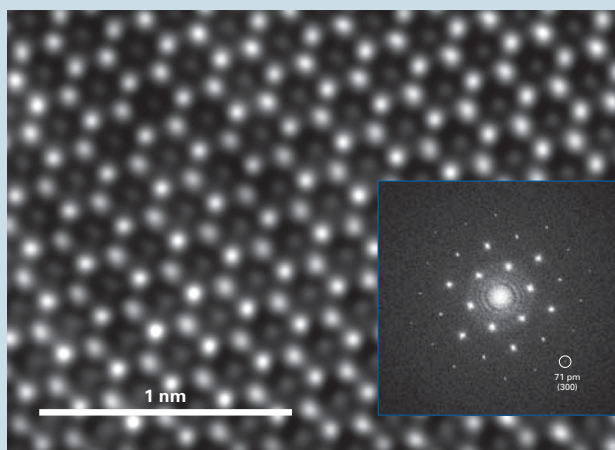


High Resolution Imaging and Spectroscopy Using Cs-Corrected TEM with Cold FEG JEM-ARM200F

Page 2

- Strain Measurement by Dark Field Electron Holography with Dual Lens Operation Page 9
- Adapting a JEM-2100F for Magnetic Imaging by Lorentz TEM Page 17
- A New WDS Spectrometer for Valence Electron Spectroscopy Based on Electron Microscopy Page 23
- Electron Microscopic Study and X-ray Probe Microanalysis of the Liver of LEC Rat, an Animal Model of Wilson Disease Page 29
- Electron Microprobe Study of Otolith: Migratory Behavior and Habitat of Three Major Temperate Species of Eels Page 33
- Realization of an Innovative Metrological Traceability Using the Quantitative NMR Method Page 51

- High Resolution Imaging and Spectroscopy Using Cs-corrected TEM with Cold FEG JEM-ARM200F 2
- Strain Measurement by Dark Field Electron Holography with Dual Lens Operation 9
- Adapting a JEM-2100F for Magnetic Imaging by Lorentz TEM 17
- A New WDS Spectrometer for Valence Electron Spectroscopy Based on Electron Microscopy 23
- Electron Microscopic Study and X-ray Probe Microanalysis of the Liver of LEC Rat, an Animal Model of Wilson Disease 29
- Electron Microprobe Study of Otolith: Migratory Behavior and Habitat of Three Major Temperate Species of Eels 33
- Realization of an Innovative Metrological Traceability Using the Quantitative NMR Method 51
- Introduction of New Products 61



Cover micrograph

A high resolution image of carbon graphite oriented along the [0001] zone axis obtained at 80 kV, with a Cs value of 230 nm.

An inset diffractogram shows that the spatial frequency (lattice resolution) of 71 pm was recorded. (See page 6)

High Resolution Imaging and Spectroscopy Using Cs-corrected TEM with Cold FEG JEM-ARM200F

C. Ricolleau[†], J. Nelayah[†], T. Oikawa^{†,††}, Y. Kohno^{††}, N. Braidy^{†,†††}, G. Wang[†], F. Hue[†] and D. Alloyeau[†]

[†] Laboratoire Matériaux et Phénomènes Quantiques, Université Paris Diderot/CNRS

^{††} JEOL Ltd.

^{†††} Laboratoire d'Etude des Microstructures, ONERA-CNRS

Recently, at the University Paris Diderot (France), a unique in the world electron microscope configuration was installed. It consists of a JEOL JEM-ARM200F spherical aberration corrected electron microscope (TEM) equipped with a cold field emission gun (CFEG). In this paper, we report on the performances of this newly developed 80 - 200 kV microscope. Firstly, we show that the stability of both emission and probe currents makes the use of this new cold-FEG much friendlier. Energy spread of electrons emitted from the CFEG has been measured as a function of emission current and shows a very last 0.26 eV energy resolution at 200 kV and even 0.23 eV at 80 kV. The combination of the cold FEG and the CEOS aberration corrector of the objective lens, associated to enhanced mechanical and electrical stabilities of this new TEM, allows reaching a point resolution of 75 pm at 200 kV and 80 pm at 80 kV. This unseen point resolution at 200 kV has allowed us to study the structure of CoPt nanoparticles by observing direct images of their atomic arrangement along high indexes zone axis, as well as carbon graphite along the [0001] zone axis orientation. The high sensitivity of this microscope allows us to image and to analyze the chemical specie of single atoms diffusing on an amorphous carbon substrate. Finally, we used the small energy spread of the CFEG to study the surface plasmon resonance modes characteristic of bimetallic nanoparticles in close electromagnetic interaction.

Introduction

The understanding of physical and chemical properties of nanomaterials requires to investigate their structural and chemical arrangements at the atomic scale. For that purpose, Transmission Electron Microscope (TEM) is the most complete characterization instrument because it gives access to all these structural aspects on individual nano-objects [1-3]. In the past, conventional high resolution TEM has given numerous information on the structural properties of nanomaterials, however, the resolution was limited to 0.18 nm at 200 kV for the best optical configuration (namely magnetic lens with a low gap pole piece). Thanks to the revolutionary development of aberration corrected TEM, the attainable spatial resolution can now be of the picometer order [4-8]. This ability to resolve distances of less than 0.1 nm is very important in order to characterize new metallic, semi-conductor, oxides, ... nanostructures for which 0.1 nm is of the same order of magnitude than the distances between atoms in many zone axis orientation of interest in these materials. Huge progresses in quantitative TEM have also been done due to the recent development of highly coherent electron sources [9-11]. Among the electron sources with a narrow energy spread around a tenth of an eV [12-14], the high brightness of Cold Field Emission Gun (CFEG) is a tremendous advantage for the study of

nanomaterials, in which poor elastic and inelastic signals emitted by small volumes of matter are key limiting factors. So far, highly coherent electron waves emitted from CFEG technology was applied to electron holography observation [15] and to the analysis of EELS fine structures [16].

The present work describes the performances of an unseen 80 - 200 kV microscope, employing a CFEG and an aberration-corrected objective lens. The capabilities of this instrument were used to determine the structure of bimetallic nanoparticles (NPs) from high index zone axis orientation, to visualize fragile carbon graphite structure, to image and to identify individual metal atoms on a surface of amorphous carbon and to measure the plasmon resonance modes in two interacting bimetallic CuAu nanoparticles.

Performances of the cold field emission gun (CFEG)

The CFEG developed in this work, employs a tungsten single crystal emitter with a <310> oriented axis. In order to keep high vacuum level in vicinity of the emitter, three non-evaporative getter (NEG) pumps are installed in the gun chamber [17]. Total evacuation speed of the NEG's corresponds to 300 (= 3×100) L/s. The accelerating tube is evacuated by 200 L/s sputter ion pump (SIP). Additionally, two intermediate chambers are designed using small orifices, in order to create a differential pumping system between gun chamber and column. These

UMR 7162, Case 7021, 75205 Paris Cedex 13, France

E-mail: Christian.Ricolleau@univ-paris-diderot.fr

intermediate chambers are also evacuated by 20 L/s and 30 L/s SIPs, respectively [17]. The newly designed evacuation system can provide a vacuum better than 5×10^{-9} Pa, at the bottom of the accelerating tube. Owing to high quality of the vacuum, high stabilities of both emission and probe currents are expected. **Figure 1** shows variations of emission and probe currents after flashing procedure of the tip. Decay rate of probe current was less than 5% in the first 2 hours after flashing. Since the probe current takes only into account electrons emitted by the (310) facets on the tungsten tip, the probe current is more stable than total emission current [18].

Figure 2a shows zero-loss peak measurements at various emission current conditions, obtained with a Quantum ER Gatan Imaging Filter[®]. The energy spread of the electron source is commonly defined by the full width at half maximum (FWHM) of the zero-loss peak, measured without specimen. The energy spread depends on the emission current due to the statistical Coulomb effect [19-20]. The energy spread varies from 0.26 eV with an emission current of 0.1 μA to 0.4 eV in normal emission current conditions (20 μA). As illustrated in Figure 2b, the energy resolution measurements are even better with an accelerating voltage of 80 kV, since the energy spread ranges

from 0.35 eV in normal emission current conditions to 0.23 eV with an emission current of 0.1 μA . The smallest energy spread obtained here is close to the theoretical value at the emitter surface (0.22 eV). This result shows that the high-voltage stability (5×10^{-7} min^{-1} peak-to-peak fluctuation) is high enough to maintain the energy spread of the CFEG.

Microscope performances

The objective lens of the TEM used in this experiment has inherent optical performances as listed in **Table 1**. In this newly developed TEM, a CEOS hexapole type spherical aberration corrector [4] was employed. Therefore, the final spherical aberration coefficient (C_s) can be tuned from -0.1 mm to $+0.5$ mm with a precision of about $1 \mu\text{m}$. The lens excitation current of objective lens has a stability of 5×10^{-7} min^{-1} in peak-to-peak fluctuation. To evaluate the aberrations of the image-forming system, a diffractogram tableau [21] with a maximum tilt angle of 24 mrad was employed. **Table 2** shows a list of residual aberrations calculated in the procedure.

Figure 3a demonstrates the achieved point resolution of the microscope in these imaging conditions. A high resolution image of a carbon film was doubly exposed with small shift of field of view induced by projector alignment deflector. The

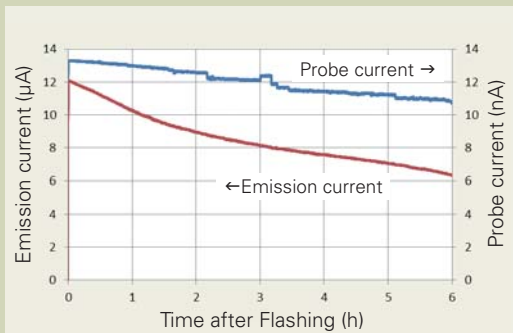


Fig. 1 Variations of emission (μA) and probe (nA) currents after flashing procedure. Decay rate of probe current was less than 5% in the first 2 hours after the flashing.

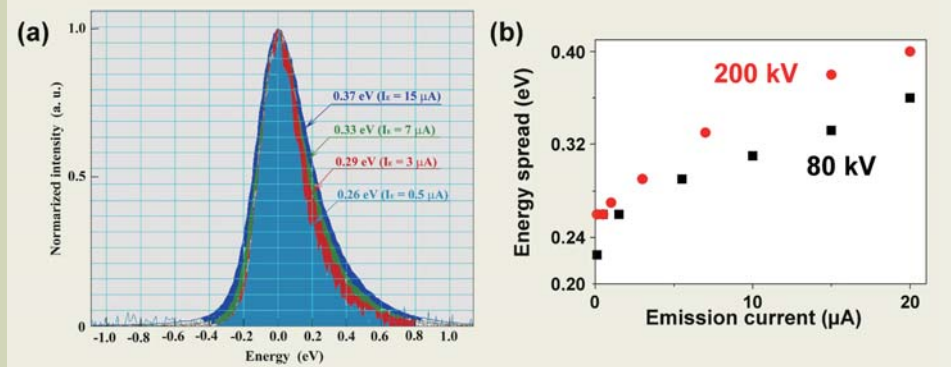
Table 1 Inherent optical performances of objective lens employed in the TEM.

Item	Performance
Focal length (f_0)	1.9 mm
Spherical aberration coefficient (C_s)	0.5 mm
Chromatic aberration coefficient (C_c)	1.1 mm
Minimum focus step (Δf)	0.25 nm
Lens current fluctuation (peak-to-peak) (ΔI)	5×10^{-7} min^{-1}

Table 2 Residual aberrations calculated by the CEOS aberration corrector software.

Residual aberration	Value
Defocus (C_1)	- 184.7 nm
Two-fold astigmatism (A_1)	140.6 pm
Three-fold astigmatism (A_2)	23.0 nm
Axial coma (B_2)	7.1 nm
Spherical aberration coefficient (C_3)	- 518.3 nm
Four-fold astigmatism (A_3)	146.1 nm
Star aberration (S_3)	167.1 nm
Five-fold astigmatism (A_4)	40.1 μm

Fig. 2 (a) Measured zero-loss peaks at various emission current (I_E) conditions. The energy spread was defined by FWHM of the zero-loss peak. (b) Energy spread as a function of emission current measured at 200 kV (red circles) and at 80 kV (black squares).



Fourier transform of this image gives the well known Young's fringes pattern which shows a point resolution of 75 pm. This resolution was measured with the commonly used minimum contrast level of 13.5%. Such a performance is close to the theoretical limit for a 200 kV TEM. Figure 3b shows the Fourier transform of a lattice image of a gold single crystal in [100] zone axis orientation. This image highlights that the microscope attains a lattice resolution of 46 pm, since the (048) reflection of the gold lattice is clearly observed. Figure 3c shows the Young's fringes pattern obtained with similar optical parameters at 80 kV. In spite of this low voltage condition, the point resolution of the microscope reaches 80 pm. The possibility to maintain sub-angstrom imaging resolution with an energy resolution below 0.4 eV at 80 kV opens many possibilities for the atomic scale characterization of beam sensitive materials.

Application data

Structural analysis of CoPt nanoparticles with the sub-angstrom resolution

Figure 4 shows calculated envelope functions of the contrast transfer function (CTF) for the cold and Schottky FEG by using the following parameters, namely $C_c = 1.1$ mm and $\Delta I/I = \Delta V/V = 5 \times 10^{-7}$. For the calculation, the energy spreads of 0.4 eV and 0.75 eV for cold and Schottky FEG were used, respectively, the accelerating voltage was 200 kV, the beam convergence angle was 2 mrad and the C_s value was close to zero. According to the calculated results, although the point resolution is limited to 0.1 nm for Schottky FEG it is

expected to obtain a point resolution of 0.075 nm for CFEG. The resolution of 75 pm obtained in the experiment (Figure 3a) is in good agreement with the calculated one. Hence, by combining the C_s corrector, the CFEG and by using newly designed microscope column and power supplies, the C_s value, the beam coherency and the microscope stability have been optimized to reach sub-angstrom resolution and improve signal to noise ratio in the high spatial frequency range. Indeed, by minimizing the damping of the envelope functions, the reduction of both electron energy dispersion and mechanical vibration allow a sub-angstrom information transfer limit (Figure 4). Thus high resolution imaging is not limited anymore for the structural study of low index crystal orientations: today one can resolve many more inter-planar distances and thus displays the structure of materials in many more orientations. This highly improved resolution is very important to study the size effect on the structural properties of individual nano-objects. This major advantage is illustrated in Figure 5a in which the structure of a CoPt nanoparticles in the [114] zone axis orientation is directly observed on the C_s corrected high resolution image and an information transfer up to the -440 reflection (65 pm) is reported on the Fourier transform (Figure 5b).

Graphite

In the previous section, we have seen that the performances of the JEOL JEM-ARM200F cold FEG are almost the same at 80 kV than the ones at 200 kV. It is thus possible to observe nanomaterials which are sensitive to electron beam such as polymers and carbon

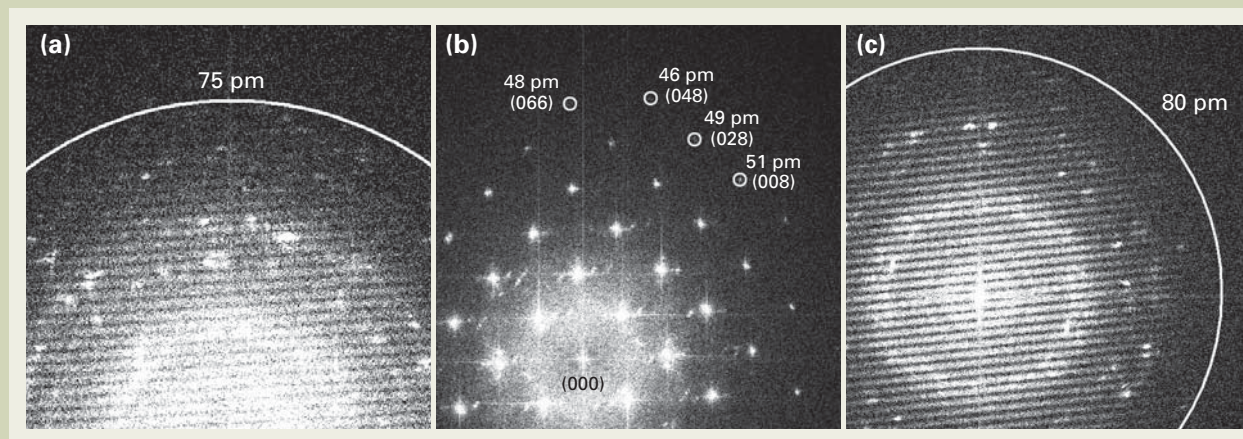
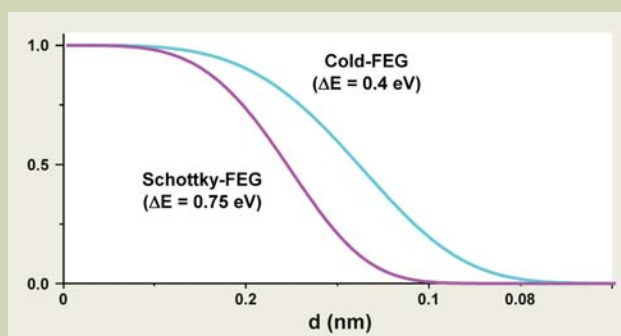


Fig. 3 (a) Young fringes pattern obtained at 200 kV showing a point resolution of 75 pm. (b) Fast Fourier transformation (FFT) of a high resolution image obtained at 200 kV on a (100) gold single crystal. The observation of the [048] peak of the gold crystal highlights that the lattice resolution of the microscope is below 50 pm ($d_{048} = 0.046$ nm). (c) Young fringes pattern obtained at 80 kV showing a point resolution of 80 pm.

Fig. 4 Calculated envelope functions of the contrast transfer function (CTF) for cold (cyan) and Schottky (magenta) FEG by using the following parameters, namely $C_c = 1.1$ mm and $\Delta I/I = \Delta V/V = 5 \times 10^{-7}$. For the calculation, the energy spreads of 0.4 eV and 0.75 eV for the cold and Schottky FEG were used, respectively, the accelerating voltage was 200 kV, the beam convergence angle was 2 mrad and the C_s value was close to zero.



nanostructures. This instrument opens up the route to direct observations of the grafting of molecules on the surface on the nanotubes as well as to the determination of the electronic states of these hybrid nanostructures in order to study their structural and electronic properties.

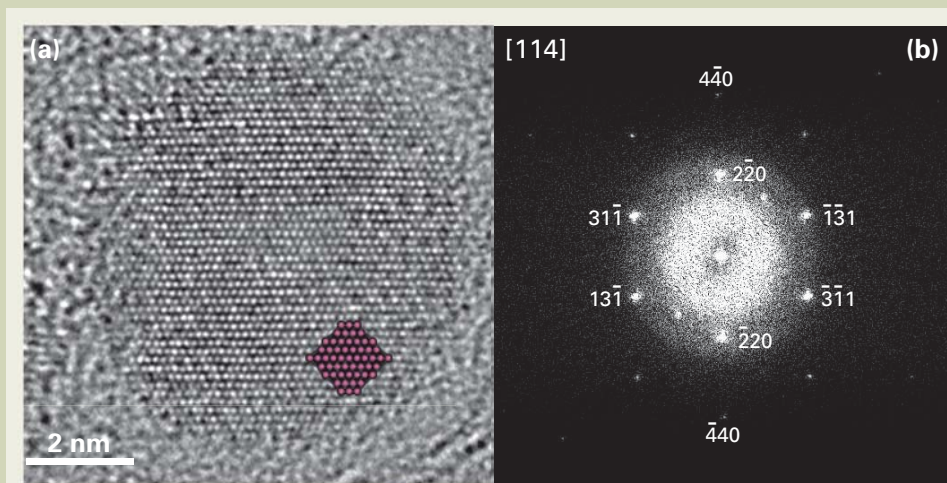
As an example of fragile materials imaging, **Figure 6** shows high resolution images of carbon graphite oriented along the [0001] zone axis obtained at 80 kV, with a C_S value of 230 nm. Figure 6a shows a wide field of view of the sample where more or less dark contrasts are visible in the image. Those contrasts correspond to different layer steps of the graphite. The specimen is composed by the stacking of only a few layers of graphite. Figure 6b shows a diffractogram of the image (a), the spatial frequency (lattice resolution) of 71 pm was recorded. Figure 6c shows a magnified area from a part of the image in (a) marked by the white rectangle. Noise reduction was applied to the image by using a spatial annular filter in the power spectrum of the original image. Figure 6d shows the atomic model of the mono-layered graphite. By comparison with the experimental image, we clearly observed that the white contrast corresponds to carbon atom sites.

Single atom imaging

When the growth and coarsening of nanostructures composed of two or more chemical elements are concerned, the imaging and chemical identification of single atoms is of primary importance to understand coalescence and Ostwald ripening phenomena at the atomic scale. Furthermore, in the case of alloyed nanostructures, nanoparticle compositional changes may arise during growth or thermal annealing if the two species have different thermodynamic behavior. As an example, we have shown in a previous paper on CoPt bimetallic nanoparticles [22], that after a heat treatment at high temperature, the larger NPs present a large excess of Co. To understand the origin of this result, we have studied *in situ* the NPs coarsening by using the energy transferred from the electron beam to the nanoparticles. Typical HRTEM image of the CoPt NPs after a few seconds under beam irradiation is presented in **Figure 7a**. On this image, individual atoms appear as additional contrast in the carbon film between the NPs. However, these contrasts appear and disappear from frame to frame when image series

are recorded with a 0.2 s time interval indicating that the diffusion of metallic atoms on carbon substrate is too fast to follow the path of a single atom from a particle to another. But, it is still possible to observe such diffusing atoms on HRTEM images because they are trapped long enough in energetically favorable site of the carbon thin film. In order to interpret this result and to determine the chemical nature of the atoms, comparison between experimental and simulated HRTEM images was performed. For that purpose, the atomic model consists in one Co and one Pt atom on a 5 nm-thick amorphous carbon film. To quantify the simulated and experimental contrast of single atoms in the images, we used the signal to noise ratio (SNR) definition proposed by Rose [23]. The SNR is defined as the ratio between the incremental change in the image intensity due to the atoms and the standard deviation of the carbon film intensity (defined as the noise level). We calculated the SNR as a function of the objective lens defocus for both Co and Pt atoms and we have shown that the SNR is flat against the defocus in a range from -2 to -10 nm and that the contrast difference between Co and Pt is significant: from -2 to -2.6 for Co and from -3 to -3.6 for Pt. These simulations allow us to determine the optimum optical condition for the chemical analysis of single atoms. The analysis of the single atom contrast was firstly performed on pure Co and Pt NPs to calibrate the experimental conditions. The histograms of the SNR of single atoms for both samples are shown on **Figure 8**. These histograms are centered on -2.68 for Co atoms and -3.18 for Pt atoms, with a standard deviation of 0.18 and 0.30 respectively. These values are in good agreement with simulations. On CoPt nanoparticles, as shown in Figure 7a, both Co and Pt atoms were detected during the beam induced NPs coarsening. The first profile (green intensity profile in Figure 7b) reveals the presence of a Co atom on the carbon film (SNR of -2.32) whereas the second profile (blue intensity profile on Figure 7c) shows a Pt atom (SNR of -3.59). These results show that, using these illumination conditions, the energy transferred from the electron beam to the CoPt NPs allows overcoming the energy barrier for atomic evaporation from a NP to the substrate either for Co or Pt atoms. Furthermore, a statistical analysis realized by measuring the SNR of 100 single atoms clearly shows that the kinetic of atomic exchange is faster for Co than Pt. Indeed, among the 100 analyzed atoms, 61 are Co, 32 are

Fig. 5 (a) HRTEM image of a CoPt nanoparticle observed along the [114] zone-axis orientation ($C_S=0.005$ mm, $\Delta f=-0.5$ nm (Scherzer focus), focus spread of 2.2 nm). An inset (red) indicates an atomic model on the projected plane. (b) Corresponding power spectrum of the HRTEM image (a).



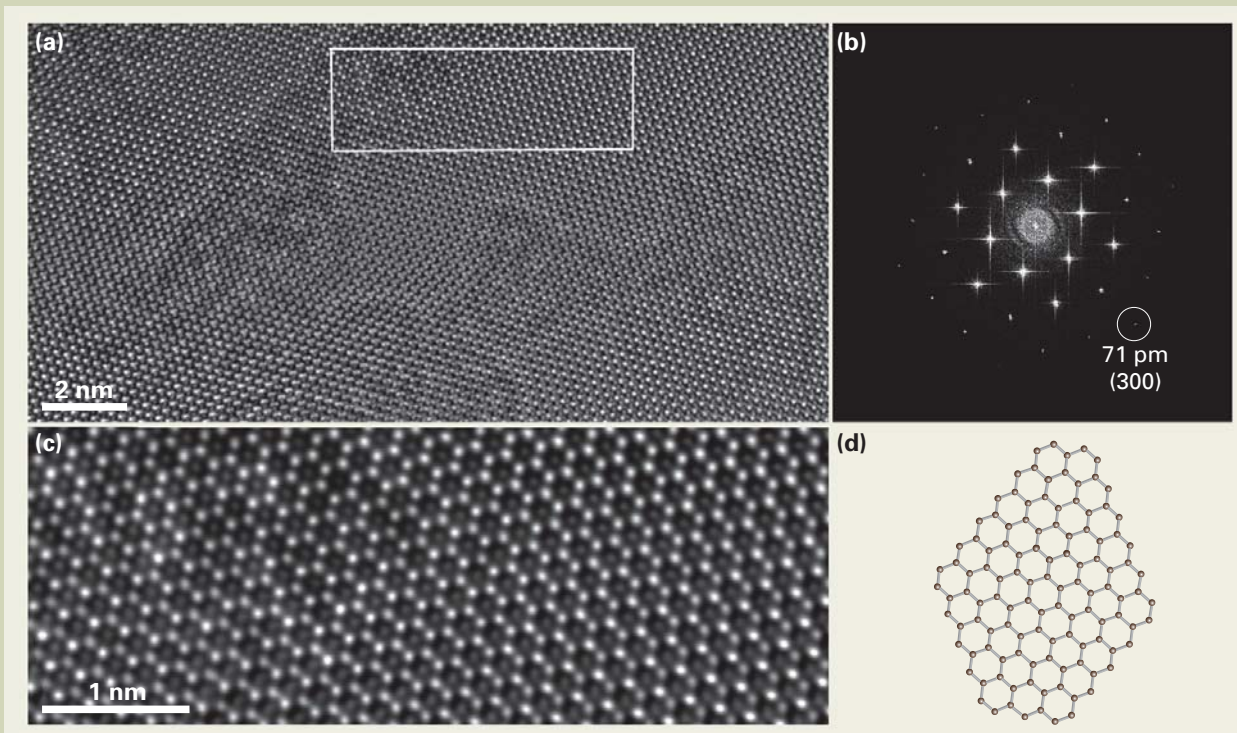


Fig. 6 (a) HRTEM image of a carbon graphite crystal oriented along the [0001] zone axis obtained at 80 kV. (b) Fourier transform of the image (a). (c) Magnified area corresponding to the white rectangle in image (a). The image was obtained by applying a spatial filter to the original image (a). (d) Atomic model of a mono-layered graphite crystal.

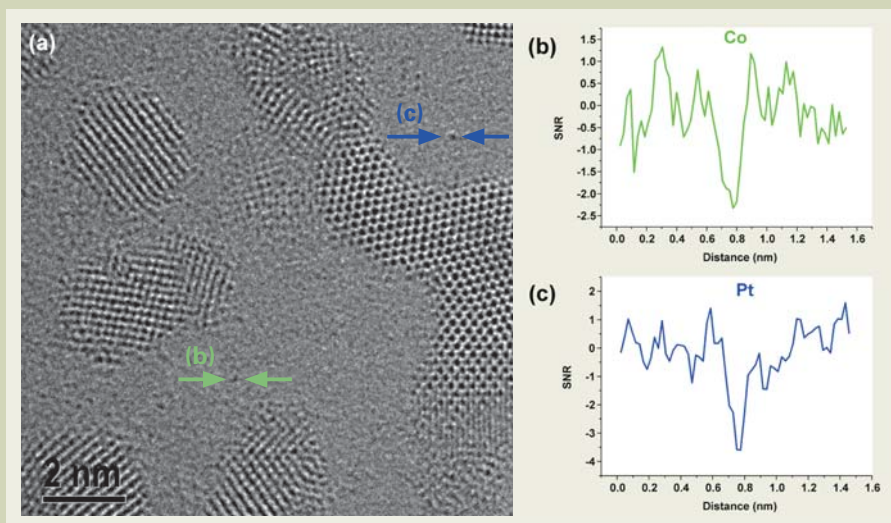


Fig. 7 (a) HRTEM image of CoPt nanoparticles. Individual Co and Pt atoms appear as additional black contrast on the carbon substrate. Signal to noise ratio (SNR) measured between the two corresponding arrows in (a) for both Co and Pt atoms: (b) SNR profile showing one Co atom (SNR of -2.32). (c) SNR profile showing one Pt atom (SNR of -3.59).

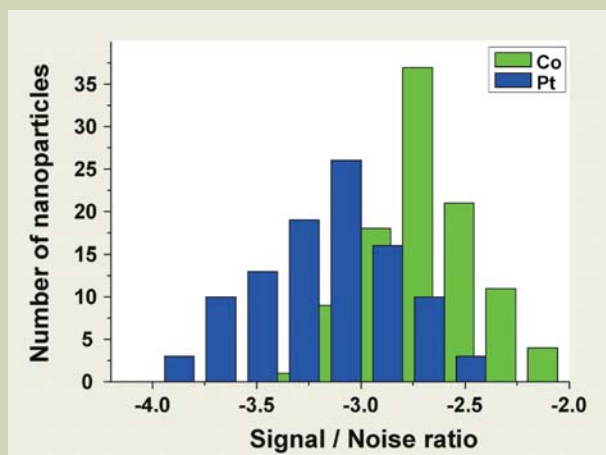


Fig. 8 Histogram of the single atom SNR experimentally measured for pure Co NPs (green) and pure Pt NPs (blue).

Pt and 7 are undetermined. These results explain the size dependant composition changes in CoPt NPs and highlight the better mobility of Co atoms with respect to Pt atoms because of their higher evaporation rate. These results show that the sensitivity of the microscope enhanced by the high brightness of the cold FEG and the mechanical stability of the ARM200F, allows distinguishing the chemical nature of individual Co and Pt atoms while they are diffusing on the surface of the carbon substrate. In this study, the modulation transfer function (MTF) of the Gatan CCD camera was not taken into account because we always use the same magnification in order to have the same MTF effects in all the HRTEM images. It is however possible to improve the quantitative agreement between experimental and simulated single atom contrast by accounting this MTF on the experimental images [24].

Plasmon resonance nanospectroscopy in metallic nanoparticles

Metallic nanoparticles have shown to exhibit unique optical properties. The latter result from the existence of collective electronic excitations, known as surface plasmon resonances (SPRs), under electromagnetic excitations (for instance, light or fast electrons) [25]. Associated with these surface-bound resonances are intense electromagnetic fields which are exploited in various potential applications like surface-enhanced Raman scattering and all-optical communication. In the context of an electron microscope, nanometer-scale studies of SPRs in the visible spectral domain, where most of the potential applications lie, is now possible using electron energy loss spectroscopy [26-27]. Taking full advantage of the intense and highly monochromatic sources of electrons that is generated by the cold FEG JEOL JEM-ARM200F, our group has been using spatially-resolved STEM-EELS to investigate the optical response of either isolated or interacting metallic nanoparticles. **Figure 9a** shows an HAADF image of two carbon-supported gold-copper nanocubes in very close interaction (gap distance <1 nm). EEL spectra were acquired at different positions on the dimer with the following experimental conditions: the microscope was operated at 200 kV and with an initial energy resolution of about 0.4 eV (2.5 mm spectrometer entrance aperture, camera length 3 cm and 0.05 eV/pix dispersion). To increase the signal-to-background ratio in the visible domain, the raw data was subsequently

deconvoluted using a non-linear iterative algorithm [28]. The spatial resolution, fixed by the probe size, was better than 1 nm (spot size 5C). Figure 9b compares STEM-EEL spectra acquired at five distinct positions on the dimer. The position, at which each numbered spectrum is acquired, is indicated by red dots in Figure 9a. Two distinct modes centered at about 2.30 eV and 2.60 eV are detected at the outer corners and in the gap region respectively. Comparison of the EELS data shows these SPRs are common to the two nanocubes (the dimer) though they are not identical. This results from the electromagnetic coupling between the nanocubes when they are brought in interaction. Such analysis illustrates the power of STEM-EELS to finely study the optical properties of nanoparticles with the aim of tailoring these properties for targeted applications.

Conclusion

The JEOL JEM-ARM200F cold FEG TEM described in this paper is the first commercial instrument combining both a cold field emission electron source and a CEOS aberration corrector of the objective lens. We have shown the very good stability of both emission and probe currents thanks to a new design of the vacuum system for the gun chamber including non evaporating getter pumps. The combination of the JEOL cold FEG and the CEOS aberration corrector, associated to enhanced mechanical and electrical stabilities of the instrument allows reaching a point resolution of 75 pm at 200 kV and 80 pm at 80 kV. Owing to high coherency of electron waves and high stabilities of both electrical and mechanical part on the TEM developed in this work, much smaller lattice spacing information that the point resolution were excited in the interferences of the waves. In addition, the high brightness of the cold FEG substantially improved imaging sensitivity that is essential for quantitative high resolution imaging.

We have shown that sub-angstrom imaging is of great benefit for understanding the structural properties of nanomaterials, because it is now possible to observe crystals and defects along high index zone axis orientation. We have also demonstrated that the performances of the microscope can be exploited for studying the mobility of single atoms on surface which is very useful for the understanding of crystal growth and crystal reshaping, as well as the understanding of the coalescence and Ostwald ripening phenomena at the atomic scale. Finally, we

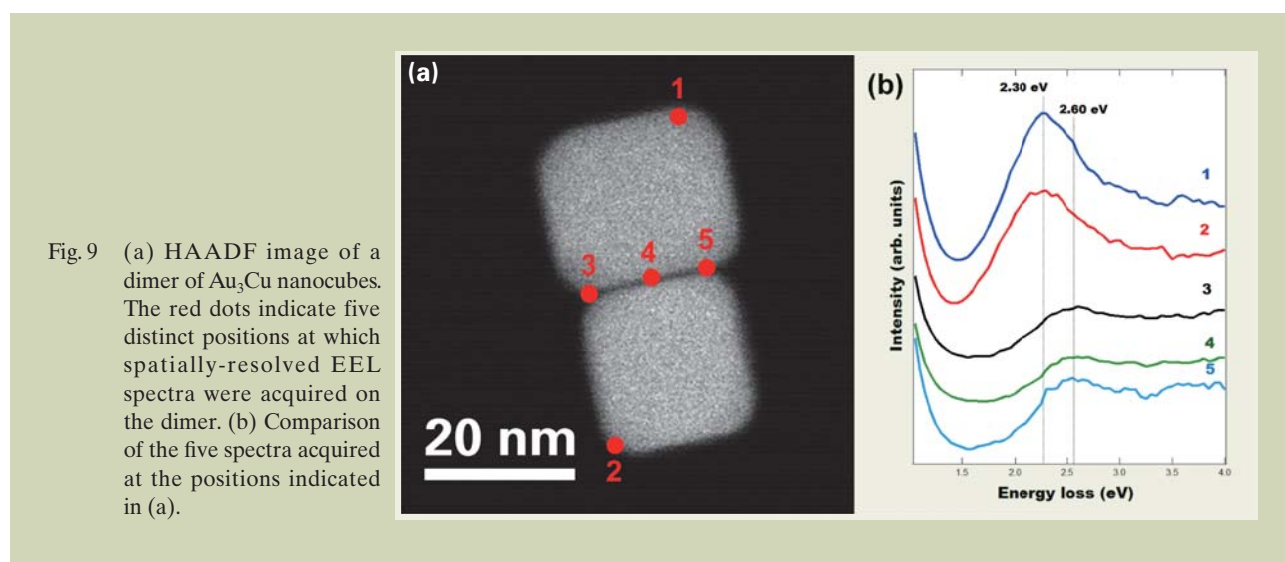


Fig. 9 (a) HAADF image of a dimer of Au₃Cu nanocubes. The red dots indicate five distinct positions at which spatially-resolved EEL spectra were acquired on the dimer. (b) Comparison of the five spectra acquired at the positions indicated in (a).

showed how the small energy spread of the cold FEG can be successfully used to measure surface plasmon resonance modes characteristic of metallic nanoparticles which are close enough to exhibit electromagnetic interactions.

Acknowledgments

Financial support from ANR within ANR-07-NANO-018-04 (ETNAA) is gratefully acknowledged. The authors are indebted to Dr Dario Taverna (IMPMC, University Paris 6, Paris, France) for providing us the graphene / graphite sample.

References

- [1] Kirkland A.I. Nanocharacterisation. Royal Society of Chemistry, Cambridge. (2007).
- [2] Reimer L. Transmission Electron Microscopy. Springer, Berlin. (1997).
- [3] Shindo D. and Hiraga K. High-Resolution Electron Microscopy for Materials Science. Springer Verlag, Tokyo. (1998).
- [4] Haider M., Uhlemann S., Schwan E., Rose H., Kabius B. and Urban K. Electron microscopy image enhanced. *Nature* **392**: 768-769 (1998).
- [5] Krivanek O.L., Dellby N. and Lupini A.R. Towards sub-Angstrom electron beams. *Ultramicroscopy* **78**: 1-11 (1999).
- [6] Urban K. Studying Atomic Structures by Aberration Corrected Transmission Electron Microscopy. *Science* **321**: 506-510 (2008).
- [7] Kisielowski C., Freitag B., Bischoff M., Van Lin H., Lazar S., Knippels G., Tiemeijer P., Van Der Stam M., Von Harrach S., Stekelenburg M., Haider M., Uhlemann S., Müller H., Hartel P., Kabius B., Miller D., Petrov I., Olson E.A., Donchev T., Kenik E.A., Lupini A.R., Bentley J., Pennycook S.J., Anderson I.M., Minor A.M., Schmid A.K., Duden T., Radmilovic V., Ramasse Q.M., Watanabe M., Erni R., Stach E.A., Denes P. and Dahmen U. Detection of Single Atoms and Buried Defects in Three Dimensions by Aberration-Corrected Electron Microscope with 0.5-Å Information Limit. *Microscopy and Microanalysis* **14**: 469-477 (2008).
- [8] Takayanagi K., Kim S., Lee S., Oshima Y., Tanaka T., Tanishiro Y., Sawada H., Hosokawa F., Tomita T., Kaneyama T. and Kondo Y. Electron microscopy at a sub-50 pm resolution. In: *Journal of Electron Microscopy*, pp. S239-S244 (2011).
- [9] Browning N.D., Arslan I., Erni R., Idrobo J.C., Ziegler A., Bradley J., Dai Z., Stach E.A. and Bleloch A. Monochromators and aberration correctors: Taking EELS to new levels of energy and spatial resolution. In: *EMAG-NANO 2005: Imaging, Analysis and Fabrication on the Nanoscale*, eds. Brown P D, Baker R and Hamilton B, pp. 59-64, (Iop Publishing Ltd, Bristol) (2006).
- [10] Kimoto K., Ishizuka K., Asaka T., Nagai T. and Matsui Y. 0.23 eV energy resolution obtained using a cold field-emission gun and a streak imaging technique. *Micron* **36**: 465-469 (2005).
- [11] Kimoto K., Kothleitner G., Grogger W., Matsui Y. and Hofer F. Advantages of a monochromator for bandgap measurements using electron energy-loss spectroscopy. *Micron* **36**: 185-189 (2005).
- [12] Browning N.D., Arslan I., Erni R., Idrobo J.C., Ziegler A., Bradley J., Dai Z., Stach E.A. and Bleloch A. Monochromators and aberration correctors: Taking EELS to new levels of energy and spatial resolution. In: *EMAG-NANO 2005: Imaging, Analysis and Fabrication on the Nanoscale*, eds. Brown P D, Baker R and Hamilton B, pp. 59-64, (Iop Publishing Ltd, Bristol) (2006).
- [13] Kimoto K., Ishizuka K., Asaka T., Nagai T. and Matsui Y. 0.23 eV energy resolution obtained using a cold field-emission gun and a streak imaging technique. *Micron* **36**: 465-469 (2005).
- [14] Kimoto K., Kothleitner G., Grogger W., Matsui Y. and Hofer F. Advantages of a monochromator for bandgap measurements using electron energy-loss spectroscopy. *Micron* **36**: 185-189 (2005).
- [15] Tonomura A. Applications of electron holography. *Rev. Mod. Phys.* **59**: 639-669 (1987).
- [16] Chen S.Y., Gloter A., Zobelli A., Wang L., Chen C.H. and Colliex C. Electron energy loss spectroscopy and ab initio investigation of iron oxide nanomaterials grown by a hydrothermal process. *Phys. Rev. B* **79**: 104103 (2009).
- [17] Kohno Y., Okunishi E., Tomita T., Ishikawa I., Kaneyama T., Ohkura Y., Kondo Y. and Isabell T. Development of a Cold field-Emission Gun for a 200 kV Atomic Resolution Electron Microscope. *Microscopy and Analysis Nanotechnology* **24**: S9-S13 (2010).
- [18] Kasuya K., Katagiri S., Ohshima T. and Kokubo S. Stabilization of a tungsten <310> cold field emitter. *Journal of Vacuum Science & Technology B: Microelectronics and Nanometer Structures* **28**: L55-L60 (2010).
- [19] Jansen G.H. *Coulomb interaction in particle beams*. Academic Press Inc. (1990).
- [20] Tiemeijer P.C. Measurement of Coulomb interactions in an electron beam monochromator. *Ultramicroscopy* **78**: 53-62 (1999).
- [21] Zemlin F., Weiss K., Schiske P., Kunath W. and Herrmann K.H. Coma-free alignment of high resolution electron microscopes with the aid of optical diffractograms. *Ultramicroscopy* **3**: 49-60 (1978).
- [22] Alloyeau D., Prévot G., Le Bouar Y., Oikawa T., Langlois C., Loiseau A. and Ricolleau C. Ostwald ripening in nanoalloys : when thermodynamics drives a size-dependent particle composition. *Phys. Rev. Letters*, **105**, 255901 (2010).
- [23] Rose A., *Advances electronics and electron physics*. Academic Press, New York, (1948).
- [24] A. Thust, High-Resolution Transmission Electron Microscopy on an Absolute Contrast Scale. *Physical Review Letters* **102**, 220801 (2009).
- [25] Kreibitz U. and Vollmer M. *Optical Properties of Metal Clusters*, volume 25 of Springer Series in Material Science. Springer, Germany, (1995).
- [26] Bosman M., Keast V. J., Watanabe M., Maarouf A. I. and Cortie M.B. Mapping Surface Plasmons at the Nanometre Scale with an Electron Beam. *Nanotechnology* **18**, 165505 (2007).
- [27] Nelayah J., Kociak M., Stephan O., J.Garcia de Abajo F., Tence M., Henrard L., Taverna D., Pastoriza-Santos I., Liz-Marzan L.M., and Colliex C. Mapping surface plasmons on a single metallic nanoparticle. *Nature Physics* **3** (5) :348-353 (2007).
- [28] Gloter A., Douiri A., Tencé M. and Colliex C. Improving energy resolution of EELS spectra: an alternative to the monochromator solution. *Ultramicroscopy* **96**: 385-400 (2003).

Strain Measurement by Dark Field Electron Holography with Dual Lens Operation

Y.Y. Wang[†], J. Li[†], A. Domenicucci[†], J. Bruley[†],
M. Kawaski^{††}, D. Cooper^{†††}, and J. Rouvière^{†††}

[†] IBM microelectronics division

^{††} JEOL USA

^{†††} CEA LETI Minatoc

^{††††} CEA DSM INAC

Dark field electron holography with dual lens operation to achieve high spatial resolution is summarized. Its application to measure strain on semiconductor devices is reported and comparison with converging beam electron diffraction (CBED) and nano-beam electron diffraction (NBD) is discussed.

Introduction

Recent development of CMOS Si semiconductor device shows that strain along the channel region greatly enhances the device performance, which has assisted further scaling of semiconductor devices. For PFET device, the compressive stress is beneficial to the device performance, while for NFET device, the tensile stress is. Because of that, the strain measurement at nano-meter scale becomes critical for device engineering for next generation integrated circuit (IC) development and manufacturing.

It has been shown that converging beam and nano-beam diffraction can be used to measure strain of Si. In 2008, Mytch et al. reported that dark field holography provided a promising path to nano-meter scale strain mapping [1]. Initial strain map acquired by Mytch et al. was done on an instrument with a Lorentz lens (single lens electron holography), which has fringe spacing of 2.0 nm. The principle of dark field holography is to use a biprism to overlap a strained region of the device with an unstrained region in Si. By selecting a specific diffracted beam with an objective aperture to obtain a dark field hologram, the difference of lattice constant between strained and unstrained Si can be measured and the change of the lattice constant can be mapped out through a data processing [1-4].

In this paper, we report that, using a dual lens system on JEOL JEM-2010F [5-8], we achieve a fringe spacing relative to the sample down to 1.0 nm, thus, provide a more detailed map of strain distribution of 3 nm spatial resolution (3x fringe spacing). We also compare strain measurement by dark field electron holography with the ones obtained by converging beam electron diffraction (CBED) and nano-beam electron diffraction (NBD).

Background theory of electron holography

There are three critical parameters in electron holography: fringe spacing for spatial resolution, interference width for field of view, and fringe contrast for signal to noise ratio. As shown in **Fig.1a**, an off-axis electron hologram can be thought of as being formed from two virtual sources, S_1 and S_2 , of finite size (δ) positioned above the biprism and separated by a distance d . The fringe spacing, σ_o , and interference width (field of view), W_o , relative to the sample (object) can be described as [9, 10]:

$$\sigma_o = \frac{\lambda}{2\gamma_o V_b} \left(1 + \frac{b}{a}\right) \frac{1}{M_o} \dots\dots\dots(1)$$

and

$$W_o = [2\gamma_o V_b b - 2r_b \left(1 + \frac{b}{a}\right)] \frac{1}{M_o} \dots\dots\dots(2)$$

2070 Route 52, Mail Stop 40E Hopewell Junction, NY 12533, USA

E-mail: Wangyy@us.ibm.com

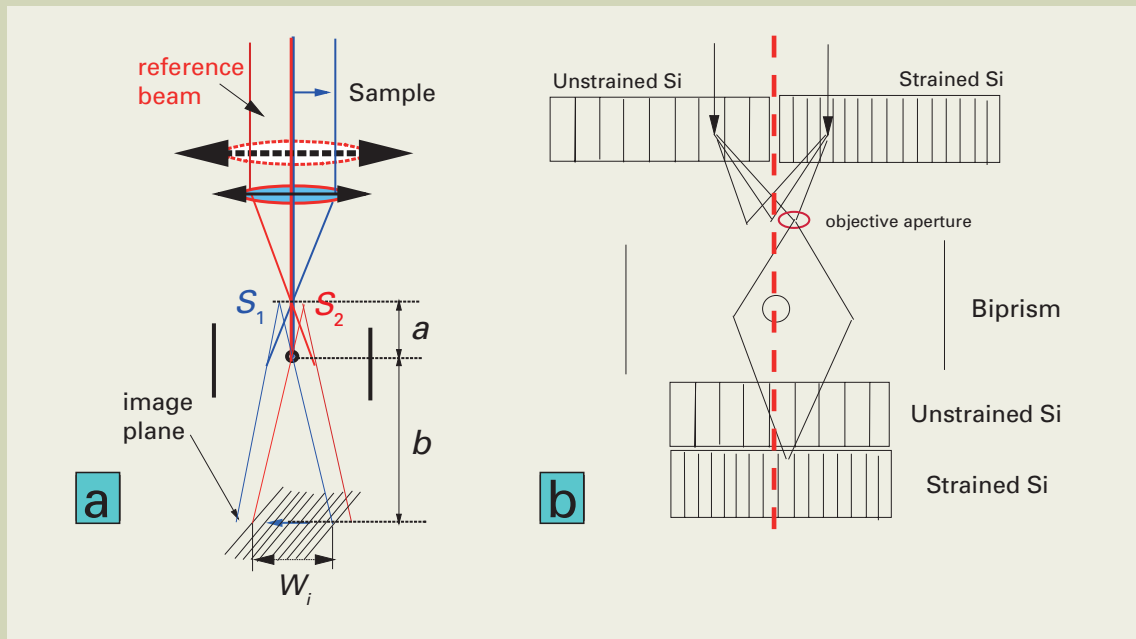


Fig. 1 (a) Bright field electron hologram formation with two virtual sources, S_1 and S_2 .
 (b) Off-axis dark field electron holography. Diffracted beam is selected by moving objective aperture to the diffracted beam location.

where γ_o is related to the accelerating voltage of electron beam and the other parameter of the microscope setting, r_b is biprism radius, a is the distance between the virtual sources and biprism position, b is the distance between image plane and the biprism, λ is the wavelength of the electron beam, and V_b is the biprism voltage, M_o is the magnification of the imaging lens(es). The fringe contrast, μ , has been derived as [5]:

$$\mu = \frac{I_{max} - I_{min}}{I_{max} + I_{min}} = \frac{\sin(\beta)}{\beta}, \quad \dots\dots\dots(3)$$

where

$$\beta = \frac{2\pi\delta}{\lambda} \frac{\gamma_o b}{a+b} V_b + \beta_0 \quad \dots\dots\dots(4)$$

In Eq.(4), the constant, β_0 , is added on to fit experimental data[11], in addition to the first term derived from the wave optics [12].

To get useful electron hologram, we need reasonable fringe contrast, which is 20%-40%, and high number of fringe in the hologram. Fringe number can be calculated as following:

$$N = \frac{W_o}{\sigma_o} \quad \dots\dots\dots(5)$$

Based on above equations, increasing the biprism voltage increases number of fringes and decreases the fringe contrast. Both fringe number and fringe contrast has a strong dependence on biprism voltage, either can be used to estimate the coherence of electron holography. We propose to use a discount fringe number, a product

of fringe contrast and fringe number, to estimate the coherence:

$$N' = N\mu \quad \dots\dots\dots(6)$$

Mathematically, with a linear approximation of Eq.(3) in the β range of 0.5π and 0.8π , one can derive that there is a maximum N' , at the fringe contrast value, μ_{max} , as [11]:

$$\mu_{max} \approx \frac{1}{3} (1.3 - 0.4 \beta_0) \quad \dots\dots\dots(7)$$

Since the N' near its maximum value changes smallest against μ or V_b , N' can be used to estimate the goodness of the coherence.

The principle of dark field holography is to use a biprism to overlap a strained region of the device with an unstrained region in Si, as shown in Fig.1b. The intensity of a dark field hologram can be written as:

$$I = A_r^2 + A_o^2 + 2\mu A_o A_r \cos [2\pi q_c r + 2\pi(\vec{g}_r - \vec{g}_o) \bullet \vec{r} + \varphi_r - \varphi_o] \quad \dots\dots\dots(8)$$

where \vec{g}_o and \vec{g}_r are g vectors from the region of the interest (object) and the reference, respectively. The phase of the hologram is:

$$\varphi = 2\pi(\vec{g}_r - \vec{g}_o) \bullet \vec{r} + \varphi_r - \varphi_o \quad \dots\dots\dots(9)$$

The lattice constant change to the first order can be calculated as,

$$\varepsilon_{ii} = \frac{d_o^{(i)} - d_r^{(i)}}{d_r^{(i)}} \approx \frac{1}{2\pi g_r^{(i)}} \frac{\partial \varphi^{(i)}}{\partial r_i} \quad \dots\dots\dots(10)$$

where $i=x, z, g=1/d$, and d is the lattice spacing. In that equation, it is assumed that the diffraction spot is in the x, z direction for the simplest case. By selecting a specific diffracted beam with an objective aperture to obtain a dark field hologram, the difference in lattice spacing between strained and unstrained Si can be measured.

In 2004 paper and patent, we described the dual lens operation to change the magnification of objective lenses (lenses between sample and biprism) [5-8]. The basic principle is to use objective lens to form a magnified virtual image and objective mini-lens to project the virtual image onto the imaging plane, which is shown in Fig.2a. To simplify the operation of projection lenses, objective mini-lens is used to focus the image to the same imaging plane.

For bright field electron holography (junction profiling), the virtual source position is not as critical. But for dark field holography, the ideal position should be near the objective aperture. For a single lens operation, the position is at the back focal plane of the lens; while for dual lens system, the position

depends on the focal point of the objective lens as well as objective mini-lens as shown in Fig.2b. A third weak lens can be added into the design of an electron microscope before the biprism, but after the second lens, to move the virtual focal point without affecting much of dual lens operation. That configuration is proposed in a patent publication as a tri-lens operation [13].

Instruments

The JEM-2010F microscope is used for the strain measurements, which include converging beam analysis, nano-beam diffraction analysis, and dark field electron holography. The instrument is equipped with $4k \times 4k$ camera (top camera) for imaging and $2k \times 2k$ camera for Gatan energy filtered imaging system. Converging beam and nano-beam diffraction was obtained using the top camera and dark field electron hologram was obtained with Gatan energy filtered camera.

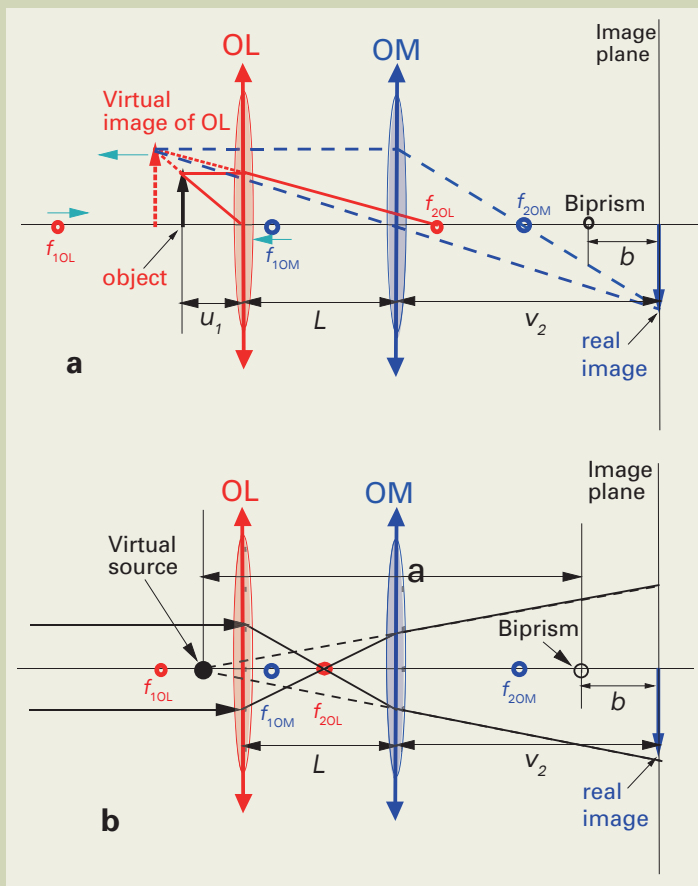


Fig.2 (a) Optical ray diagram of dual lens operation. A magnified virtual image of OL is shown as dashed image and a real image is projected by OM onto the imaging plane. (b) Virtual source position in dual lens operation. The diagram is for illustration purpose only, the actual position of virtual source may vary.

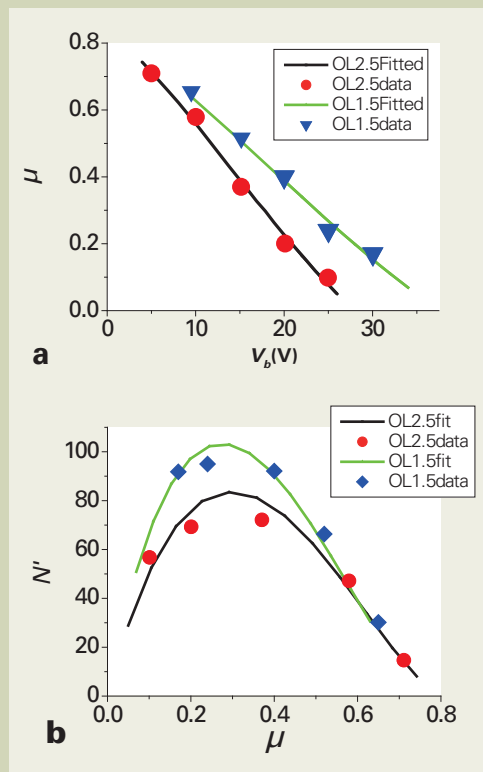


Fig.3 (a) Contrast vs. biprism voltage for JEM-2010F with different objective lens (OL) current. Data for OL=1.5 and OL=2.5 are fitted by Eqs.(3) and (4). (b) Discount fringe number vs. fringe contrast. A maximum of N' is observed near fringe contrast of ~30%.

Experimental result

Experimental data of contrast and discount fringe number

We have measured contrast vs biprism voltage on JEOL JEM-2010F with different objective lens current (OL). Using Eqs.(3) and (4), we can fit the data, shown in **Fig.3a**, and obtain β_0 of 0.99 and 1.03 for OL of 2.5 and 1.5, respectively. From the data fitting, we realized that β_0 does not depend on objective lens value that much. In Fig.3b, we plot the measured data and fitted data of discount fringe number, N' , vs. contrast for OL=1.5 and OL=2.5 obtained from 2010F instrument. In that figure, it is shown that the maximum N' is ~70-90 at the contrast value of ~30%, which is consistent with the result derived from the mathematical calculation[11]. Between 20%-40% contrast range, the N' is less dependent on contrast or biprism voltage, which leads us to believe that this can be used to estimate the coherence of electron

holography.

Strain measurement by dark field electron holography

One way to increase strain under the channel for PFET is to use embedded $\text{Si}_{(1-x)}\text{Ge}_x$ (e-SiGe) as a stressor, as shown in **Fig.4**. The Si in the source/drain (S/D) region is etched away, and e-SiGe is grown in the S/D region. Because Ge atom is larger than Si atom, it applies pressure onto the channel region, which causes a decrease in lattice constant of Si in the channel. SiGe to SiGe proximity is defined as L in **Fig.5**. The strain maps were generated based on Hytch et al.s' method¹ and the data processing is based on geometrical phase analysis developed earlier[2, 3].

Fig.5a shows a deformation map for a PFET device with an e-SiGe to e-SiGe distance of about 130 nm (L) and a Ge concentration of 17%[14]. The map is extracted from a dark field hologram obtained on a

Fig. 4 Schematics of embedded SiGe to increase compressive stress under the channel for PFET to improve the mobility of the device. L is defined as SiGe to SiGe proximity.

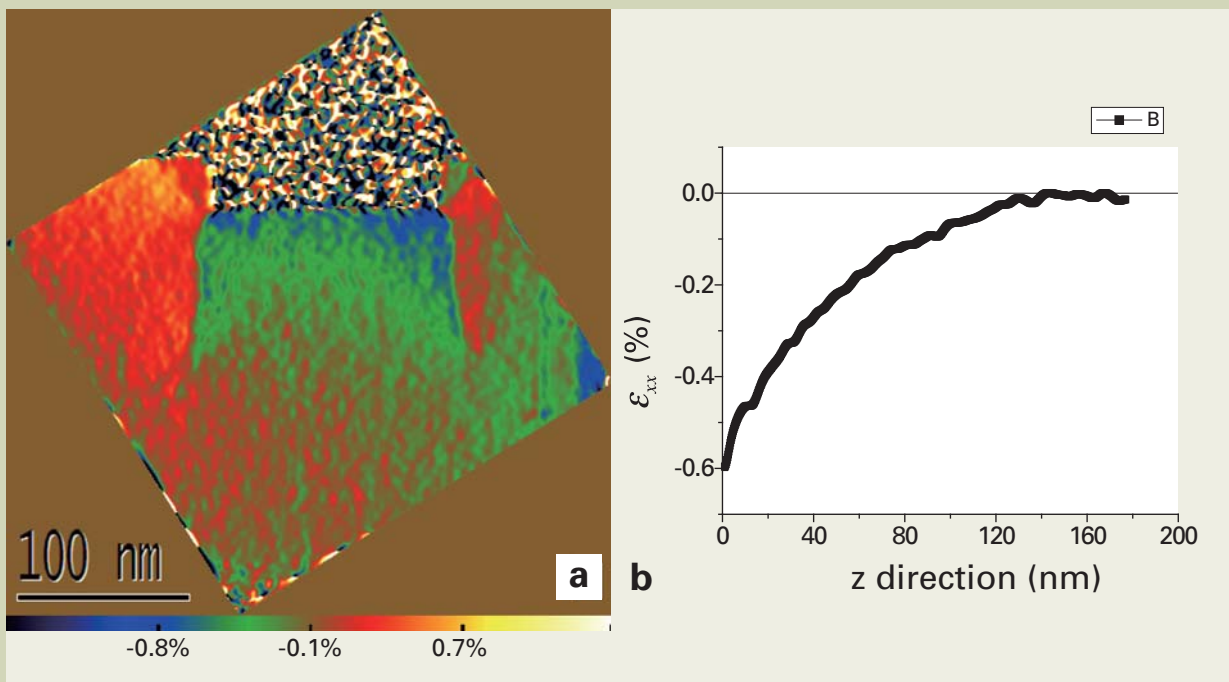
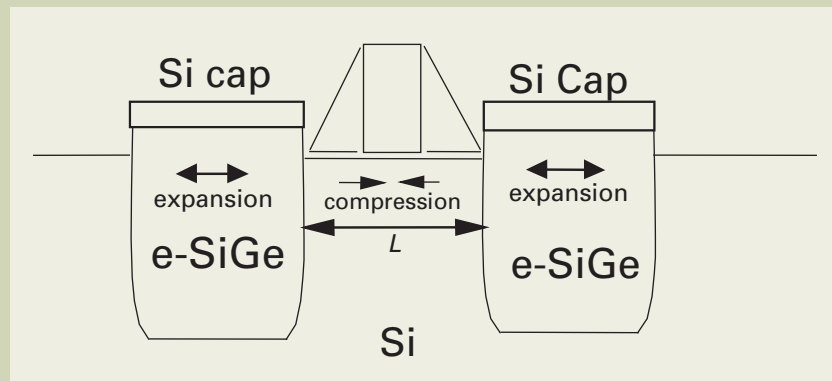


Fig. 5 (a) A strain map of $\langle 220 \rangle, \epsilon_{xx}$, from off-axis dark field hologram. SiGe proximity L is 130 nm. (b) Vertical profile of the strain map under the gate. At the Si surface, -0.6% lattice constant change along x direction is observed.

2010F instrument operated with dual lens mode. The dark field image was obtained by moving the objective aperture to $\langle 220 \rangle$ spot (Fig.1b). The objective lens was operated at $OL= 5.0$. Fig.5b shows a vertical profile of the change in d spacing along $\langle 220 \rangle$ direction. The deformation under the channel is measured at -0.6% . Fig.6a shows a deformation map for a PFET device with L of 56 nm and Fig.6b and Fig.6c is the vertical profile and horizontal profile of lattice constant change in the channel and in SiGe region, respectively. In order to obtain map for the smaller device, we increase OL to 5.5 to obtain 1 nm fringe spacing for the hologram. Fig.6b shows the lattice deformation scan along vertical direction with -0.65% at the surface of Si and 1.1% at SiGe surface. Fig.6c shows the line scan 3 and 4 parallel to the channel. Line scan 3 and 4 has more noise than line scan 1 and 2. That is due to the data processing,

where the derivative direction is along x direction.

Both strain maps shows strain at the Si surface is highest. In addition, the gradual change between SiGe and Si at the bottom of e-SiGe is observed, indicating SiGe is fully strained to get maximum strain in the channel region (Fig.6b). Along the side wall of e-SiGe, between SiGe and channel Si, there is step function kind of change on both side of Si channel (Fig.6c). Both samples have over grown SiGe above channel Si surface. The lattice constant of SiGe above the surface of channel Si is large (Fig.6b), indicating fully relaxation of SiGe above channel Si surface.

CBED measurement and nano-beam electron diffraction (NBD) measurement

In CBED technique, the shift of high order Laue

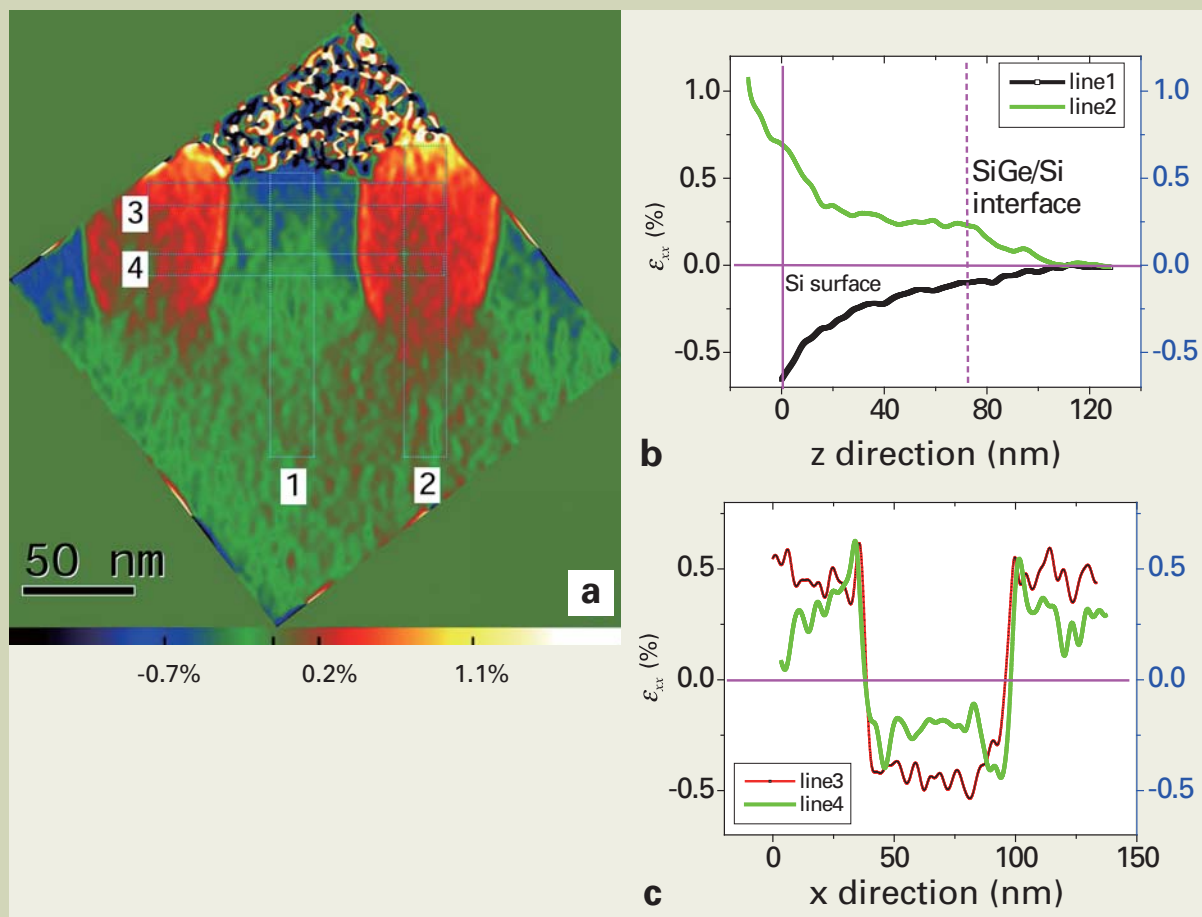


Fig. 6 (a) A strain map of $\langle 220 \rangle, \epsilon_{xx}$, from off-axis dark field hologram. SiGe proximity L is 56 nm. (b) Vertical profile of the strain map under the gate. At the Si surface, -0.65% lattice constant change along x direction is observed (black curve of line scan 1) and at the SiGe surface, lattice constant is 1.1% of unstrained Si lattice (green curve of line scan 2). (c) Horizontal scan under the channel. Red curve is for line scan 3 and green curve is for line scan 4.

zone (HOLZ) lines in the CBED pattern caused by strain is measured by comparing simulated CBED pattern with experimental one [15]. A pattern from unstrained Si is used for calibration. **Fig.7a** shows a dark field STEM image of PFET gate and four typical CBED patterns taken on the $\langle 430 \rangle$ zone axis at different depths below the gate of the same sample measured by dark field electron holography shown in Fig.5. Fig.7b shows channel strain profile along the electron flow direction of $\langle 220 \rangle$ with different depth under gate, reaching maximum compressive strain (lattice deformation) $\sim -0.5\%$ below the gate. The maximum compressive stress of ~ 824 MPa is calculated based on measured lattice deformation value and it is close to the simulated stress value of ~ 850 MPa at the same depth below the gate.

In nano-beam diffraction (NBD) technique,

electron diffraction patterns are generated by a nano electron beam size of ~ 20 nm, positioned in the area of interest. Near parallel and nanometer size of the electron beam is achieved by decreasing convergent angle with a condenser aperture of $10 \mu\text{m}$. Strain can be measured by comparing NBD patterns from the strain area of interest to the unstrained area, by measuring peak position of diffraction spot which has Gaussian distribution of diffraction intensity. **Fig.8** shows a TEM image of PFET transistor with the same sample shown in Fig.5 and Fig.7 by dark field electron holography and CBED measurement, respectively, and corresponding NBD patterns from channel area and Si substrate. The TEM probe is positioned at the center of channel, just below the gate. **Table 1** shows results of channel strain measured by NBD. Average strain measured by NBD along channel direction is about -0.50% , which is

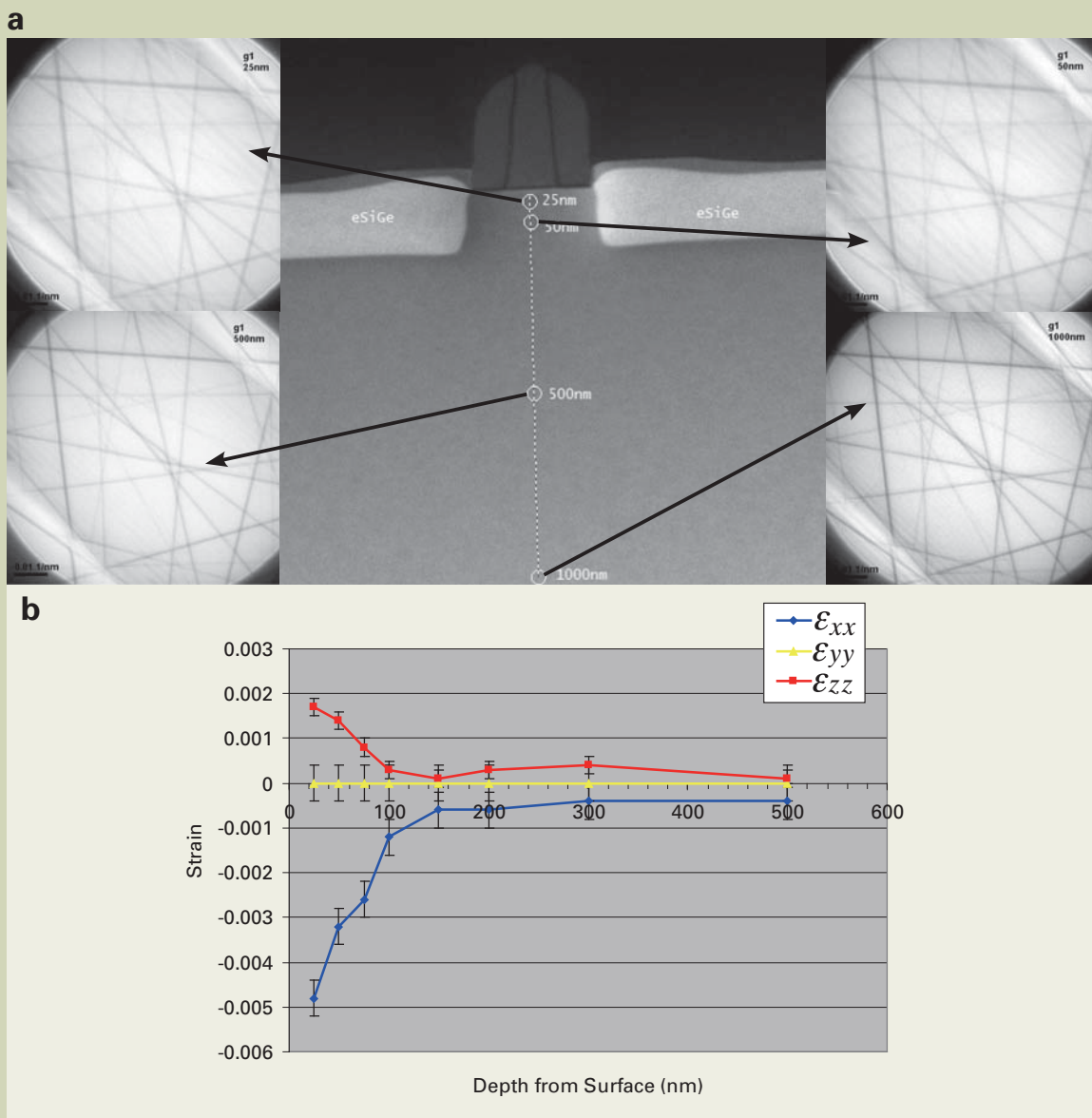


Fig. 7 (a) A dark field STEM image of eSiGe gate and four CBED patterns at different depths: 20nm; 80nm; 500nm and 1000nm.

(b) Strain vs depth measured by CBED of $L=130$ nm samples: Blue curve is the strain along the channel direction, red curve is the strain perpendicular to the channel direction, and yellow curve is the strain parallel to the electron beam direction.

consistent with the measurement by CBED (-0.50%) and dark field electron holography in consideration of difference of spatial resolution with these techniques [16].

Discussion

We measured strain with three different techniques: dark field electron holography, converging beam electron diffraction (CBED), nano-parallel electron beam diffraction. In dark field electron holography measurement, we obtained -0.6% strain at the surface comparing with -0.5% strain obtained by CBED and nano-beam diffraction on the same sample. The difference can be attributed to the spatial resolution difference. For dark field electron holography, the strain map has about 3 nm spatial resolution, which allows us to measure the strain near the top surface, where the strain is highest; while for CBED and NBD, the spatial resolution is about 20 nm, which results in a lower strain measurement on the same sample. Overall, the data are consistent with each other.

These three techniques have their advantage and disadvantage. For instance, dark field electron holography can provide map quickly and it also has a spatial resolution to 3 nm and smaller with dual lens operation. However, the data process cannot tell us whether it is positive or negative strain. Additional

reference is needed, such as nano-beam diffraction to get the sign of the strain. The nano-beam diffraction is easy to acquire, and yet, because the data is usually analyzed after the acquisition, large data storage space is needed for a line scan. It is impractical at this moment to acquire nano-beam diffraction map, because of data storage issue. CBED is in similar situation as of nano-beam electron diffraction. Because of its large data storage space required, CBED measurement is limited to lines scan only for the moment. In the future, nano-beam diffraction map acquisition is possible, if the data storage issue can be resolved.

For nano-beam diffraction, if one wants to decrease the probe size to improve spatial resolution, the converging angle would increase. The relationship between probe size and converging angle in diffraction limited condition can be written as the following equation [17]:

$$\alpha = \frac{0.6\lambda}{d} \dots\dots\dots(11)$$

where α is the converging angle, λ is the wavelength of the electron beam, and d is the probe size. For 3 nm probe, the converging angle increase to about 0.5 mrad from 0.07 mrad of 20 nm probe size. Increasing converging angle results in a disk like diffraction pattern, which means that accuracy of

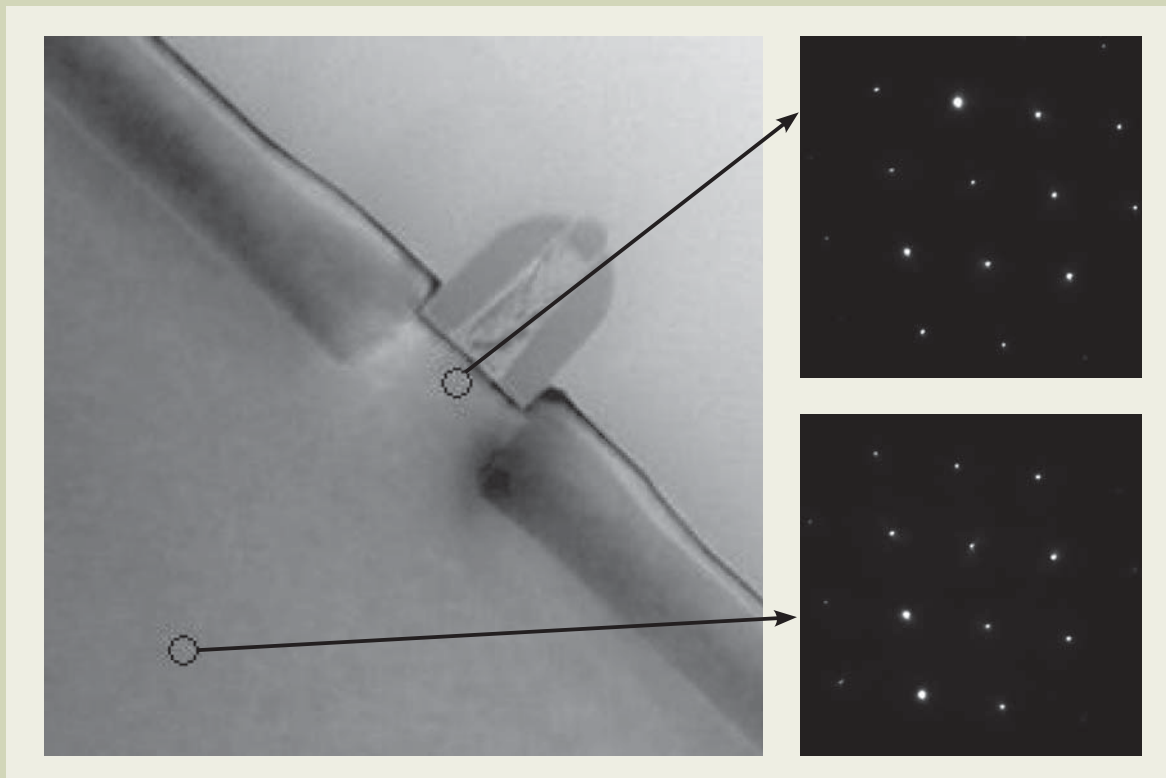


Fig. 8 TEM images of eSiGe and corresponding NBD patterns from channel area and Si substrate.

lattice parameters measurement would get worse. We did the comparison between electron holography measurement with dual lens operation and nano-beam diffraction measurement, we concluded that the spatial resolution of nano-beam diffraction is close to, but not as good as the measurement from dark field electron holography, neither the accuracy of the measurement in comparison with the one of dual lens dark field electron holography [18]. Therefore, dark field electron holography with dual lens operation has its advantages in terms of spatial resolution and accuracy of lattice constant measurement, in addition to the 2-D mapping capability.

Acknowledgement

Authors would like to thank IBM managers, M. Lagus, W. Chu, and A.C. Lamberti for their support and their leadership, which makes this work possible. Helpful discussion with F. Baumann on the data processing of nano beam electron diffraction is acknowledged.

References

- [1] M. Hytch, F. Houdellier, F. Hue, and E. Snoeck, *Nature*, **Vol. 453**, 1086 (2008).
- [2] M. Hytch, E. Snoeck, and R. Kilaas, *Ultramicroscopy* **74**, 131 (1998).
- [3] J. Rouviere and E. Sarigiannidou, *Ultramicroscopy* **106** 1 (2005).
- [4] A. Beche, J.L. Rouviere, J.P. Barnes, and D. Cooper, *Ultramicroscopy*, **111** 227 (2011).
- [5] Y.Y. Wang et al., *Ultramicroscopy*, **101** 63-72 (2004).
- [6] Y.Y. Wang et al., US patent: US 7,015,469 B2 (2006).
- [7] Y.Y. Wang et al., *JEOL News*, **39** 6 (2004)
- [8] Y.Y. Wang et al., *Microscopy Today*, **12** 20 (2004).
- [9] G.F. Missiroli et al., *Journal of Phys. E: Sci. Instrum.*, **14** 649 (1981).
- [10] H. Lichte, *Ultramicroscopy* **64** (1996) 79.
- [11] Y.Y. Wang, J. Li, A. Domenicucci, J. Bruley, to be published.
- [12] M. Born and E. Wolf, **Principle of Optics**, Pergamon Press, Oxford, (1965), Chapter 7.
- [13] A. Domenicucci and Y.Y. Wang, US patent: US 7,102,145 B2 (2006)
- [14] Y.Y. Wang et al., *Microscopy and Microanalysis*, **16**, Supplement S2 590 (2010).
- [15] A. Armigliato et al., *Solid State Phenomena*, 82-84 727-734 (2002).
- [16] J. Li et al., *MRS Symposium Proceedings*, 913157-162 (2006) .
- [17] L. Reimer, *Transmission Electron Microscopy*, Springer-Verlag Berlin Heidelberg, 1984 and 1989, p.104.
- [18] Y.Y. Wang and F. Baumann, unpublished result.

Table 1 Channel strain measured on <220> and <002> diffraction spot by NBD.

Gate Number	ϵ_{220}	ϵ_{002}
Gate1	-0.40%	+0.18%
Gate2	-0.60%	+0.28%
Gate3	-0.50%	+0.16%
Gate4	-0.40%	+0.16%
Gate5	-0.40%	0
Gate6	-0.40%	+0.24%
Gate7	-0.46%	+0.23%
Gate8	-0.65%	-0.35%
Average	-0.50%	+0.20%

Adapting a JEM-2100F for Magnetic Imaging by Lorentz TEM

Amit Kohn and Avihay Habibi

Department of Materials Engineering and the Ilse Katz
Institute for Nanoscale Science and Technology, Ben-Gurion
University of the Negev

Lorentz TEM enables to map quantitatively magnetic induction fields in the sample. A specifically designed objective lens, a coherent electron source, and a biprism filament can achieve magnetic imaging at the nanometer scale through off-axis electron holography experiments. However, this equipment is specialized and therefore not suited to many microscopy labs. In this article, we describe an adaptation of a conventional JEM-2100F for Lorentz phase microscopy, namely Fresnel-contrast imaging. Since a biprism filament is installed on this microscope, we evaluate the capabilities of the Fresnel-contrast magnetic imaging. We show that a relatively simple and low-cost adaptation enables quantitative magnetic and electrostatic mapping on a conventional TEM.

Introduction

The development of new magnetic materials, e.g. for information storage devices, requires the characterization of the structural, chemical, electronic and magnetic properties of these materials at the nanometer and even atomic scale. Transmission electron microscopy (TEM) is a versatile tool for materials characterization that contributes significantly towards all these goals [1]. Amongst the capabilities of electron microscopy is the so-called 'Lorentz TEM', which enables to map quantitatively the magnetic and electrostatic fields of the material at the nanometer scale. In addition, *in situ* experiments are performed to image the micromagnetic structure while subjecting the specimen to magnetic and electrical fields [2, 3].

A combination of a specifically designed objective lens, a coherent electron source, and a biprism filament enables magnetic mapping at a spatial resolution in the nanometer scale, e.g. References [4,5]. However, such a combination is specialized and expensive, therefore not suited for most electron microscopy labs.

In this report, we describe an adaptation of a conventional JEM-2100F for Lorentz TEM, and show that achieving Fresnel-contrast imaging is straightforward. Since this microscope has a coherent electron source, and is equipped with a biprism filament, we also report on the off-axis holography characteristics under these conditions. Electron holography enabled us to examine the quantitative capabilities of Fresnel-

contrast imaging in the modified TEM for magnetic mapping.

The outline of the paper is as follows: The requirements for adapting a microscope for Lorentz TEM are presented. Following this, the modifications of the JEM-2100F are described. The relevant optical parameters of the adapted microscope are then characterized. We present an example of magnetic imaging both in Fresnel-contrast, and electron holography in order to demonstrate and evaluate the quantitative capability of the adapted microscope. Finally, we show that low-angle electron diffraction is also possible using free-lens control.

Requirements

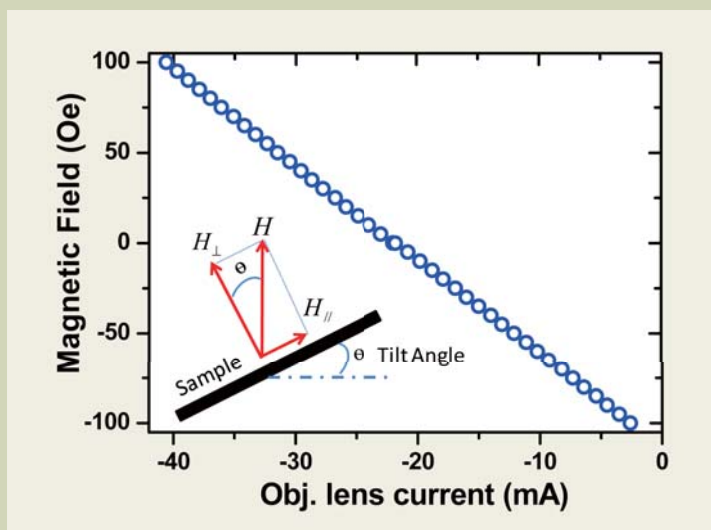
The initial requirement for performing Lorentz TEM is to position the sample in a region free from external magnetic fields. Many samples of interest are based on soft magnetic materials, namely their coercivity is under 50 Oe. Consequently, the magnetic field in the region of the sample should be less than several Oe. In addition, during the insertion of the holder through the load-lock, the sample should not be subjected to significant stray magnetic fields from the column. Therefore, the first stage is to close the current supply to the objective lens, and use the objective mini-lens instead (calculated focal length of 42 mm, 10% accuracy).

Lorentz TEM is often used for *in situ* experiments. A typical research interest is to examine the development of the micromagnetic structure with applied external field. A basic method to achieve this is by using the objective lens to generate a magnetic field along the optic axis. The sample is then tilted to apply both an

Be'er-Sheva 84105, Israel

E-mail: akohn@bgu.ac.il

Fig. 1 The magnetic field along the optic-axis of the microscope as a function of applied current to the objective lens. Inset: tilting the sample enables to apply a magnetic field also in the plane of a thin film.



in-plane and out-of-plane magnetic field (see inset of **Figure 1**). Tilting of the sample is necessary because for soft magnetic materials, the magnetic moments reside in-plane. In recent years, there is increased technological interest in perpendicular magnetic media, which is based on hard magnetic materials. Here, there is an advantage to apply large magnetic fields (possible up to approximately 2 Tesla using the objective lens) along the optical axis, perpendicular to the sample plane.

When using the objective mini-lens, the magnification range should enable magnetic mapping at nanometer resolution: A pixel calibration of the CCD at around 1 nm is sufficient for Fresnel-contrast imaging.

Finally, the aberrations of the microscope should be characterized in order to evaluate the imaging capabilities of the microscope. For Lorentz TEM in a conventional microscope, the relevant aberrations are mainly the spherical aberration, C_s , and the defocus distance. Measuring C_s and calibrating the defoci distances can then enable quantitative analysis of the Fresnel-contrast images by comparison to image simulations.

Adaptation and characterization

The first step of the adaptation was to extend the magnification range of the objective mini-lens. Lens settings were obtained from JEOL to extend the magnification from the usual maximum setting of 6kX up to 40kX. The latter magnification is sufficient for the spatial resolution required both in Fresnel-contrast imaging and for electron holography. At a nominal magnification of 40kX, the pixel calibration is approximately 0.25 nm on a 2048×2048 Gatan Ultrascan Charge-Coupled-Device (CCD).

At this stage, the residual field was measured with a Hall probe that was incorporated onto a sample holder. The typical residual magnetic field measured on the sample was approximately 190 Oe. While this residual field is small compared to the regular operation of the objective lens, it will saturate most soft magnetic materials.

Reduction of the remnant field is necessary, and can be achieved by applying a current on the objective lens.

Setting 34.4 mA to this lens decreased the residual field to approximately 0.1 Oe. The required current can be reduced by degaussing the objective lens, namely cycling the applied current on the objective lens in decreasing magnitude from 1 Ampere. After the degaussing procedure (approximately 2 minutes), a reduced current of under 22 mA is applied to reduce the remnant field to approximately 0.1 Oe.

The stability of this low field was examined to determine the duration of experiments that can be undertaken. The residual field increased at a rate of 0.2-0.3 Oe per hour, meaning that experiments spanning 4 hours can be conducted while ensuring that the residual field at the sample is less than 1 Oe. The stability of the residual field was examined with the change of magnification. Starting from the highest magnification setting of 40kX, the field increased approximately linearly up to 0.5 Oe when reducing the magnification down to 8kX. When the magnification setting was further reduced, the residual field increased to over 4 Oe at 6kX, further increasing to above 6 Oe at the lowest magnifications. A similar change of the residual field was measured when starting at low magnifications and then increasing the magnification. This observation can be explained by the new lens setting of the objective mini-lens. Since the magnification range was increased beyond 6kX, the current applied to the objective mini-lens changes, which results in a change in the magnetic field applied to the sample.

The residual field was also examined with the change of current or defocusing of the objective mini-lens. This measurement is relevant for Fresnel contrast imaging, where the typical defoci distances span from tens to hundreds of micrometers. For underfocus, the field increased to over 0.2 Oe, 0.3 Oe, and 0.4 Oe up to defoci distances of 100 μm , 400 μm , and 900 μm , respectively. For overfocus, the residual field was stable, below 0.3 Oe, up to a defocus distance of 900 μm .

We conclude that a residual field of under 1 Oe can be maintained in the sample region with the use of the objective mini-lens over a wide range of magnifications and defoci distances, and during experiments conducted for several hours.

After reducing the residual field, the magnetic field was measured when removing and inserting the sample holder with the Hall probe. A maximum field of 2 Oe was measured during this process. Therefore, the insertion of the sample is not expected to affect the micromagnetic structure of the sample.

As previously explained, the objective lens can be used to apply a magnetic field on the sample. In Figure 1, the field, measured in the applied current range of approximately 40 mA to 2 mA is presented, equivalent to magnetic fields spanning between -100 to +100 Oe. This result shows a linear response, which can be further extended by increasing the current on the objective lens.

The next stage is to characterize the aberrations of this Lorentz setup. For magnetic imaging and phase reconstruction at the nanometer scale resolution, the two important aberrations to measure are the spherical aberration, C_s , and the defocus distance. Calibrating the defoci distances as a function of the objective mini-lens current is also required for choosing the correct Fresnel-contrast conditions and quantifying the results.

The two aberrations were measured using the methodology outlined in Reference [6]. **Figure 2(a)** shows the calibration of the defoci distances. The minimum

defocus step is $3.02 \pm 0.01 \mu\text{m}$. This focal step is small enough for Fresnel contrast imaging. However, when finer control is needed, for example to achieve the Gaussian defocus, then the z-axis of the stage can mechanically translate the sample by steps of $0.3 \mu\text{m}$ (verified by the above mentioned methodology). **Figure 2(b)** shows the measured C_s for the various defoci distances. The average measurement of the spherical aberration is $4.61 \pm 0.17 \text{ m}$, while the chromatic aberration was calculated to be 87 nm. The point resolution of this low magnification, Lorentz set-up is therefore approximately 2 nm.

Figure 3 is a comparison of bright-field TEM images of gold nanoparticles, sputter-deposited on an amorphous carbon film, obtained with the adapted Lorentz mode (left) and with the conventional TEM imaging (right). While degradation in the image quality is observed, a spherical aberration of several meters still enables imaging with nanometer resolution.

We now demonstrate the electron holography capabilities of this setup. The JEOL biprism filament ($0.6 \mu\text{m}$ in diameter) was positioned perpendicular to the insertion direction into the microscope column in order to minimize mechanical vibrations. **Figure 4(a)** shows both the fringe spacing and hologram width as a

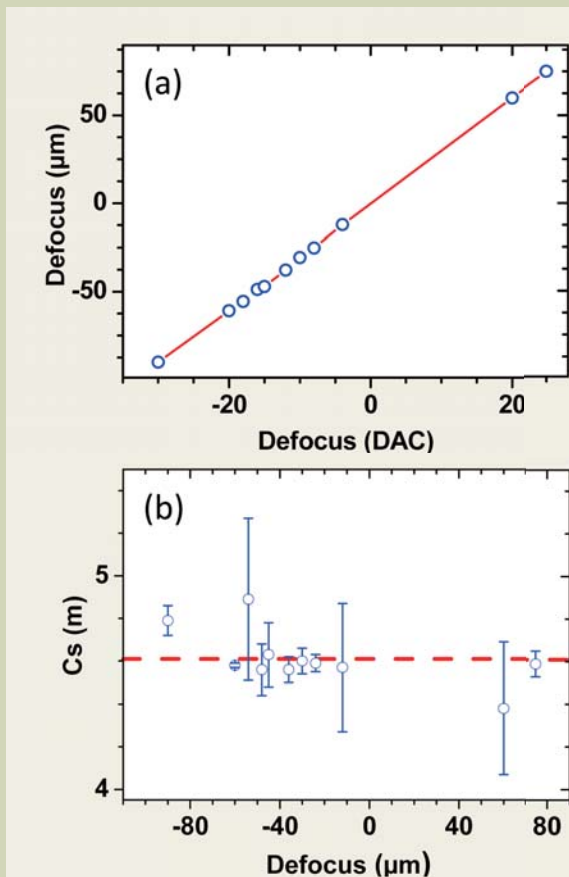


Fig. 2 (a) Defocus distance as a function of DAC setting of the objective mini-lens (b) coefficient of spherical aberration, C_s , measured at various defoci distances.

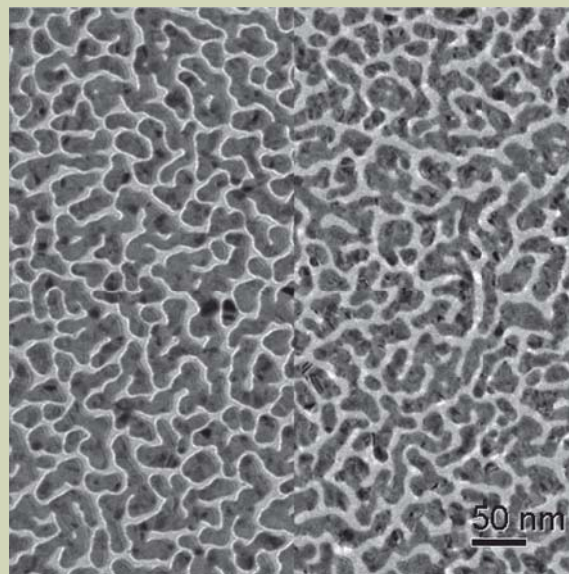


Fig. 3 Comparison of bright-field TEM imaging of gold nanoparticles on a carbon film recorded with the adapted Lorentz setting (left) and conventional imaging (right). The nominal magnification is 40kX.

function of applied voltage to the biprism. Figure 4(b) shows the contrast of these holograms, which in all cases was found to be over 10%. The acquisition time was set at 2 seconds. Longer recordings of holograms resulted in a deterioration of the contrast due to instabilities, mostly associated with the laboratory environment.

The holograms were recorded at a nominal magnification of 40kX. The width of the hologram that can be achieved in the low-magnification, Lorentz setting is larger than in regular TEM operation, reaching up to 1.2 μm . Such an increase may still not be sufficient for some magnetic imaging applications, for example when a large field of view across a thin film is required, or when the interaction between patterned elements or particles is examined.

Example: magnetic imaging of a patterned element

We demonstrate the magnetic imaging capabilities of the adapted Lorentz TEM on patterned magnetic elements. These elements were fabricated by depositing nominally 40 nm thick Permalloy ($\text{Ni}_{80}\text{Fe}_{20}$) films on

Si_3N_4 membranes using electron-beam lithography and lift-off processing. Here, we show an example of a square element, with a side length of 0.5 μm . A bright-field image, obtained in the Lorentz mode, of this element, presented in **Figure 5(a)**, highlights the polycrystalline structure of the Permalloy film. Figures 5(b,c) are Fresnel-contrast images, under- and over-focus, respectively, of 399 μm . Qualitatively, the bright and dark bands in the image, originating from domain walls, show a micromagnetic flux-closure structure. This structure can be characterized quantitatively by applying the ‘Transport-of-Intensity’ equation (TIE). The TIE is derived from a paraxial form of the flow conservation equation, which is obtained by applying the Schrödinger equation to an electron in a field-free region.[7, 8] Phase reconstructions were carried out using the Fourier transform-based approach of solving the TIE developed by Nugent *et al.*, (e.g. References [9, 10]) with the commercially available ‘QPt’ software.[11] Alignment of the defocused images was done using the ‘Align 3_TP’ plugin for ImageJ. [12]

An example of phase reconstruction for defocused images of 399 μm is shown in **Figure 6(a)**. The result is presented in the form of an equiphase contour map,

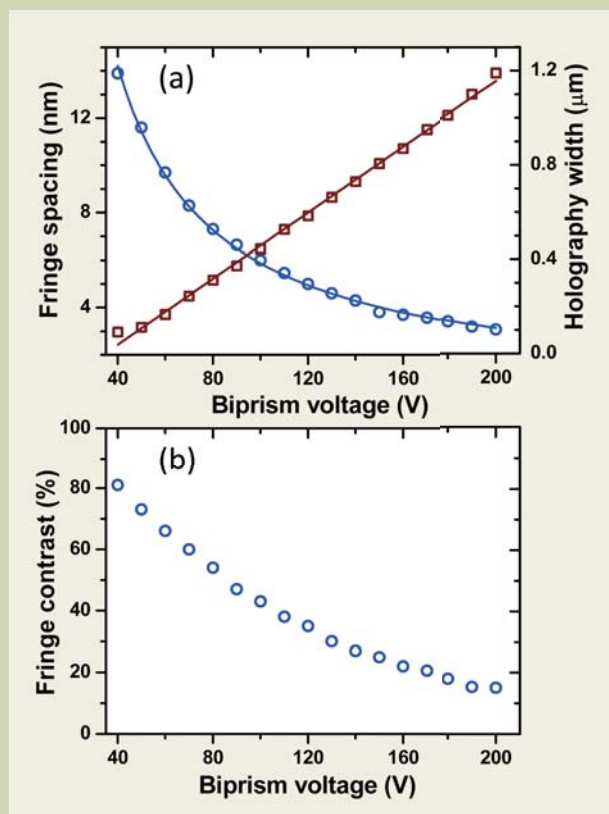
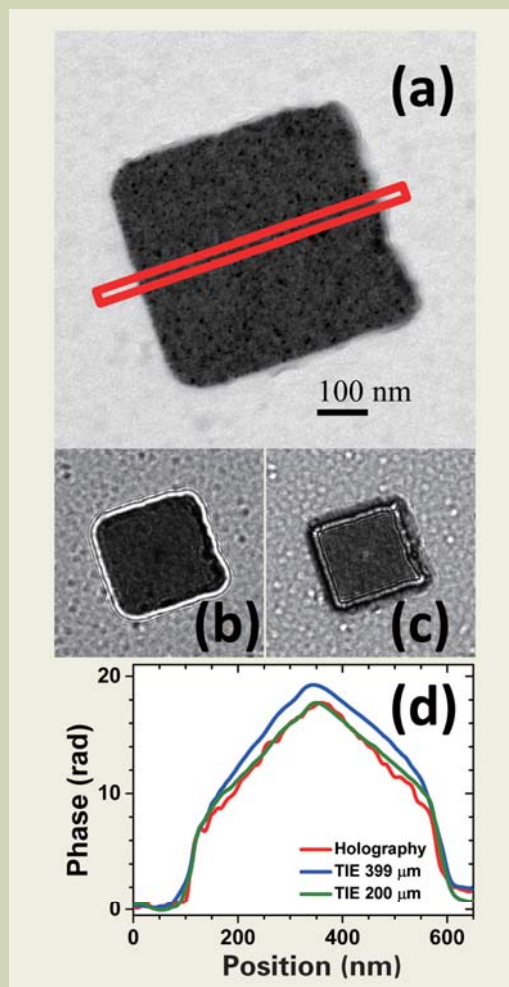


Fig. 4 Fringe spacing (a, left), off-axis hologram width (a, right), and fringe contrast (b) as a function of voltage applied to the biprism filament.

Fig. 5 (a) Bright-field TEM image of a nominally 40 nm thick square Permalloy element, 500 nm \times 500 nm, patterned on a Si_3N_4 membrane. (b, c) Fresnel-contrast images, under-focus and over-focus, respectively, of 399 μm defocus distance. (d) Comparison of the reconstructed phase values along the direction denoted schematically by the red line in (a) for the off-axis holography measurements (red line) and the TIE phase reconstructions of Fresnel contrast images at 201 μm (green line) and 399 μm (blue line) defoci distances.



spaced at 1 radian between lines. This representation is convenient for magnetic mapping because the direction of the induction vector is along the equiphase line, and the magnitude of the vector is determined by the proximity of the contour lines (or gradient) perpendicular to the vector direction.

To test the reconstructed phase, we compare this result to off-axis electron holography measurements and Fresnel-contrast image simulations. Figure 6(b) is a phase-contour map of the same square Permalloy element measured by electron holography. Note that this result demonstrates two relative drawbacks compared to Fresnel-contrast imaging: the limited field of view, and the lack of a reference hologram from the vacuum, which degrades the quality of the reconstruction. Figure 6(c) is a phase-contour map calculated theoretically: The micromagnetic structure was first found by solving the time-dependent Landau-Lifshitz-Gilbert equations with the ‘OOMMF’ NIST package.[13] The magnetization distribution enables to determine the phase change of the electron wave. Following this, Fresnel-contrast Lorentz TEM images were simulated based on a code developed by McVitie *et al.*[14] The calculation of the Fresnel-contrast images used here also include the optical parameters of this Lorentz TEM setting, the electrostatic potential of the sample, the change in amplitude of the electron wave due to the sample, and the shot-noise of the CCD. Finally, the phase was reconstructed from these simulated images using the TIE approach, shown in Figure 6(c).

A comparison of the phase values along the direction denoted schematically by the red line in Figure 5(a) is shown in Figure 5(d) for the off-axis holography measurements and the TIE reconstruction of Fresnel-contrast images at 201 μm and 399 μm . These phase line-scans show the typical electrostatic step at the edge of the element due to the change in the mean inner potential as well as the linear slopes within the sample due to the magnetic domain structure.

These comparisons are in agreement with the expected theoretical values, and show that quantitative magnetic mapping is indeed achieved to a good level in the adapted Lorentz TEM. Increasing the defocus distance increases the Fresnel contrast, which is useful for qualitative analysis. However, both the magnetic reconstruction and spatial resolution are degraded compared to reconstructions achieved with smaller defocus distances or electron holography.

Finally, an additional, indirect method to characterize the micromagnetic properties of the sample in the TEM is by low-angle electron diffraction (LAED). In this mode, the splitting of the central undiffracted beam is observed due to the Lorentz force. In the adapted JEOL JEM-2100F, this measurement was demonstrated by using ‘free-lens control’ of the intermediate lenses until the back-focal plane was observed on the viewing screen. **Figure 7** shows an example of a LAED obtained from a continuous Permalloy film sample, 45 nm thick. Figure 7(a) is a Fresnel-contrast image of a single domain region in the film showing typical ripple-contrast. The inset in the top left part of the image shows the central undiffracted beam in the back focal plane. In comparison, Figure 7(b) is a Fresnel-contrast image of a region including two magnetic domains. The domain wall is clearly visible as the white band, and the change of ripple-contrast on either side of the wall indicate the orientation of the magnetic moments within the domains. In this case, the LAED, shown in the inset in the top left hand corner of Figure 7(b) shows the splitting of the central beam. The

deflection between the two spots is under 60 μrad , namely more than two orders of magnitude smaller than deflections measured for typical Bragg reflections.

Summary

Characterization of magnetic fields at the nanometer scale is important for the development of new materials

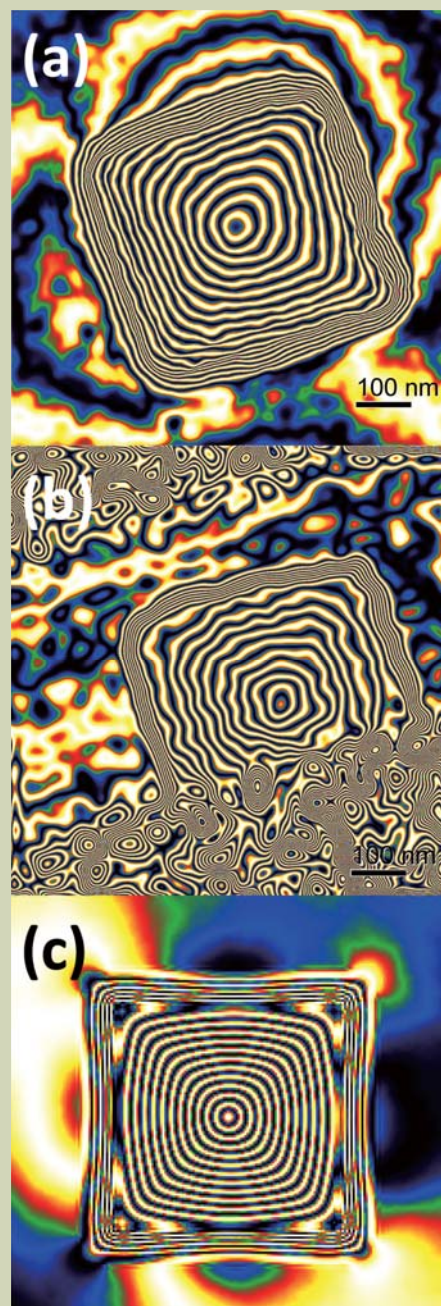


Fig. 6 Equiphase contour maps of the Permalloy square element derived from (a) TIE analysis of Fresnel-contrast images (399 μm defocus), (b) off-axis electron holography, (c) Fresnel-contrast image simulations from micromagnetic calculations, followed by phase reconstruction using the TIE approach. Note that the image simulations include specific characteristics of the adapted JEM-2100F for Lorentz TEM.

and devices. In this paper, we describe the adaptation of a conventional JEM-2100F to enable such measurements. Using a relatively simple and low-cost approach, Fresnel-contrast imaging is achieved while the sample is subjected to a field lower than 1 Oe during extended periods and over a wide range of microscope settings. Quantitative magnetic and electrostatic mapping of sub-micrometer magnetic structures at nanometer resolution has been demonstrated.

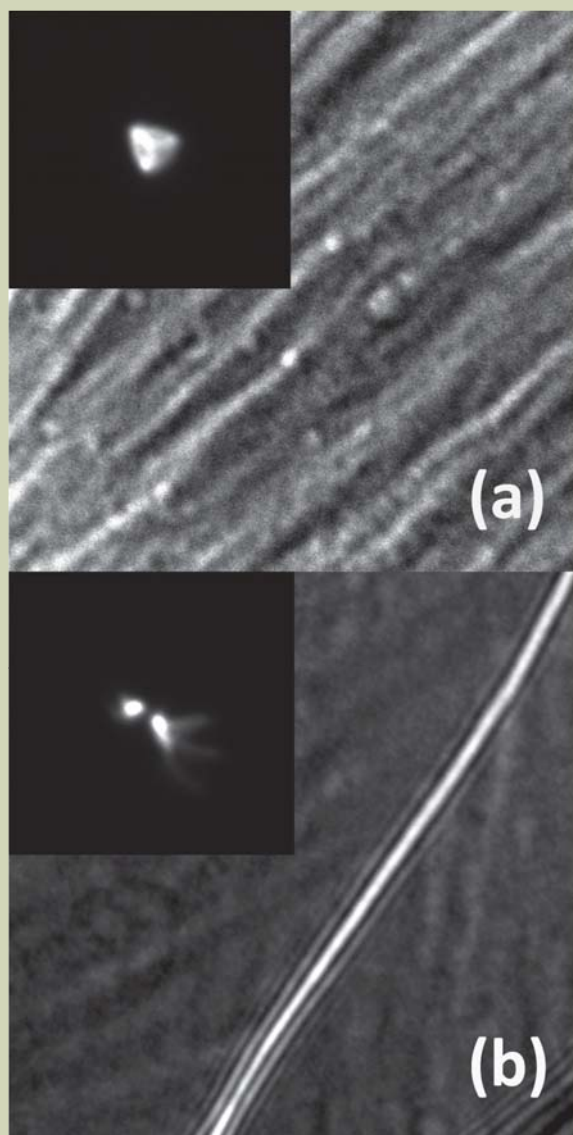


Fig. 7 Low-angle electron diffraction of a Permalloy film, 45 nm thick. (a) Fresnel-contrast image of a single domain region in the film (inset) LAED of this region (b) Fresnel-contrast image of a domain wall and two domain regions (inset) LAED of this region showing two spots at approximately 60 μ rad separation.

Acknowledgments

The magnetic field neutralizer system was designed and built by Adrian Goodchild and Dave Greenshields in the Department of Physics, University of Warwick, UK.

We thank the assistance of Tom Hayward and Dan Allwood from the University of Sheffield, UK for supplying the lithographically patterned Permalloy elements.

The authors are grateful to Dorin Geiger and Hannes Lichte, Triebenberg Laboratory, Technische Universität Dresden, and Véronique Pierron-Bohnes and Corinne Ulhaq, Institut de Physique et de Chimie des Matériaux de Strasbourg for instruction and advice on off-axis electron holography.

We thank the technical assistance of JEOL (UK) Ltd., and AVBA Hitech Services, Israel.

References

- [1] A. K. Petford-Long, A. Kohn, T. Bromwich, V. Jackson, F. Castano, and L. J. Singh, Application of TEM to the development of information storage materials, *Thin Solid Films*, **505** (1-2) 10-15 (2006).
- [2] A. Kohn, J. Dean, A. Kovacs, A. Zeltser, M. J. Carey, D. Geiger, G. Hrkac, T. Schrefl, and D. Allwood, Exchange-bias in amorphous ferromagnetic and polycrystalline antiferromagnetic bilayers: Structural study and micromagnetic modelling, *J. Appl. Phys.*, **109**(8) 083924 (2011).
- [3] A. Kohn, C. Wang, A. K. Petford-Long, S. Wang, and R. C. C. Ward, Magnetization reversal processes in epitaxial Co/Fe bi-layers grown on MgO(001), *J. Appl. Phys.*, **103** (6) 063918 (1-9) (2008).
- [4] M. A. Schofield, M. Beleggia, Y. Zhu, and G. Pozzi, Characterization of JEOL 2100F Lorentz-TEM for low-magnification electron holography and magnetic imaging, *Ultramicroscopy* **108** 625–634 (2008).
- [5] M. A. Schofield, M. Beleggia, J. W. Lau, and Y. Zhu, Characterization of the JEM-2100F -LM TEM for Electron Holography and Magnetic Imaging, *JEOL news* **42** 2-7 (2007).
- [6] O.L. Krivanek, *Optik* **45** 97 (1976).
- [7] M. R. Teague, *J. Opt. Soc. Am.* **73**, 1434 (1983).
- [8] A. Barty, D. Paganin, and K. Nugent, in *Magnetic Imaging and its Applications to Materials*, edited by M. De Graef and Y. Zhu, Academic Press, San Diego, 2001.
- [9] D. Paganin and K. A. Nugent, *Phys. Rev. Lett.* **80** 2586 (1998).
- [10] A. Kohn, A. K. Petford-Long, and T. C. Anthony, Determining the Magnetic Potential in Patterned Materials Using Energy-Dependent Lorentz Phase Microscopy, *Phys. Rev. B.* **72** 014444 (2005).
- [11] QPt for Digital Micrograph, IATIA and HREM Inc.,
- [12] W.S. Rasband, ImageJ, National Institutes of Health, Bethesda, Maryland, USA, <http://rsb.info.nih.gov/ij/>, 1997-2003.; J. A. Parker, 'Align3_TP', Beth Israel Deaconess Medical Center Boston, Maryland, USA, <http://www.med.harvard.edu/jpnm/ij/plugins/Align3TP.html>
- [13] M. J. Donahue and D. G. Porter, *OOMMF User's Guide*, Version 1.0 Interagency Report NISTIR 6376 National Institute of Standards and Technology, Gaithersburg, MD (Sept 1999).
- [14] S. McVitie and M. Cushley, *Ultramicroscopy* **106** 423 (2006).

A New WDS Spectrometer for Valence Electron Spectroscopy Based on Electron Microscopy

Masami Terauchi[†], Hideyuki Takahashi^{††}, Nobuo Handa^{††},
Takanori Murano^{††}, Masato Koike^{†††}, Tetsuya Kawachi^{†††}, Takashi
Imazono^{†††}, Masaru Koeda^{††††}, Tetsuya Nagano^{††††}, Hiroyuki
Sasai^{††††}, Yuki Oue^{††††}, Zeno Yonezawa^{††††} and Satoshi Kuramoto^{††††}

[†] IMRAM, Tohoku University

^{††} EO Peripheral Component Business Unit, JEOL Ltd.

^{†††} Quantum Beam Science Directorate, Japan Atomic Energy Agency

^{††††} Device Department, SHIMADZU Corp.

A new WDS spectrometer for a transmission electron microscope has been constructed. This spectrometer can cover an energy region from 50 eV to 3800 eV by using four aberration-corrected gratings for flat-field optics. By using a newly designed and manufactured grating of JS50XL for 50-200 eV, soft-X-ray emission spectra of simple metals of Mg, Li, Al and Be were measured. Those intensity profiles correspond to partial density of states of valence electrons (bonding electrons) and also showed clear Fermi edges (top of the occupied state). At the Fermi edge of Mg-L emission (49.5 eV), an energy resolution was evaluated to be 0.16 eV. Si-L emission spectra of Si and TiSi₂ show a difference in those intensity distributions, indicating different valence-electron states for those materials. A comparison of B-K emission spectra of CaB₆ and LaB₆, which were obtained by using another grating of JS200N, is shown. A clear Fermi edge was also observed for LaB₆ at about 187 eV with an energy resolution of 0.4 eV.

Introduction

Recent tendency for miniaturizing semiconductor devices and developing new functional materials with nanometer scale size are eager for new evaluation methods not only for structural and elemental analyses but also for state analysis (physical properties) based on microscopy. Physical properties strongly depend on the electronic structure of valence electrons (bonding electrons). Thus, a high energy-resolution spectroscopy for valence electrons with a high spatial-resolution is extremely important to evaluate new functional materials. One promising way is an introduction of a valence-electron spectroscopy into electron microscopy.

Electron energy-loss spectroscopy (EELS) based on transmission electron microscopy (TEM) can obtain excitation spectra of valence electrons (transition “a” in **Fig.1**), which include information on dielectrics (refractive index, bandgap energy, interband transition

energies), from identified nanometer-scale specimen areas. The imaginary part of a dielectric function is proportional to the joint density of states of valence and conduction bands. Recent developments of monochromators for TEM enable us to examine physical properties in near infra-red energy region of nanoparticles [1] and also fine structures of partial density of states of conduction bands of nanometer scale specimen areas [2]. However, the density of states of valence electrons (bonding electrons) cannot be directly obtained by EELS.

For obtaining the density of states of valence electrons, soft-X-ray emission spectroscopy (SXES) instruments by using aberration corrected (varied-line-spaced) gratings have been introduced to transmission electron microscopes [3,4]. Especially, emissions due to electronic transitions from valence bands to an inner-shell level (transition “d” in Fig.1) are important. X-ray emissions due to transitions “c” in Fig.1, which is usually used for elemental analyses, do not have information on the density of states of valence bands. Combinations of SXES and EELS can figure out the total electronic structure from valence bands to conduction bands [3,5]. The energy resolutions of those SXES instruments

2-1-1 Katahira, Aoba-ku, Sendai 980-8577, Japan.

E-mail: terauchi@tagen.tohoku.ac.jp

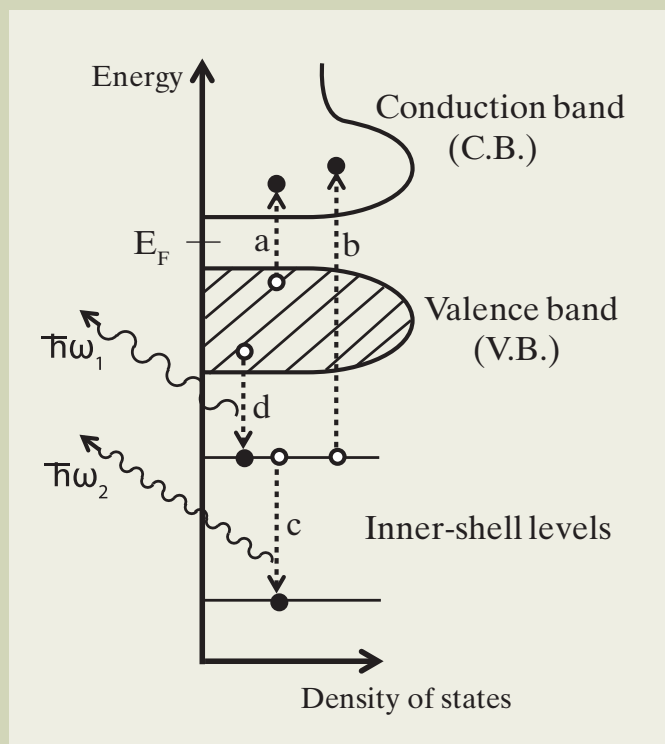


Fig. 1 Schematic diagram of electronic structure and electronic transitions relating to electron energy-loss spectroscopy (a and b) and X-ray emission spectroscopy (c and d). Soft-X-ray emission due to transition d gives us information on electronic states of valence electrons (bonding electrons).

are better than 1 eV for energies lower than 400 eV. This resolution is comparable to those of conventional X-ray photoelectron spectroscopy (XPS) or electron spectroscopy for chemical analysis (ESCA) instruments. The charging problem of a specimen in XPS/ESCA experiments, which causes a shift of a spectrum, does not come out in SXES experiments, because a soft-X-ray emission originates from an electronic transition inside a material. Furthermore, SXES instruments do not need an ultra-high vacuum condition due to a larger absorption length of soft-X-ray photons than a few tens nm. However, SXES method is inferior in detection efficiency compared to that of EELS due to a small efficiency of soft-X-ray emission and a small solid-angle for detection of spectrometers. Thus, an application of those SXES instruments to an electron probe microanalyzer (EPMA), which usually uses a much more beam current than that of a transmission electron microscope, overcomes the problem of pure S/N in soft-X-ray emission spectra obtained by transmission electron microscopes. This application will provide a valence electron spectroscopy method to examining an origin of a physical property with microscopy for a wide variety of materials developments.

In this report, results of a new SXES spectrometer attached to a transmission electron microscope are presented.

Instrumentation[6]

The present test SXES instrument has been designed to cover an energy region from 50 eV to 3800 eV by using four aberration-corrected (varied line-spaced; VLS) laminar-type gratings. This SXES spectrometer is based on flat-field grazing-incidence optics. Since a solid angle of this optics is small, it is

not so difficult to incorporate an SXES instrument with an electron microscope without any change in electron optics. A demerit of a small detection efficiency due to a small collection angle can be recovered by a few times using X-ray collection mirrors and dominantly by a high beam-current in case for EPMA/SEM.

Figure 2(a) shows a photo of the test SXES instrument attached to a transmission electron microscope of JEM-2010. This spectrometer is composed of a pair of X-ray collection mirrors, four VLS gratings and two detectors. The X-ray collection mirrors have gold surfaces and a length of 14 cm along the incoming X-ray path. Two VLS gratings (JS50XL and JS200N) among the four were used for present experiments. The upper detector in Fig.2(a), which is a CsI-coated two-stage multi-channel plate (MCP) optically coupled with a conventional front-illumination-type charge-coupled device (CCD) camera, is usually used for a lower energy region. An effective pixel size on MCP plane was evaluated to be 24 μm . Another detector (lower one) is a back-illuminated type CCD (direct CCD) without an anti-reflection coating with a pixel size of 12 μm . This smaller pixel sized detector has an advantage for obtaining high energy-resolution for a smaller energy-dispersion condition for higher energy X-rays.

A combination of a VLS grating of JS50XL, which covers from 50 eV to 200 eV, and the MCP+CCD detector was applied for measurements of Mg-L, Li-K, Al-L, Si-L and Be-K emissions. This grating has an Au-surface and an average groove density of 1200 lines/mm. The incident angle of X-ray is designed to be 86 degs. A solid angle for this combination with present X-ray collection mirrors was calculated to be 2.1 msr. The optics of this grating is shown in Fig.2(b).

The same one has already been applied to EPMA [7]. For B-K emission measurements, a VLS grating of JS200N, which covers from 150 eV to 350 eV, and the direct-CCD detector were applied. This second grating has a Ni-surface and an average groove density of 1200 lines/mm. The incident angle has been designed to be 87 degs, which is a little smaller than that of JS50XL.

In the following experiments, an accelerating voltage of the TEM was 100 kV. Beam size on

specimen area was varied from 0.6 μm to 5 μm to escape from irradiation damage. A parameter AQ ($\text{nA}\cdot\text{min}$), a beam current (nA) \times an acquisition time (min), is used for presenting acquisition conditions in this report.

Mg-L and Li-K emission spectra

Figure 3(a) shows a Li-K emission spectrum (V.B. \rightarrow K-shell) of Li and a Mg-L emission spectrum

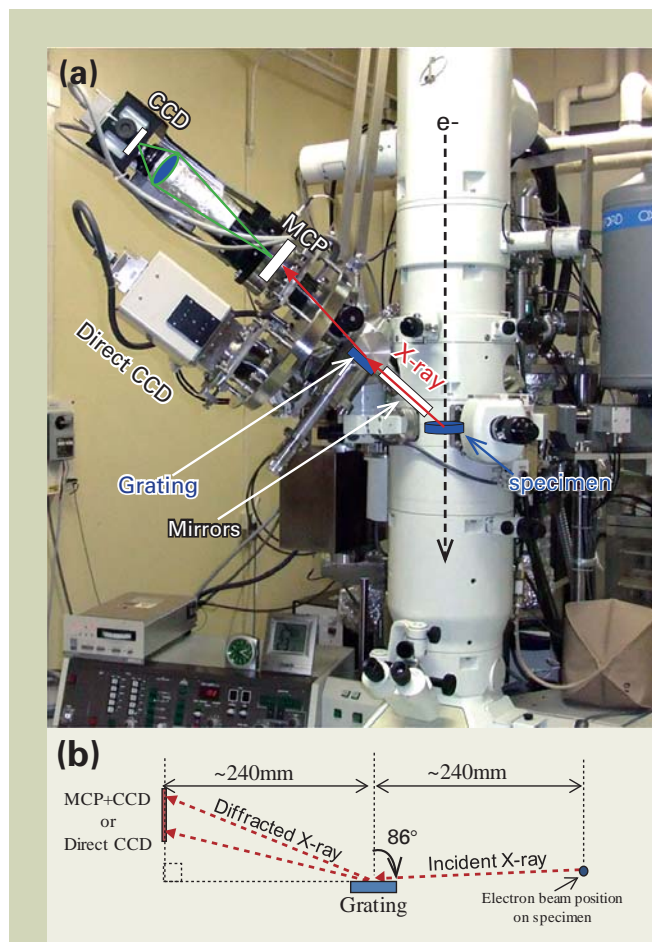


Fig. 2 (a) Photo of a newly constructed SXES instrument attached to a transmission electron microscope of JEM-2010. Upper detector is a multi-channel plate (MCP) optically coupled with a conventional front-illumination-type CCD camera. Lower one is a back-illuminated type CCD camera for direct detection of soft-X-ray. (b) A schematic figure of optics of the newly designed and manufactured grating of JS50XL for 50-200 eV.

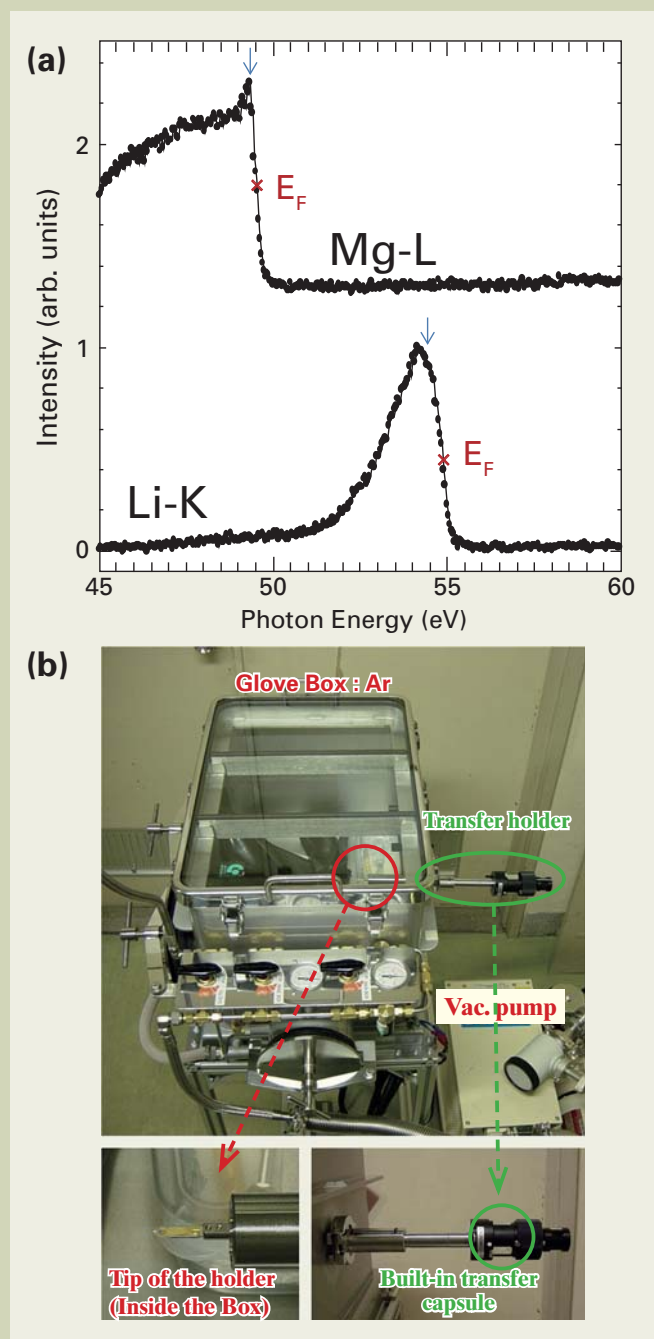


Fig. 3 (a) Mg-L emission spectrum (V.B. \rightarrow L-shell) of Mg-metal and Li-K emission spectrum (V.B. \rightarrow K-shell) of Li-metal. The energy resolution at E_F of the Mg-L emission spectrum was evaluated to be 0.16 eV. Core-hole effect in Li-K emission, suppression of intensity just below E_F , is seen. (b) A glove box and a specimen transfer holder, attached to the glove box, used for a preparation of Li-metal specimen.

(V.B.→L-shell) of Mg. AOs for Li-K and Mg-L were 950 nA·min and 400 nA·min, respectively. Since Li-metal is easily oxidized and/or nitrized in the air, a piece of Li-metal was mounted on a specimen transfer holder (JEOL-EM050611) attached to a glove box, and transferred to the SXES-TEM instrument. During the preparation and transfer processes, the specimen was kept under an Argon atmospheric condition. For this purpose, Ar gas was also used for the pre-pumping system of the transmission electron microscope. This transfer system is shown in Fig.3(b). A negligible hump at about 50 eV of Li-K emission may indicate little oxidization of metal surface during the specimen preparation.

Each spectrum shows a clear Fermi edge at the right-hand side end of each intensity distribution. A Fermi energy position (E_F), marked by x at the middle of each Fermi edge, corresponds to the top of the occupied energy level of each metal. The energy resolution at E_F of the Mg-L emission spectrum was evaluated to be 0.16 eV. Li-metal and Mg-metal are simple metals. Then, the electronic structure can be described by a free electron model. Thus, intensity distributions $I(E)$ of the lower part (apart from E_F) of those spectra are expected to be written as $I(E)_{Mg-L} \propto E^{1/2}$ (density of states of s -symmetry) and $I(E)_{Li-K} \propto E^{3/2}$ (density of states of p -symmetry) due to the dipole selection rule (the effect of transition matrix) [8]. E' is an energy measured from the bottom of V.B. An energy dependence of transition matrix elements, E^{-2} (E : photon energy), can be now omitted because an interested energy region is limited [8]. Experimental intensity distributions seem like those ways, indicating that the free electron model is appropriate for those metals.

Since Li has one valence electron per atom, the Fermi surface of a free electron model does not touch to Brillouin zone boundary. Thus, the intensity profile is expected to be simple as $I_{Li-K}(E') \propto E'^{3/2}$. However, it is clearly seen that the intensity just below E_F is apparently suppressed, indicated by an arrow, apart from $E'^{3/2}$. This discrepancy in Li-K emission has been explained by the effect of 1s core-hole, which exists

before an electronic transition from V.B. [9,10].

In case of Mg, which has two valence electrons per atom, the Fermi surface of a free electron model has some interaction with Brillouin zone boundary. The peak, observed just below E_F , indicated by an arrow, can be explained by the band-structure effect [11] and also the previous core-hole effect, which works to increase the intensity in case for L-emission [10].

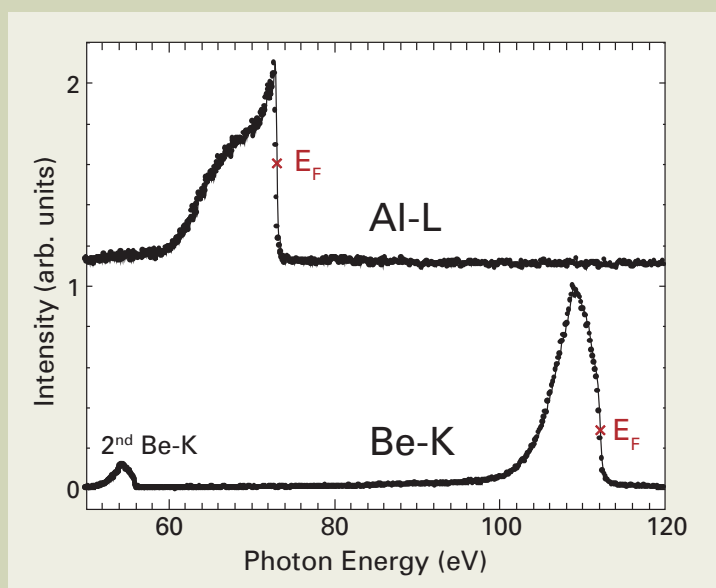
Al-L and Be-K emission spectra

Figure 4 shows an Al-L emission spectrum (V.B.→L-shell) of Al and a Be-K emission spectrum (V.B.→K-shell) of Be. AOs for Al-L and Be-K were 560 nA·min and 390 nA·min, respectively. In the Be-K emission spectra, a secondary diffracted intensity by the grating is also seen at a half of the energy of 1st order diffracted intensity at around 110 eV. Each spectrum shows a clear Fermi edge at the right-hand side end of each intensity distribution. A Fermi energy position, marked by x at the middle of each Fermi edge, corresponds to the top of the occupied energy level of each metal. The energy resolution at E_F of the Al-L emission spectrum was evaluated to be 0.2 eV.

Aluminum has three valence electrons per atom. Then, the Fermi sphere of a free electron model extends to higher Brillouin zones. Thus, intensity distribution is obeyed to $I(E') \propto E'^{1/2}$ in the lower part of V.B. as in the case of Mg-L emission and is affected by the band-structure in the upper part of V.B. The intense peak just below E_F has been explained by a presence of d -symmetry component [8].

Beryllium has two valence electrons per atom. Then, it can be expected a band-structure effect due to a larger free electron Fermi sphere than that of Li-metal. Thus, intensity distribution is obeyed to $I(E') \propto E'^{3/2}$ in the lower part of V.B. as in the case of Li-K emission and is strongly affected by the band-structure in the upper part of V.B. The delayed peak structure is well similar to a calculated density of states [12].

Fig. 4 Al-L emission spectrum (V.B.→L-shell) and Be-K emission spectrum (V.B.→K-shell). Each spectrum shows a clear Fermi edge. E_F position, marked by x at the middle of each Fermi edge, corresponds to the top of the occupied energy level of each metal. The energy resolution at E_F of the Al-L emission spectrum was evaluated to be 0.2 eV. Different characteristics in intensity profiles below E_F can be understood by the band-structure.



Si-L emission spectra

Figure 5 shows Si-L emission spectra (V.B.→L-shell) of Si and TiSi₂. AQs for Si and TiSi₂ were 150 nA·min and 300 nA·min, respectively. Due to the dipole selection rule, intensity distributions correspond to *s+d*-symmetry of the V.B. Since Si crystal is a semiconductor formed by covalent bonding of *sp*³ orbitals, intensity distribution of Si should correspond to *s*-symmetry part of V.B. It is seen that *s*-symmetry component contributes largely in the lower part and smaller in the upper part of V.B. Inversely, *p*-symmetry component possesses dominant part in the upper part and lesser in the lower part of V.B. [8]. The spectrum shows four structures as indicated by vertical lines. Those are assigned to special points of L₂, L₁, X₄ and L₃ in the band diagram [13].

TiSi₂ has been an interested conducting material in large-scale integrated circuit technology and a field-emission property of nanowires. Recently, Si/TiSi₂ heteronanostructures are attracting interest as a memory device [14] and an electrode material for energy storage [15]. Width of V.B. of TiSi₂ is almost the same with that of Si. The intense two peak structures, L₂ and L₁ in the lower part of V.B. of Si, may correspond to closely placed two peaks in TiSi₂. It is noted that the relative intensity in the upper part of V.B. (indicated by an arrow) is increased in TiSi₂ compared to that of Si. In a simple understanding for this change from Si seems a redistribution of *s*-symmetry component in V.B. of TiSi₂. However, this intensity increase is reported to be a contribution of *d*-symmetry of Si, which interacts with 3*d* orbitals of Ti, based on a theoretical calculation [16].

It is seen that energy positions of top of the V.B., indicated by a vertical broken line, is almost the same for both materials within experimental accuracy. The relative energy shift of TiSi₂ compared to Si can be evaluated by $\Delta E_B - E_g/2$ [8], where ΔE_B is a chemical shift value of Si-L level in TiSi₂ and E_g is an energy gap of 1.2 eV for Si. ΔE_B is reported to be about 0.5 eV [17]. Then, $\Delta E_B - E_g/2$ is calculated to be -0.1 eV, which is consistent with

present experimental results within the accuracy. A steep intensity increase at the top of V.B. in TiSi₂ should be attributed to a presence of the Fermi edge.

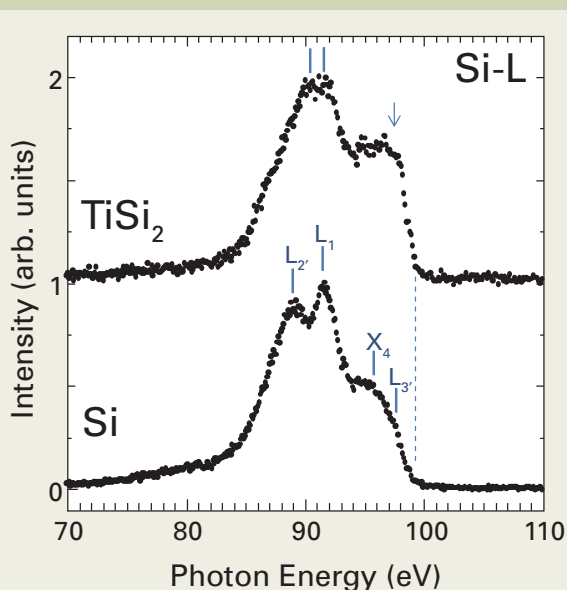
B-K emission spectra

Figure 6 shows B-K emission spectra (V.B.→K-shell) of CaB₆ (semiconductor) and LaB₆ (metal, well known cathode material). These intensity profiles have better signal to noise ratios compared to those to previous spectra. It is mainly due to a large AQ of 1560 nA·min for both spectra. Both materials belong to the same crystal structure of metal hexaborides MB₆. A schematic figure of the structure is shown as an inset. Due to the dipole selection rule, K-emission intensity corresponds to *p*-symmetry component in the V.B. Since boron atom has 2*s* and 2*p* valence electrons, intensity distribution of B-K emission should have larger intensity for the upper part of V.B. This situation is opposite compared to that in L-emission stated above.

The main peak in each spectrum is due to B-B bonding states between B atoms of B₆ cluster (intra-cluster orbitals), which are located at each corner of a cubic unit cell of the inset figure. The energy positions of the shoulder structures, indicated by vertical lines, are apparently different for the two materials. It may be due to a different B-B bonding length inside the cluster of the two materials [18]. The lower part of V.B. is assigned to inter-cluster bonding states labeled as B₆-B₆. CaB₆ shows a longer tail of B₆-B₆ intensity, which may be due to shorter inter-cluster distances causing larger energy dispersion for inter-cluster bonding states.

The most dominant difference between the two spectra is seen in the top part of the V.B. La and Ca atoms can transfer three and two electrons, respectively, to B₆-cluster network. Thus, higher energy levels should be occupied by electrons in LaB₆ than those in CaB₆. The spectrum of LaB₆ clearly shows an additional intensity at the right-hand side of the dominant B-B peak (top of V.B.) compared to that of CaB₆. It should be noted that a clear Fermi edge is seen corresponding

Fig. 5 Si-L emission spectra (V.B.→L-shell) of TiSi₂ and bulk silicon. Due to the dipole selection rule, intensity distributions correspond to *s+d*-symmetry of V.B. Intensity distribution shows that the *s*-symmetry is dominant in the lower part of V.B. Four structures labeled as L₂, L₁, X₄ and L₃ on the spectrum of Si correspond to special points in the band diagram.



to a metal nature of this material. The energy resolution at E_F was evaluated to be 0.4 eV. The Fermi level exists in a hybridized band of B-2p and La-5d orbitals [19].

Conclusion

A newly designed soft-X-ray spectrometer attached to a conventional transmission electron microscope has extended the detection lower limit from 60 eV to 50 eV by using a new VLS grating of JS50XL. This spectrometer enables us to detect Li-K emission from an identified specimen area by electron microscopy. Not only characteristic intensity distributions of K- and L-emissions of simple metals but also a core-hole effect in Li-K emission were observed. Structures in L-emission of Si were assigned to special points in the band diagram. The Fermi level in a cathode material of LaB_6 has been clearly observed. Thus, it is successfully shown that this SXES instrument provides a new valence electron spectroscopy method for chemical analyses not only for a wide variety of new functional materials developments but also for basic research of compounds.

Acknowledgments

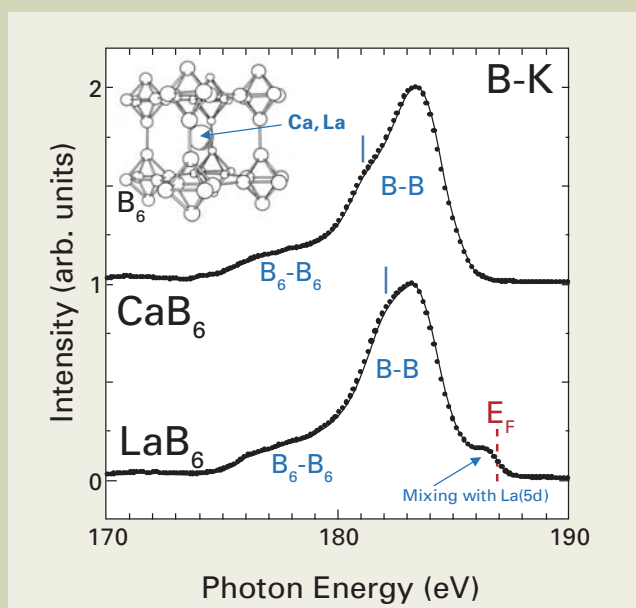
The authors thank Mr. F. Sato for his skillful technical assistance. This development was conducted as one project of Collaborative Development of Innovative Seeds (Practicability verification stage) by Japan Science and Technology Agency. Measurements of Li-K emission were partly supported by a Grant-in-Aid for Scientific Research on Priority Areas 'New Materials Science Using Regulated Nano Spaces-Strategy in Ubiquitous Elements' by the Ministry of Education, Culture, Sports, Science and Technology of Japan (No.19051002).

References

[1] Y. Sato, M. Terauchi, M. Mukai, T. Kaneyama and K. Adachi, *Ultramicroscopy*, **111**, 1381 (2011).

- [2] Y. Sato, M. Terauchi, W. Inami and A. Yoshiasa, *Diamond and Related Materials*, **25**, 40 (2012).
- [3] M. Terauchi and M. Kawana, *Ultramicroscopy*, **106**, 1069 (2006).
- [4] M. Terauchi, M. Koike, K. Fukushima and A. Kimura, *Journal of Electron Microscopy*, **59**, 251 (2010).
- [5] M. Terauchi, *Microscopy Research and Technique*, **69**, 531 (2006).
- [6] M. Terauchi, H. Takahashi, N. Handa, T. Murano, M. Koike, T. Kawachi, T. Imazono, M. Koeda, T. Nagano, H. Sasai, Y. Oue, Z. Yonezawa and S. Kuramoto, *Journal of Electron Microscopy*, **61**, 1 (2012).
- [7] H. Takakashi, N. Handa, T. Murano, M. Terauchi, M. Koike, T. Kawachi, T. Imazono, M. Koeda, T. Nagano, H. Sasai, Y. Oue, Z. Yonezawa and S. Kuramoto, *Microscopy & Microanalysis*, **16(supple.2)**, 34 (2010).
- [8] D.J. Fabian, L.M. Watson and C.A.W. Marshall, *Rep. Prog. Phys.*, **34**, 601 (1972).
- [9] F.K. Allotey, *Phys. Rev.*, **157**, 467 (1967).
- [10] Y. Mizuno and K. Ishikawa, *J. Phys. Soc. Japan*, **25**, 627 (1968).
- [11] R.P. Gupta and A.J. Freeman, *Phys. Rev. Lett.*, **36**, 1194 (1976).
- [12] S.T. Inoue and J. Yamashita, *J. Phys. Soc. Japan*, **35**, 677 (1973).
- [13] S. Shin, A. Agui, M. Watanabe, M. Fujisawa, Y. Tezuka and T. Ishii, *Phys. Rev. B*, **53**, 15660 (1996).
- [14] Y. Zhu, B. Li and J. Liu, *J. Appl. Phys.*, **101**, 063702 (2007).
- [15] S. Zhou, X. Liu and D. Wang, *Nano Lett.*, **10**, 860 (2010).
- [16] P.J.W. Weijs, H. van Leuken, R.A. de Groot and J.C. Fuggle, *Phys. Rev. B*, **44**, 8195 (1991).
- [17] Y. Yamauchi, M. Yoshitake and SERD project group of SASJ, *J. Surface Analysis*, **9**, 432 (2002).
- [18] "The chemistry of Boron and its Compounds", ed. by E.L. Muetterties, John Wiley & Sons, Inc., New York (1967), p.119.
- [19] S. Kimura, H. Harima, T. Nanba, S. Kunii and T. Kasuya, *J. Phys. Soc. Japan*, **60**, 745 (1991).

Fig. 6 B-K emission spectra of CaB_6 and LaB_6 . Due to the dipole selection rule, intensity distributions correspond to p -symmetry of V.B. Intensity distribution shows that the p -symmetry is dominant in the upper part of V.B. The most dominant difference between the two spectra is seen in the top part of V.B. The spectrum of LaB_6 clearly shows a Fermi edge corresponding to a metal nature of the material. The energy resolution at E_F was evaluated to be 0.4 eV.



Electron Microscopic Study and X-ray Probe Microanalysis of the Liver of LEC Rat, an Animal Model of Wilson Disease

Hisao Hayashi[†], Yoshikazu Fujita^{††}, Miho Furukawa[†], and Akiko Suzuki[†]

[†] Department of Medicine, Aichi Gakuin University School of Pharmacy

^{††} Medical Research Engineering, Nagoya University Graduate School of Medicine

Microanalysis using JEOL JEM-2010 and JEM-2800 could provide important information on trace elements in LEC rat livers. Copper appeared with sulfur, while iron coexisted with phosphorus and oxygen in acid phosphatase-positive dense bodies. It is likely that cuprothionein and iron protein are stored in the lysosomal system of hepatocytes and Kupffer cells. Therefore, LEC rats may be a good model for studying the pathogenesis of progressive liver disease in Wilson disease.

Introduction

Morphological identification of lysosomes was established by acid phosphatase reaction [1]. Pericanalicular lysosomes exhibited lead deposits after incubating liver slices with a lead and phosphate solution under acidic condition. Transitional elements, copper and iron, are stored in lysosomes as detoxified forms of cuprothioneins and hemosiderins, respectively. Genetic background of adult-onset storage diseases in the liver remained undetermined until 1993 when ATP7B was cloned in patients with Wilson disease (WD) [2]. In 1996, HFE was first cloned in patients with hemochromatosis, followed by TFR2 of non-HFE hemochromatosis. These storage diseases of the liver were named secondary lysosomal diseases due to genetic defects of extra-lysosomal molecules [3].

Light microscopy is a standard laboratory examination of the modern pathology, but has a drawback in detecting heavy metal toxicoses. Special staining methods such as rhodanine and rubeanic acid for copper, and Berlin blue for iron are needed. It must be kept in mind that negative results do not rule out overloading, namely toxic effect of transition metals. Aggregation of metal-rich lysosomes may be needed in positive histochemical staining, or minimal overloading of metal in lysosomes may be toxic [4].

Electron Microscopy is widely used in clinical diagnosis and pathological investigation. Structural changes of intracellular organelles provided by electron microscopy are important information for understanding disease mechanism of patients and animal models. In addition, X-ray microanalysis, especially energy dispersive X-ray microanalysis (EDX), realizes detection of not only trace element deposits but also compositional pattern of heavy metal complexes [5].

The liver is a central organ for homeostasis of trace elements of iron and copper. Iron absorption in the gut is regulated by hepcidin molecules secreted from the liver, while excess copper is secreted from the liver into bile. The hepatic copper transporter ATP7B is defective in patients with WD whose biliary excretion of copper was completely blocked [6, 7]. Excess copper is first stored in the liver, and then in extrahepatic organs including the central nervous system. In the liver, copper is stored in hepatocellular lysosomes as cuprothioneins. Recent studies indicate that lysosomes are also loaded with iron, and may be replaced by iron during long-term copper chelation because of more severe hypoceruloplasminemia [8]. Both iron and copper are transition elements and primary sources in radial generation. As a result, multi-organ damage may be inevitable when excess amounts of iron and copper are accumulated in the liver and other organs.

Long-Evans cinnamon (LEC) rats are an animal model of WD with an ATP7B mutation and hypoceruloplasminemia [9]. There is evidence to suggest that transition metals of both iron and copper may be involved in variety of fulminant hepatitis and chronic hepatitis of LEC rats [10, 11]. Because these transition elements are finally stored in hepatocellular lysosomes as detoxified forms, ultrastructural element analysis on LEC rats may provide information of cytoprotective response to hepatotoxic elements during chronic hepatitis leading to hepatic fibrosis and malignancy in ATP7B-linked copper toxicosis.

Materials and Methods

Two male LEC rats aged 16 weeks were purchased from Chubu Kagaku Shizai Inc. (Nagoya). Hepatectomy was performed under anesthesia. As a standard study using transmission electron microscopy, pieces of liver specimens (1 mm³) were fixed with 2% glutaraldehyde in 0.1 M cacodylate buffer for 3 days, and post-fixed with 0.1% osmic acid solution buffered with 0.1 M cacodylate buffer, pH 7.2, for 45 min [12]. To identify lysosomes under

Fig. 1 Microanalysis of LEC rat hepatocytes. Transmission electron micrograph shows a variety of intracellular dense bodies (upper). There are 2 subtypes, Cu-rich dense bodies and Fe-rich ones identified by X-ray microanalysis (lower). Note that Fe-rich dense bodies are heterogeneous in matrices with fine grains. Fixed with 0.1% osmic acid and stained with uranyl acetate. (taken with a JEM-2010)

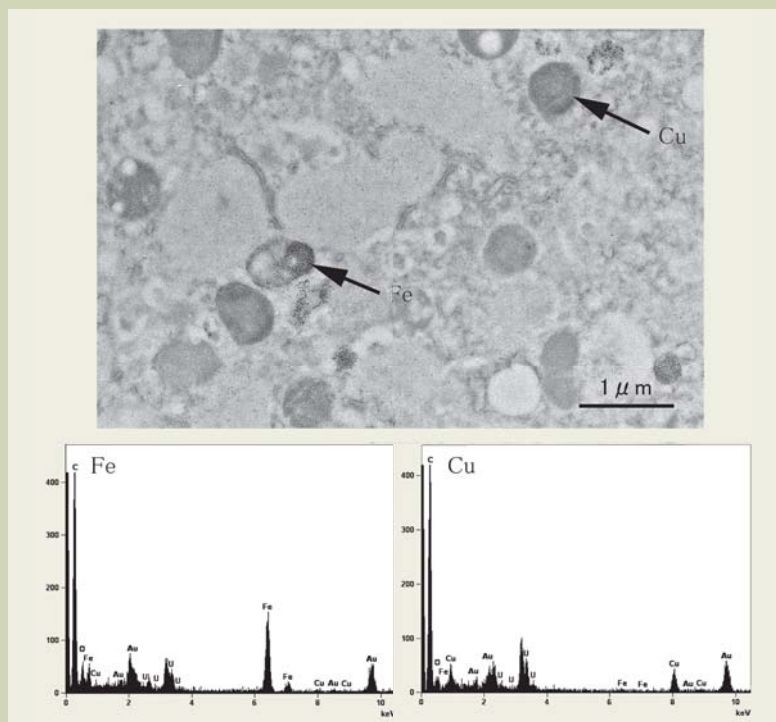
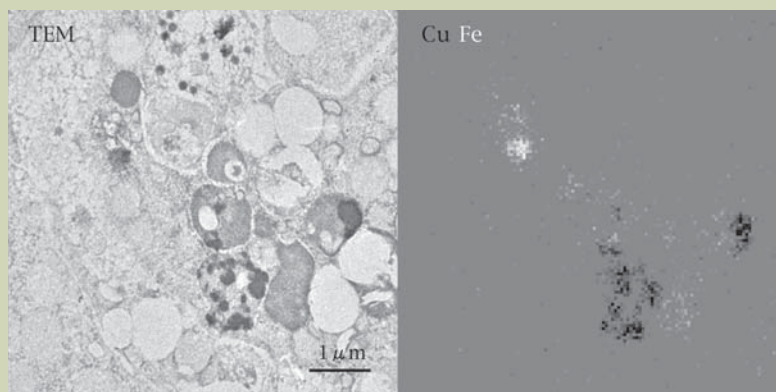


Fig. 2 Microanalysis of LEC rat Kupffer cells using a JEM-2010. Transmission micrograph shows a variety of intracellular dense bodies (left). Two dimensional imaging shows different distribution of Cu and Fe in dense bodies and their matrices (right). Fixed with 0.1% osmic acid and unstained.



electron microscopy, portions of liver tissues were fixed in 4% paraformaldehyde at 4°C, and 0.1 M cacodylate buffer, pH 7.2, for 60 minutes. After rinsing in 0.1 M cacodylate buffer at 4°C, pH 7.2, with 0.25 M sucrose, specimens were sliced in agar gel. Sections were incubated in 0.05 M acetate buffer, pH 5.0, with lead nitrate, sucrose, and 3% β-glycerophosphate, pH 5.0-5.2, at 37°C for 10 minutes, followed by a short rinsing period in distilled water [13]. Liver pieces were finally embedded in epoxy resin, TAAB812. Ultra-thin sections were mounted on gold grids. Sections unstained and stained with a 2% uranyl solution were examined under a transmission electron microscope (TEM; JEOL) and other JEOL microscopes (JEM-2010, JEM-2800) equipped with an EDX.

Electron microscopic study was first performed to visualize intracellular distribution of dense bodies in hepatocytes, Kupffer cells, and bile duct epithelial cells. Using an EDX of a JEM-2010, dense bodies in the hepatocytes, Kupffer cells, and bile duct epithelial cells were randomly exposed to electron beams for a short period. Lead was always identified in the dense bodies with acid phosphatase reaction. When copper or iron was identified in a particular dense body, the total number of X-rays yielded from the dense body was counted for 200 sec to complete an X-ray spectrum. Identification of

the specific Kα X-rays of copper and iron was performed using an autoanalysis system equipped with the EDX. Co-existence of copper and iron was expressed as isolated Cu, compound Cu and Fe, and isolated Fe. Finally, the 2 dimensional distribution of iron or copper with other elements were mapped using scans of the dense body-rich cytoplasm with the EDX of a JEM-2800 for 480 sec. Multi-element X-ray spectrums at any pin point area were available after 2 dimensional scanning.

Results

Under electron microscopy, hepatocellular organelles including the nucleus, mitochondria, and dense bodies were visualized in ultrathin sections (**Fig. 1**). Combined with EDX, some characters of Cu- and Fe-positive dense bodies of hepatocytes were visualized. Cu-rich particles were diffusely dense, while Fe-rich particles were granularly dense. Kupffer cells contained a variety of dense bodies. Distribution of Cu and Fe was apparently different in these dense bodies (**Fig. 2**). After the acid phosphatase reaction, hepatocellular dense bodies became positive for lead precipitation. As a result, co-deposits of intrinsic elements of copper and iron, and extrinsic lead were identified in some hepatocyte dense bodies (**Fig. 3**). There was no significant

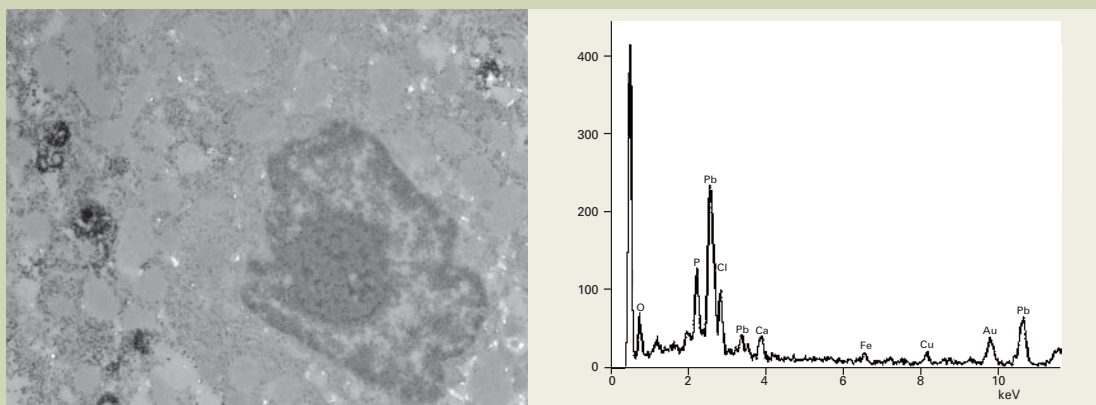


Fig. 3 Microanalysis of LEC rat hepatocytes with acid phosphatase reaction. Transmission electron micrograph shows intracellular dense bodies scattered in the cytoplasm (left). Extrinsic elements of Pb and Au, and intrinsic elements of O, P, Ca, Fe, and Cu appear in the spectrum obtained from a dense body. Fixed with a 4 % paraformaldehyde solution, and incubated with a Gomori-medium for acid phosphatase reaction, and observed without staining. (taken with a JEM-2010)

lead precipitation outside of the dense bodies.

Two dimensional distribution of copper and iron was clearly visualized within lysosomes (**Fig. 4**). Iron was co-existed with phosphorus and oxygen, while copper appeared with sulfur. Intralysosomal localization of copper and iron seemed different.

Discussions

Wilson disease is primary copper toxicosis due to mutant ATP7B which can not transport Cu molecules inside the Golgi net work. As a result, copper accumulates in the cytoplasm secondary to impaired secretion of copper into bile. However, recent studies indicate the co-existence of copper and iron in patients with WD, especially in male patients after copper chelation therapy [8]. Similar observations with WD patients were obtained in the current study using the LEC rats, animal model of WD. Iron complex consists of phosphorus and oxygen, while copper makes complex with sulfur. Dense bodies either in hepatocytes or Kupffer cells were positive for acid phosphatase, supporting that both copper and iron are accumulated in lysosomes of parenchymal cells and reticuloendothelial cells, as cuprothionein and hemosiderin, respectively. The etiology of iron overload in the animal model of WD may be complex as human disease [14], but the main reason may be due to hypoceruloplasminemia. In the animal model, dietary iron may be fortified for higher fertility. LEC rats are representative of primary copper toxicosis and secondary iron overloading due to ferroxidase deficiency and dietary fortification.

In spite of primary copper toxicosis, liver specimens of young LEC rats around 16 weeks of age are not positive for histochemical copper staining such as rhodanine and rubeanic acid. Aggregation of copper-positive lysosomes around bile canaliculi is prerequisite for histochemical staining so that biochemical determination of hepatic copper is widely applied in most reports of LEC rat studies. In fact, not histochemical study but chemical determination of copper is recommended in international scoring system for diagnosis of WD [15]. Microanalysis used in this study is not routine examination in practice, but all X-rays appear in a spectrum, clarifying multi-metal accumulation within lysosomes.

Energy dispersive X-ray microanalysis opened a way to study in vivo interaction of multi-elements. Using the JEM-

2800, both information on intralysosomal distribution and coexistence with other elements was simultaneously obtained from LEC rat liver. Different pattern of copper deposits was obtained in hepatocytes and Kupffer cells, as well. Although the sensitivity of element detection is not different, but the time period consumed for one analysis is quite different between the JEM-2010 and the JEM-2800 (8 hrs vs. 8 min/one imaging). Information on X-rays accumulated in a 2 dimensional analysis is also different. X-rays yielded from any spot area within the imaged field are reserved in a computer, and are reproducible after analysis.

Twenty years ago, using an EDX, we met a question of coexisting copper and iron in a male patient with WD. Now, we understand that iron also accumulates in the liver of WD due to concomitant low levels of serum ceruloplasmin, namely ferroxidase deficiency [8]. This hypothesis was supported by double overloading of copper and iron in animal model of LEC rats [9] and discovery of aceruloplasminemia by Miyajima [16]. The genetic disease was not a copper disease but one of iron overload syndromes.

Lysosomal deposits of iron complexes and cuprothioneins do not mean pathological conditions, but detoxification process by cellular defense mechanism. It is more important to detect toxic metal ions around the organelles essential to survive and resume the ability of reproduction. In the case of copper with a physiologically secretory route of bile ducts, copper retention is inevitable in WD and idiopathic copper toxicosis, but unusual in secondary pathological conditions. These include primary biliary cirrhosis and non-alcoholic steatohepatitis. Copper toxicosis in these conditions may be overcome with UDCA treatment [17].

In the case of iron which has no physiological route for excretion, iron overload may occur in a variety of pathological conditions. A small amount of lysosomal iron in CHC indicates iron-induced oxidative stress to hepatocytes infected with HCV. Complete removal of lysosomal iron is an effective treatment of refractory liver disease [18]. However, a large amount in lysosomal iron in hepatocytes does not affect hepatocytes of aceruloplasminemia [16]. Liver structures are intact even in aged patients. Low levels of serum iron and transferrin saturation indicates hepatocytes usually face with iron deficient state, probably except for a short postprandial period when iron is actively absorbed by inappropriately low setting of hepcidin regulation system. Iron, once trapped in lysosomes, can not utilize outside of lysosomes

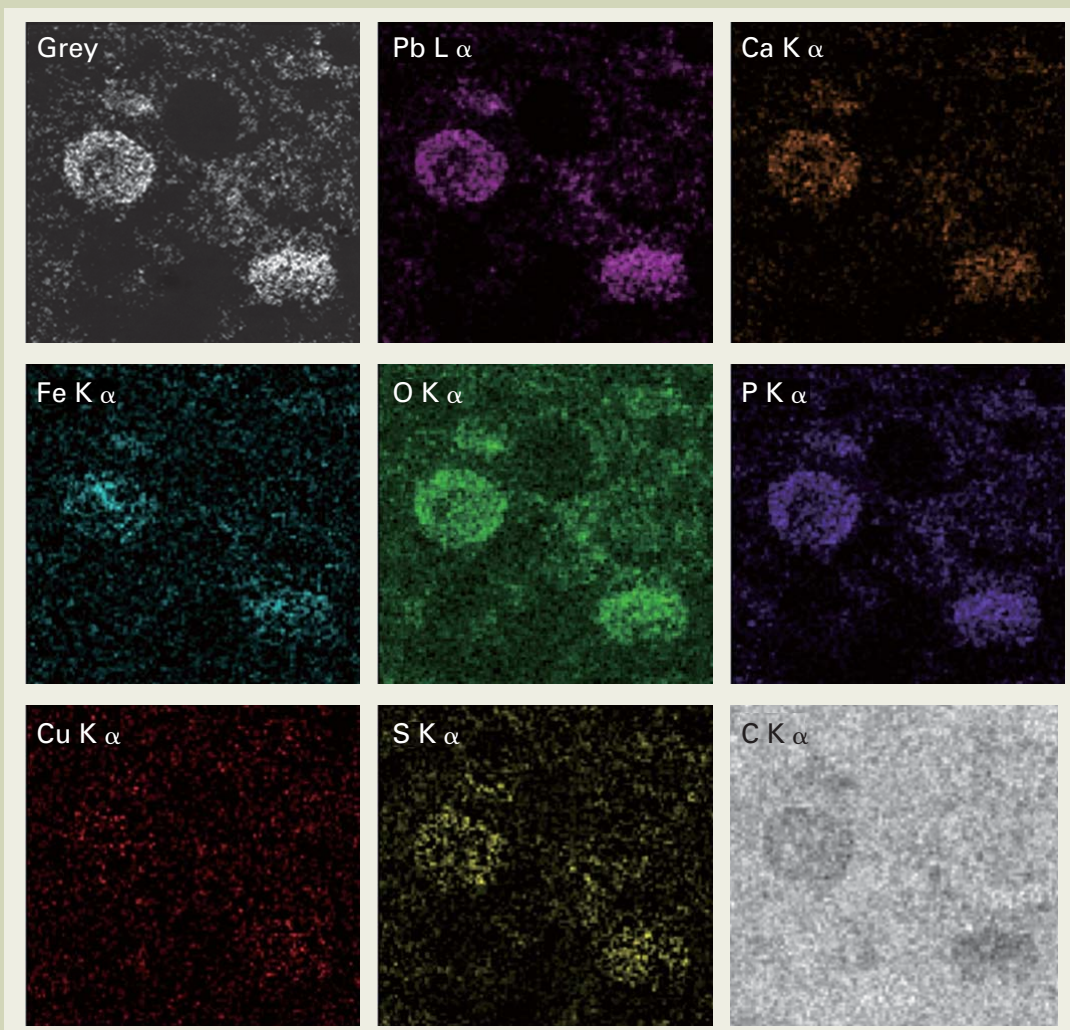


Fig. 4 Microanalysis of LEC rat hepatocytes using a JEM-2800. A series of 2 dimensional imaging using specific X-rays visualize intrinsic elements of Ca, Fe, O, P, Cu, S, and C. Pb is a reaction product demonstrating these particles lysosomal in origin. Note diffuse distribution of Cu in the cytoplasm.

probably because transport across membrane is disrupted in aceruloplasminemia. This may be a reason why patients with aceruloplasminemia are not affected by iron-induced liver damage in spite of heavy iron deposits in the liver.

Conclusions

Compound overloading of copper and iron was confirmed in lysosomes of LEC rat livers. Copper appeared with sulfur, while iron coexisted with phosphorus and oxygen. Microanalysis using JEOL JEM-2010 and JEM-2800 could provide important information on the state of trace elements in LEC rats, which may be a good model for studying the pathogenesis of progressive liver disease in WD.

References

- [1] Novikoff A. B., Beaufay H., and De Duve C., *J Biophysic Biochem Cytol*, **2**, suppl 179 (1956).
- [2] Yamaguchi Y., Heiny M. E., and Gitlin J.D., *Biochem Biophys Res Commun*, **197**, 271-277 (1993).
- [3] Hayashi H., Wakusawa S., Yano M., et al., *Hepatol Res*, **37**, 777-783 (2007).
- [4] Hayashi H., Fujita Y., Tatsumi Y., et al., *Hepatol Res*, **39**, 563-568 (2009).
- [5] Hanaichi T., Kidokoro R., Hayashi H., and Sakamoto N., *Lab Invest*, **51**, 592-597 (1984).
- [6] Gitlin J. D., *Gastroenterology*, **125**, 1868-1877 (2003).
- [7] Roberts E. A., and Schilsky M. L., *Hepatology*, **37**, 1475-1492 (2003).
- [8] Shiono Y., Wakusawa S., Hayashi H., et al., *Am J Gastroenterol*, **96**, 3147-51 (2001).
- [9] Mori M., Hattori A., Sawaki M., et al., *Am J Pathol*, **144**, 200-204 (1994).
- [10] Togashi Y., Li Y., Kang J., Takeichi N., et al., *Hepatology*, **15**, 82-87 (1992).
- [11] Kato J., Kobune M., Kohgo Y., et al., *J Clin Invest*, **98**, 923-929 (1996).
- [12] Motonishi S., Hayashi H., Fujita Y., et al., *Ultrastruct Pathol*, **30**, 409-414 (2006).
- [13] Hayashi H., and Sternlieb I., *Lab Invest*, **33**, 1-7 (1975).
- [14] Walshe J. M., and Cox D.W., *Lancet*, **352**, 1504 (1998).
- [15] Ferenci P., Caca K., Loudianos G., et al., *Liver Int*, **23**, 139-142 (2003).
- [16] Miyajima H., Nishimura Y., Mizoguchi K., et al., *Neurology*, **37**, 761-767 (1987).
- [17] Poupon R., Chretien Y., Poupon R.E., et al., *Lancet*, **2**, 834-836 (1987).
- [18] Hayashi H., Takikawa T., Nishimura N., et al., *Am J Gastroenterol*, **89**, 986-8 (1994).

Electron Microprobe Study of Otolith: Migratory Behavior and Habitat of Three Major Temperate Species of Eels

Yoshiyuki Iizuka

Institute of Earth Sciences, Academia Sinica

An analytical technique for measurement of strontium (Sr) and calcium (Ca) concentrations in otolith was developed using an electron probe micro-analyzer (EPMA). Precisions of measurement for Sr and Ca were examined with various electron beam conditions, which were a combination of different beam currents, beam diameter, X-ray counting time, and diffracting crystals on carbonate standards and eel otolith. The precision decreased when beam power densities exceeded $1 \mu\text{W}/\mu\text{m}^2$ and/or beam diameter was less than $2 \mu\text{m}$, resulting from beam damage of carbonates. The optimum analytical conditions for measuring the Sr/Ca ratios in the otoliths are suggested to be with a beam current at 3 nA, a $5 \times 4 \mu\text{m}^2$ beam, counting times of Sr and Ca for 80 sec and 20 sec at the peak, and of Sr and Ca for 20 sec and 10 sec at back-ground intensities at an acceleration voltage of 15 kV with strontianite and aragonite standards, respectively. In these conditions, it is possible to obtain precise measurements of Sr/Ca ratios at $10 \mu\text{m}$ intervals along a transect from the primordium (core) to the edge of individual otolith with an error less than 0.05 wt% in Sr, as these have been found to discriminate between brackish- and fresh-waters. We have studied more than 1,000 temperate eels from different water bodies where the East Asia (Japanese eels *Anguilla japonica*), the Northeast America (American eels *Anguilla rostrata*), and the Northwest Europe (European Eel *Anguilla anguilla*). Patterns of otolith Sr/Ca ratios from core to edge indicated similar but multiple life histories, at least four to six type of migration behaviors. Additionally, the Sr/Ca patterns of otoliths clearly illustrate eels' life between naturally-recruited and artificially-restocked. Since Anguillid eels are the endangered species, the revealed habitat information from otolith microchemistry are variable and useful for conservation and cultivate studies.

Introduction

Otolith (ear-stone) of fish is an organ in the inner ear, which is composed of 3 types of otolith; sagitta, asteriscus, and lapillus, and functions for body balance and hearing. The otolith consists of approximately 95-6 wt% of calcium carbonate (CaCO_3), 3-4 wt% of organic matters, and less than 1 wt% of trace elements. The metabolically inert nature of the otolith assures that all mineralogical deposition remains unchanged throughout the life history of the fish [1]. Sagittal otolith is biomineralized aragonite which is deposited daily on a proteinaceous matrix [2, 3]. Aragonite has relatively higher substitution rate of the alkali earth elements, particularly Strontium (Sr), into the Ca site than the polymorphism calcite. In the seawater, Sr concentrations are approximately 100 fold higher than in freshwater environments. It is thought to be, therefore, that Sr can substitute for Ca in the process of otolith deposition during the seawater and brackish water residence [4]. Accordingly, temporal changes of the elements in sagittal otoliths can reflect the environment that a fish experienced. Ratios of Sr/Ca in otoliths were positively correlated to those in the ambient water

[5]. Consequently, Sr/Ca ratios are extensively used to study the movement of diadromous fishes [e.g., 6-14]

Electron probe micro-analyzers (EPMA) equipped with wavelength dispersive X-ray spectrometers (WDS) have been widely used to determine chemical compositions of rock-forming minerals. The EPMA can analyze the calcium carbonate otolith at a limited area under observation of scanning electron micrograph. This is an advantage to target of analyses points on the otolith. It is well known, however, that carbonates are susceptible to damage from the electron beam. To avoid beam damage problem, consideration of electron beam setting and exposure time are essential in the development of high-precision analyses of otolith microchemistry [15-17].

The Sr/Ca ratios in otolith have been widely used for study of migratory history of fish since the late 1980s. Electron beam conditions and exposure times used for the quantitative analysis of Sr in otolith have greatly varied among laboratories. Gunn et al. [15] and Toole & Nielsen [17] indicated that the quantitative analysis of Sr in otoliths should be concern because of its low concentration. These researchers attempted to establish a criterion to analyze the Sr in otoliths by balancing the beam condition, in terms of beam power density (BPD)*, and beam exposure time to increase precision of the analyses of Ca and Sr. Gunn et

No.128, Sec. 2 Academia Road, Nankang Taipei, Taiwan 115, ROC

yiizuka@earth.sinica.edu.tw

al. [15] indicated that high BPD and long beam exposure time might cause pitting and induce a chemical change on the otolith. And then the BPD less than $3 \mu\text{W}/\mu\text{m}^2$, which is maintained beam current at 25 nano ampere (nA) and beam diameter at $20 \mu\text{m}$ with an acceleration voltage of 15 kilo volt (kV), was recommended. The relative error of Sr contents in otoliths can be decreased by increasing the beam exposure time and lowering BPD. On the other hand, Toole & Nielsen [17] concluded that to increase analytical precision without losing accuracy, the BPD should be adjusted to approximately $15 \mu\text{W}/\mu\text{m}^2$, i.e., maintaining beam current at 25 nA and beam diameter at $5 \mu\text{m}$ with an acceleration voltage of 15 kV. They also suggested that the behaviors of Sr and Ca are similar during beam damage, regardless of Ca concentration. However, this is not the case in the analysis of, at least, eel otoliths under their recommended conditions. By increasing beam exposure time, the intensity of Ca will increase and carbon (C) intensity will decrease (see below for further details). This may be due to a loss of material from the beam strike. Beam damage effects on the otolith surface and on target elements of the carbonates should be considered; otherwise it is difficult to evaluate small variations of Sr concentration (<1 wt%) in otoliths. In this paper, the author reports an examination of optimum technique of otolith study by EPMA and results of application studies of migratory history of eels.

Experimental procedure:

(1) Equipment

Elemental concentrations were quantified using an electron probe micro-analyzer (JEOL, JXA-8900R) at the Institute of Earth Sciences, Academia Sinica, Taipei, Taiwan. It is equipped with 4-channel WDS and programmed both qualitative (X-ray peak search, intensity counting and mapping) and quantitative (concentration) analyses. The quantitative data were corrected as oxides with standard calibration by the Phi-rho-z (PR-ZAF)

* Beam Power Density ($\mu\text{W}/\mu\text{m}^2$)= $[E_0 \times I]/A$, where E_0 is the acceleration voltage, I is the beam current and A is the area of electron beam on the surface of specimen.

method, which is a matrix correction with factors of atomic number (Z), absorption (A) and fluorescence (F) and depth distribution function (ρx), which represents the X-ray intensity per unit mass depth (ρz) [18, 19].

(2) X-ray Diffracting crystals

For Ca $K\alpha$ measurement, the X-ray diffracting crystal Pentaerythritol (PETJ) was used. Two kind of diffracting crystals, PETH and Thallium Acid Phthalate (TAP) were used for measurement of Sr $L\alpha$. The diffracting crystals Lead Stearate (STE) was used for the measurement of C $K\alpha$. Each crystal is separately equipped in 3-different WDS channel of EPMA.

(3) Accelerating voltage

Acceleration voltage of 10-25 kV is generally used for rock-forming minerals. X-ray intensity from sample increases with accelerating voltage of the electron beam. However, the electron beam at higher voltage reaches deeper part of sample specimen and leads to decomposition of the specimen [20], and subsequently, X-ray intensity may alter during the analysis. Thus higher voltage (>20 kV) is typically applied to materials, which are damage-resistant to the electron beam, such as metal and metallic alloy. Lower voltage (<10 kV), on the other hand, is advantageous for light elements, though it is difficult to measure the X-ray intensity of the L-lines for such elements as Sr [19]. Therefore, the accelerating voltage was selected to be 15 kV, which is similar to some previous studies of otolith.

(4) Beam current

The beam current was tested from 1 to 20 nA. Minimum beam current was selected at 1 nA because a beam current lower than 1 nA was unable to detect the peak intensity of Sr in the otolith. Stabilities of the beam current were less than 0.25 % for 24 hr in all conditions.

(5) Otoliths and standard materials

Sagittal otolith of eel was extracted and mounted in

epoxy resin (EpoFix resin, Struers Co. Ltd) and then was ground and polished by aluminum compounds on polishing papers until the primordium was exposed. The otolith specimen was cleaned with distilled water in an ultrasonic bath and air dried before the carbon coating.

Chemical-known carbonates are selected for standard calibrations because of similar matrix compound to the otolith [21]. Calcite (CaCO_3 in the Trigonal system; NMNH 136321 [22]), a synthetic aragonite (CaCO_3 , which is a polymorph of calcite, in the Orthorhombic system) and strontianite ($[\text{Sr}_{0.95}\text{Ca}_{0.05}]\text{CO}_3$ in Orthorhombic system [aragonite-structure]; NMNH R10065 [23]) were used as standards. The standards were mounted in epoxy resin and polished, then carbon-coated with the same thickness (approx. 25 nm [nano meter]) as the otolith specimens.

Establishment of Optimum beam condition

(1) Surface beam damage on otolith

Figure 1 shows damage spots on a polished otolith surface by various electron beams, BPD ranges from 0.1 to $376.8 \mu\text{W}/\mu\text{m}^2$. The BPD is a combination of the beam current at 1–20 nA and a beam diameter of 1 (focused beam), 5 and 10 μm , and $5 \times 4 \mu\text{m}^2$ rectangle scanning beam, at the acceleration voltage of 15 kV for 100 seconds beam exposure. Surface observation under the secondary electron micrograph shows that higher BPD made stronger damage than lower BPD beam spot.

Relations between the X-ray intensities and beam exposure time were determined for $\text{Ca } K\alpha$, $\text{C } K\alpha$ and $\text{Sr } L\alpha$

of an otolith at the BPD ranging from 0.2 to $7.5 \mu\text{W}/\mu\text{m}^2$, which are combinations of beam current between 3 nA and 10 nA, and beam size of 10 μm , 5 μm , $5 \times 4 \mu\text{m}^2$ ($\times 20,000$ in magnification) and $3 \times 2 \mu\text{m}^2$ ($\times 30,000$). The Ca, Sr and C intensities were counted for 5 sec \times 50 cycles at the same spot after setting each peak position. Total beam exposure time is 250 sec at each analysis spot on the otolith surface.

The intensities of Ca, C and Sr were greater at higher than lower beam currents (**Fig. 2a, b and c**). At higher beam current, the intensities of Ca increased and C decreased with increasing exposure time, and the extent of alteration depended strongly upon the BPD. At a lower beam current, such as 3 nA and lower BPD ($20\text{k}: 5 \times 4 \mu\text{m}^2$ rectangle beam), Ca intensities did not change throughout the analysis for 250 sec (**Fig. 2a-1 and 2a-2**), whereas the intensities of C were severely altered under the higher BPD beam compared with that of a larger beam size regardless of beam current (**Fig. 2b**). Changes in Sr intensities were smaller than those of other two elements regardless of the BPD and the exposure time (**Fig. 2c**). This indicates that the chemical composition of the otolith was changed by the beam strike with the electron current >10 nA or BPD $>3.8 \mu\text{W}/\mu\text{m}^2$, which is a beam of 5 nA and 5 μm in diameter. The otolith surface, as indicated by secondary electron images (**Fig. 1**), was also altered in the BPD is greater than $2 \mu\text{W}/\mu\text{m}^2$, while pitting was reduced or not clearly observed at BPD $<1 \mu\text{W}/\mu\text{m}^2$. These indicate that chemical alteration occurred due to the material loss associated with pitted spots on the surface of otolith during beam exposure. Accordingly, the otolith surface was undoubtedly damaged by high BPD and high beam current. The extent of damage depends upon the magnitude of BPD and beam exposure time.

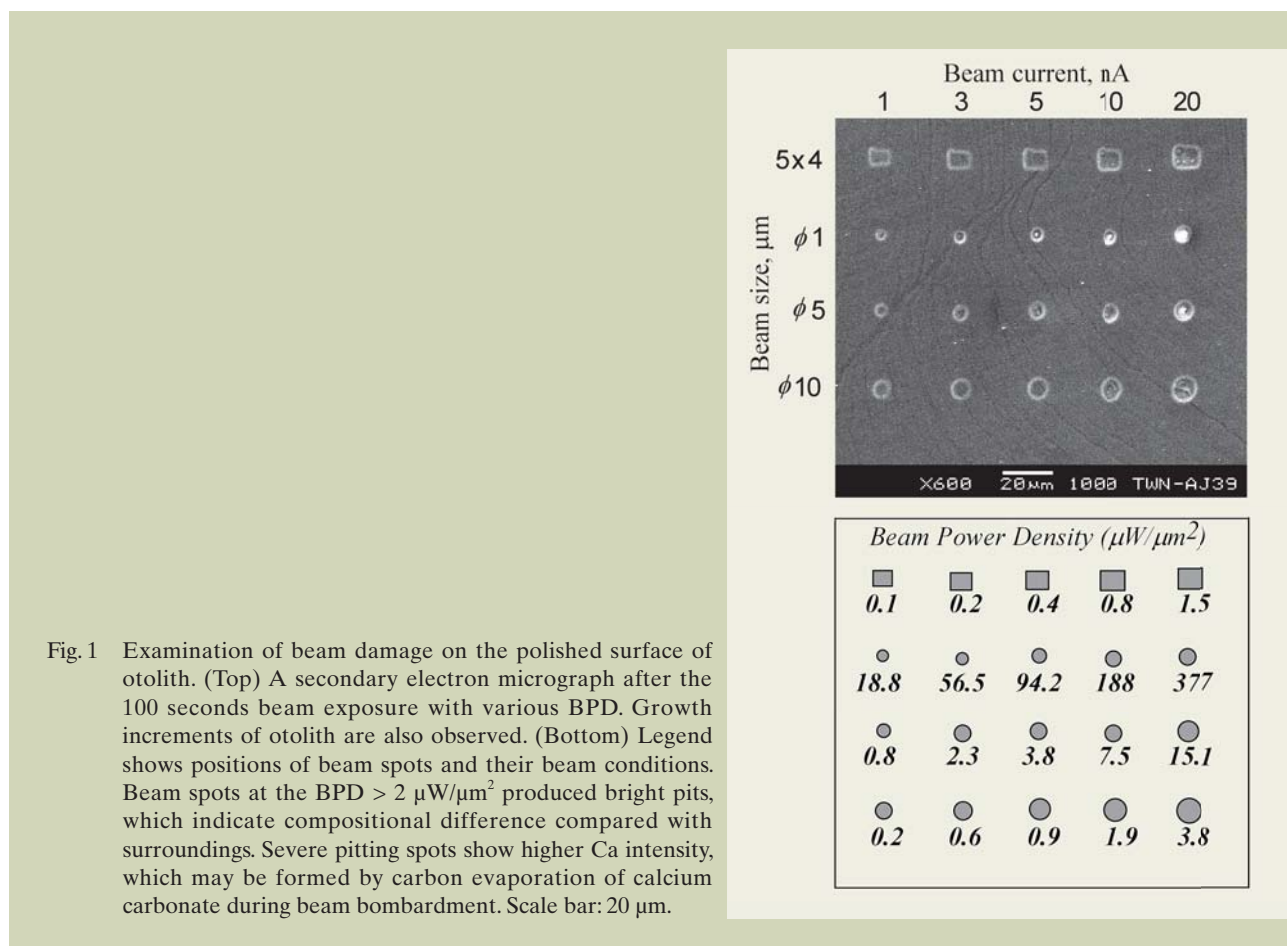


Fig. 1 Examination of beam damage on the polished surface of otolith. (Top) A secondary electron micrograph after the 100 seconds beam exposure with various BPD. Growth increments of otolith are also observed. (Bottom) Legend shows positions of beam spots and their beam conditions. Beam spots at the BPD $> 2 \mu\text{W}/\mu\text{m}^2$ produced bright pits, which indicate compositional difference compared with surroundings. Severe pitting spots show higher Ca intensity, which may be formed by carbon evaporation of calcium carbonate during beam bombardment. Scale bar: 20 μm .

(2) Selection of the diffracting crystal for target elements

Selection of the X-ray diffraction crystal is based on the highest intensities of the target elements. Both lower and upper sides of background counting positions for each target X-ray line were selected with care

to interference peaks using the qualitative line scan analysis. As shown in **Figure 3**, the net intensity of X-ray is calculated with the X-ray baseline intensity. Thus, the height of baseline must be the same between standard materials and otolith. The line scan analysis has been carried out for Ca peak and baseline positions on both Ca and Sr standards, and an otolith.

Counting of Ca $K\alpha$ was made by PETJ crystal

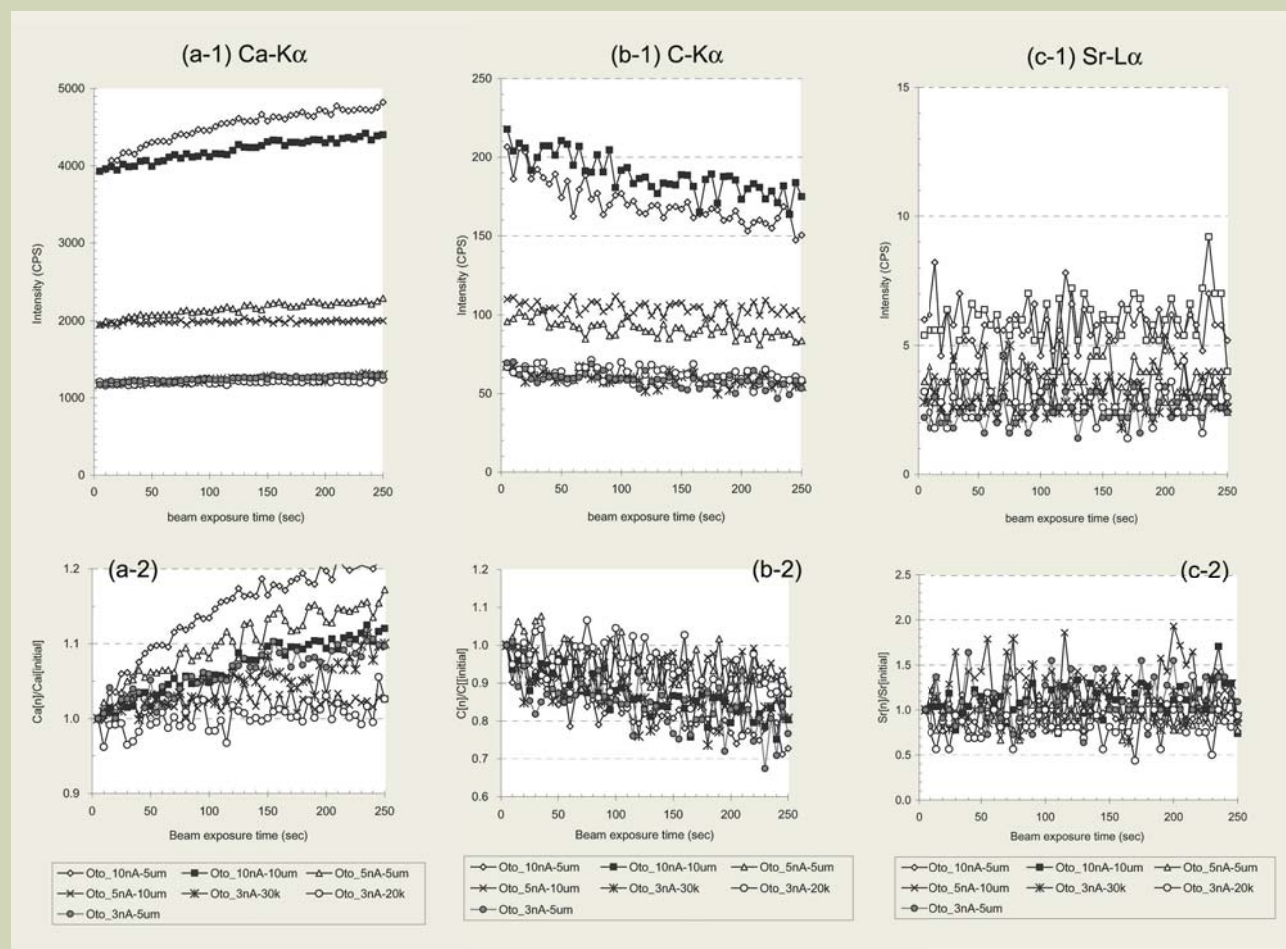


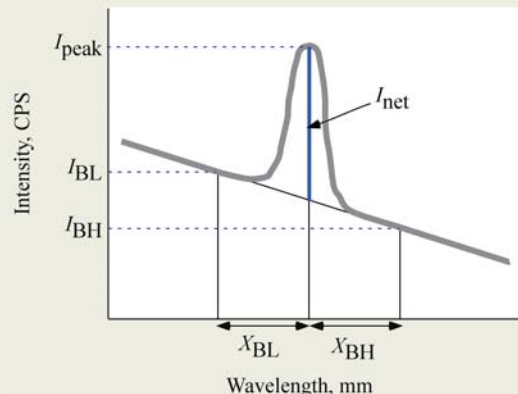
Fig. 2 Transition of X-ray intensities on otolith. Intensities of (a) Ca $K\alpha$, (b) C $K\alpha$, and (c) Sr $L\alpha$ being a function of beam exposure time (sec) at different beam conditions on a Japanese eel otolith. Upper and bottom show alterations of counts and rates of intensities, respectively.

Fig. 3 Measurement of the net peak intensity of target element. I_{bkU} and I_{bkL} are background X-ray intensity (cps) at the positions of upper- and lower side, respectively, and D_{bkU} and D_{bkL} are upper- and lower side distance (in millimeters) of background counting position from the peak position as function of L-values, respectively.

The L-value indicates the distance from the X-ray source (probe spot) to the analyzing crystal. It represents the wavelength detecting position of WDS and is given by the following equation:

$$L \text{ (mm)} = [2R/2d] n\lambda$$

where 2R is diameter of Rowland circle (mm), 2d is spacing of diffracting crystals (\AA : angstroms), n is order of reflection, and λ is wavelength (\AA).



$$I_{net} \text{ (CPS)} = I_{peak} - \frac{I_{BH} \times X_{BL} + I_{BL} \times X_{BH}}{X_{BL} + X_{BH}}$$

(Table 1). As shown in Figure 4, the Ca $K\alpha$ position is isolated with other peaks and there are low-enough baseline both low- and upper-side.

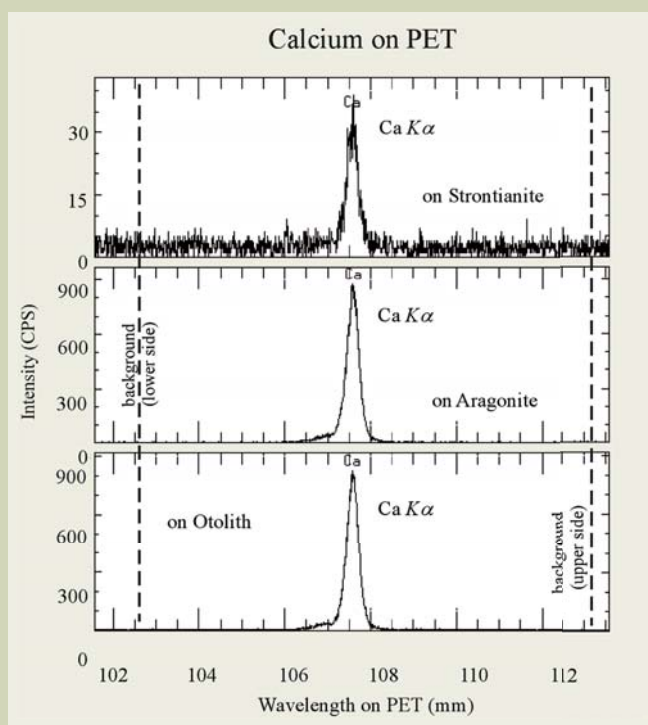
Counting of Sr $L\alpha$ was made by TAP crystal, because intensity of Sr on the TAP is 4-7 times stronger than the intensity on another possible diffracting crystal, such as PET or PETH, at the same beam condition (Fig. 5 and Fig. 6). However, the line scan analysis shows that, Sr $L\alpha$

and Ca $K\alpha$ peaks were observed as interference peaks of the lower side of Sr $L\alpha$ baseline (Fig. 5). In particular case of the Sr standard strontianite, the lower side of baseline is affected by Sr $L\alpha$ peak and their baseline height is 4-5 times higher than both of the Ca-standard aragonite and an otolith baseline (Fig 5-d, e, f). And the position of lower baseline is the same to the lowest limit of TAP, therefore, the TAP is not appropriate to measure

Table 1 An optimum setting of WDS-EPMA to measure Sr/Ca ratios of the otolith.

Machine:			
JEOL EPMA JXA-8900R at the Institute of Earth Sciences, Academia Sinica, Taipei			
Beam conditions			
Acceleration Voltage: 15kV			
Primary beam current: 3nA			
Beam size: $5 \times 4 \mu\text{m}^2$ rectangular scanning beam ($\times 20,000$ in magnification)			
Correction method: Oxide PRZ (Phi-Rho-ZAF)			
Analytical condition			
WDS channel	1	3	4
element	Carbon	Strontium	Calcium
Standard material	Aragonite	Strontianite	Aragonite
(formula)	CaCO_3	$(\text{Sr}_{0.95}\text{Ca}_{0.05})\text{CO}_3$	CaCO_3
WDS setting			
Diffracting crystal	STE	PETH	PET
X-ray Counting position	C $K\alpha$	Sr $L\alpha$	Ca $K\alpha$
Peak position, mm	ca. 124.4	ca. 220.1	ca. 107.5
Background (+), mm	10.5	14.5	5.0
Background (-), mm	8.0	20.0	5.0
X-ray Counting time (total)	50	120	40
Peak, sec	30	80	20
Background (+), sec	10	20	10
Background (-), sec	10	20	10

Fig. 4 Scanning of Calcium X-ray intensity on the carbonate standards (strontianite and aragonite) and an otolith, with diffracting crystals PET. The vertical and horizontal axes are X-ray intensity in count per second (cps) and which is shown as the L-value in mm, respectively. Any interference peak was absence around Ca $K\alpha$ peak on the PET crystal. Measurement positions of each baseline, lower- and upper-side were selected on no interferences positions.



Sr. Although the PET is obtained lower intensity of Sr, there is no base line problem and is enough space to avoid interference peaks, such as Sr $L\alpha$ and Ca $K\alpha$ (Fig. 6). The C $K\alpha$ line was interfered by the carbon-coating itself and was shown broad peak, though the intensities of C $K\alpha$ line were strong enough to examine (Fig. 7). To determine the above 3-elements, it is selected that double PET are measurements for Ca and Sr, the STE is for C

(see Table 1).

(3) Effect of exposure time with Ca, Sr, and C intensity at different beam current and beam size

Relations between the X-ray intensities and beam exposure time were determined for Ca $K\alpha$, C $K\alpha$ and

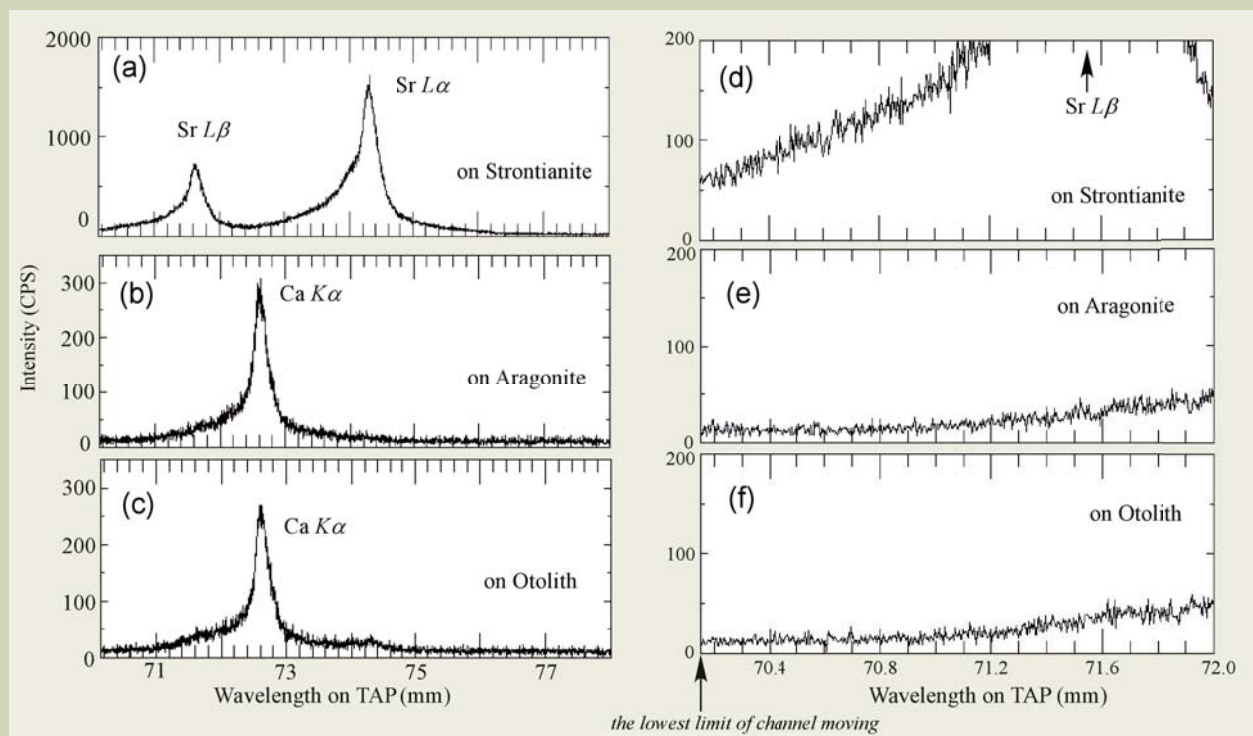


Fig. 5 Scanning of Strontium X-ray intensity on the carbonate standards (strontianite and aragonite) and an otolith, with diffracting crystals TAP. On the TAP crystal, Sr $L\alpha$ on (a) strontianite, and (b) Ca $K\alpha$ on aragonite, and (c) an otolith are observed as interference peaks of Sr $L\alpha$ (target peak), respectively. And baseline heights are considerably different among (d) strontianite, (e) aragonite and (f) an otolith.

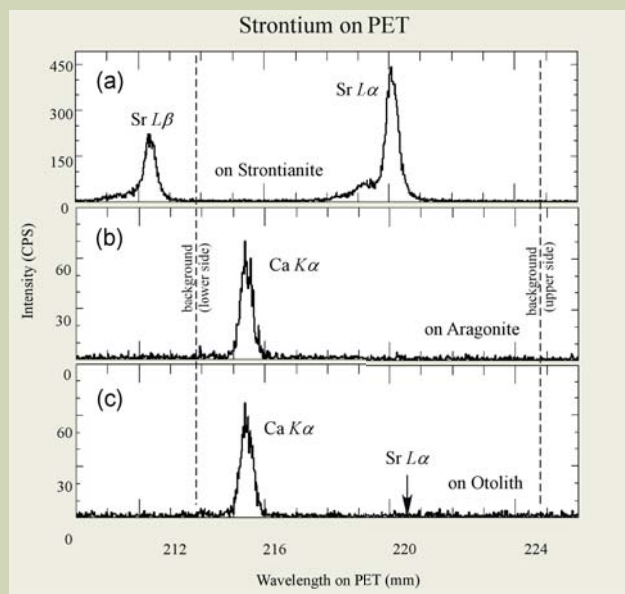


Fig. 6 Scanning of Strontium X-ray intensity on the carbonate standards (strontianite and aragonite) and an otolith, with diffracting crystals PET. Measurement positions of each baseline, lower- and upper-side were selected on no interferences positions.

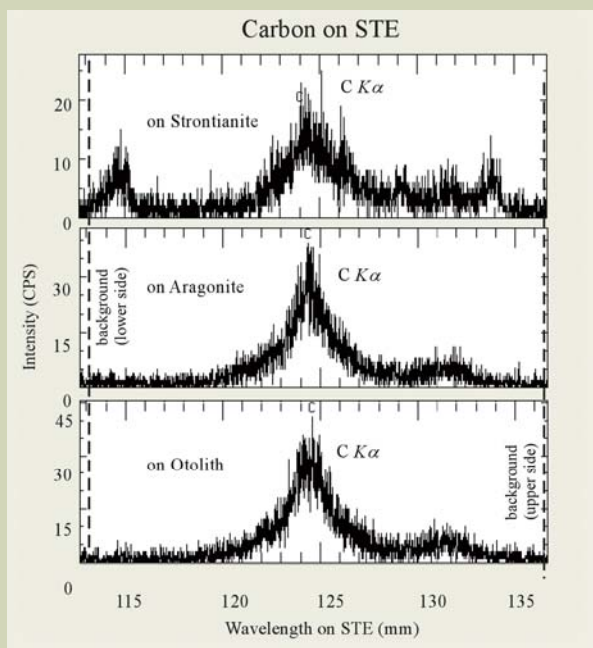


Fig. 7 Scanning of Carbon X-ray intensity on the carbonate standards (strontianite and aragonite) and an otolith, with diffracting crystals STE.

Sr $L\alpha$ of the standards, calcite (Fig. 8), aragonite (Fig. 9) and strontianite (Fig. 10) at the BPD ranging from 0.2 to $7.5 \mu\text{W}/\mu\text{m}^2$, as well as on the otolith experiment (Fig. 2). The Ca, Sr and C intensities were counted for 5 sec \times 25 cycles at the same spot after setting each peak position. Total beam exposure time is 250 sec at each analysis spot.

The intensities of Ca, C and Sr were greater at higher than lower beam currents (Fig. 8, 9, 10). At higher beam current on calcite and aragonite, the intensities of Ca increased and C decreased with increasing exposure time, and the extent of alteration depended strongly upon the BPD. At the lowest BPD (0.2: 3 nA – $5 \times 4 \mu\text{m}^2$ rectangle beam), Ca intensities on calcite are slightly increasing with the time (Fig. 8a-1 and 8a-2), though Ca on aragonite did not change throughout the analysis

for 250 sec (Fig. 9a-1 and 9a-2). This behavior is also observed in case of otolith time study (Fig. 2). On the other hand, the intensities of C were severely altered under the higher BPD beam compared with that of a larger beam size regardless of beam current (Fig. 8b and 9b). Changes of Sr intensities were smaller than those of other two elements regardless of the BPD and the exposure time (Fig. 10).

These observations indicate that the surface condition of specimen has been modified by the electron beam bombardments, and the extent of alteration depended upon the BPD, primarily beam diameter as well as beam exposure time determined the extent of the alteration. It is not only happened an organic carbonate otolith but also occurred on the inorganic carbonates,

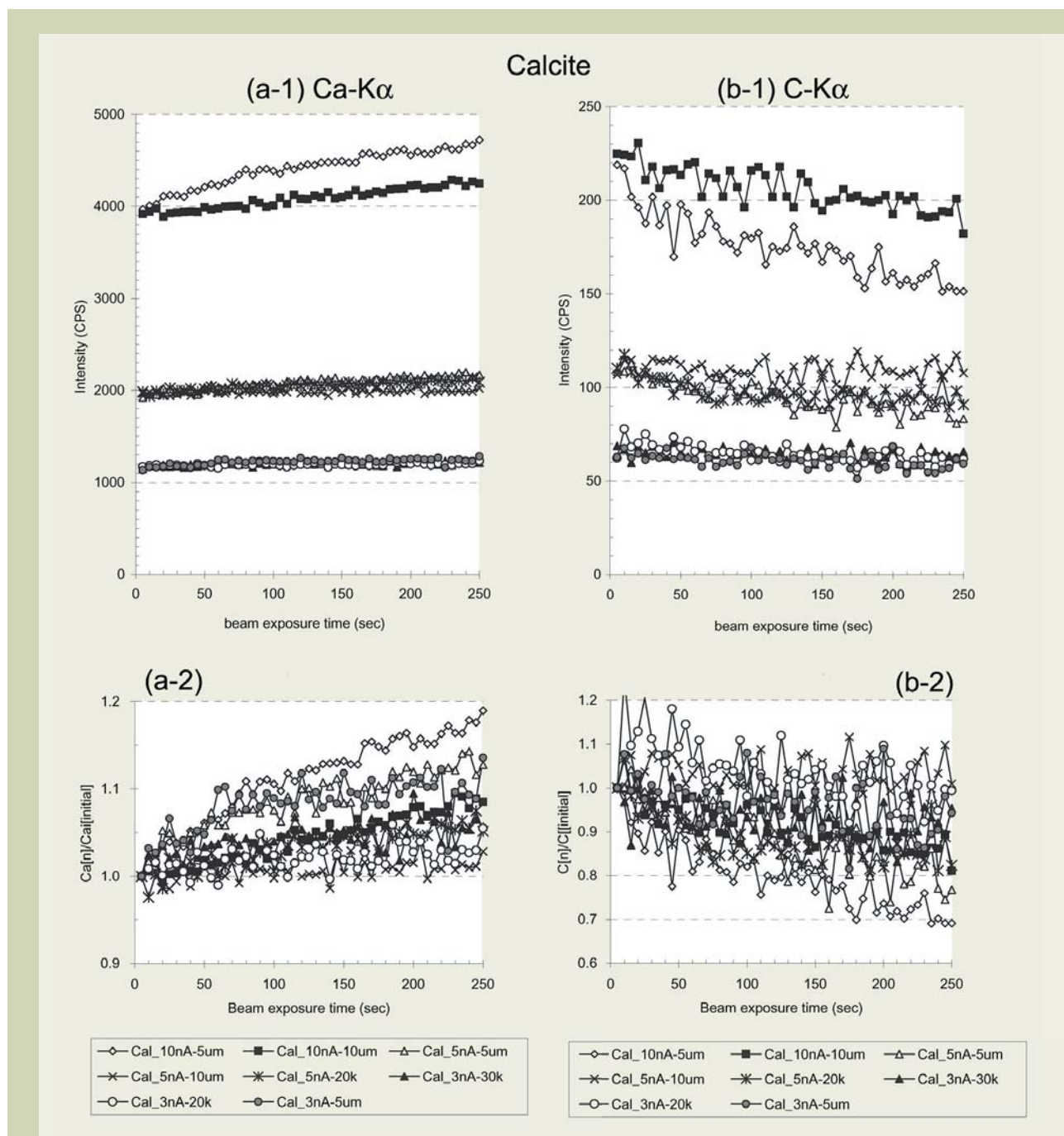


Fig. 8 Intensities of (a) Ca $K\alpha$, and (b) C $K\alpha$ being a function of beam exposure time (sec) at different beam conditions on calcite standard. Upper and bottom show alterations of counts and rates of intensities, respectively.

calcite and aragonite. The changes in intensities of Ca and C with exposure time may be due to changes of the original surface by beam damage within a few minutes of exposure.

During beam exposure for analysis, the entire energy of the incident electron beam is dissipated in the form of heat at the point of impact [19]. The degree of heating is depending upon the BPD and the type of specimen. Casting [24] estimated that the rise in temperature (ΔT , °C) resulting from an electron beam diameter d (μm) and thermal conductivity k (W/cm) of target is given by

$$\Delta T = 4.8 \left(\frac{E_0 I}{kd} \right)$$

where E_0 is the incident energy of the electron beam (kV), and I is beam current (μA).

Plotts [20] determined that the temperature rise in lower k minerals, such as calcite ($k = 0.05$ [25]), and it could be large cause of decomposition and/or structural alteration ($\text{CaCO}_3 \rightarrow \text{CaO} + \text{CO}_2$). Although there is no report about the thermal conductivity k of aragonite, it is expected that the aragonite-carbonate is also decomposed during the beam heating from the results from Figure 9. The decrease of C intensities might be related with evaporation effect of the CO_2 from the beam spot, and as a result increasing of Ca intensities occurred during beam exposure. It is suggested that the effect of beam damage should indicate wrongly estimation of chemical composition. Thus, the temperature rise on the

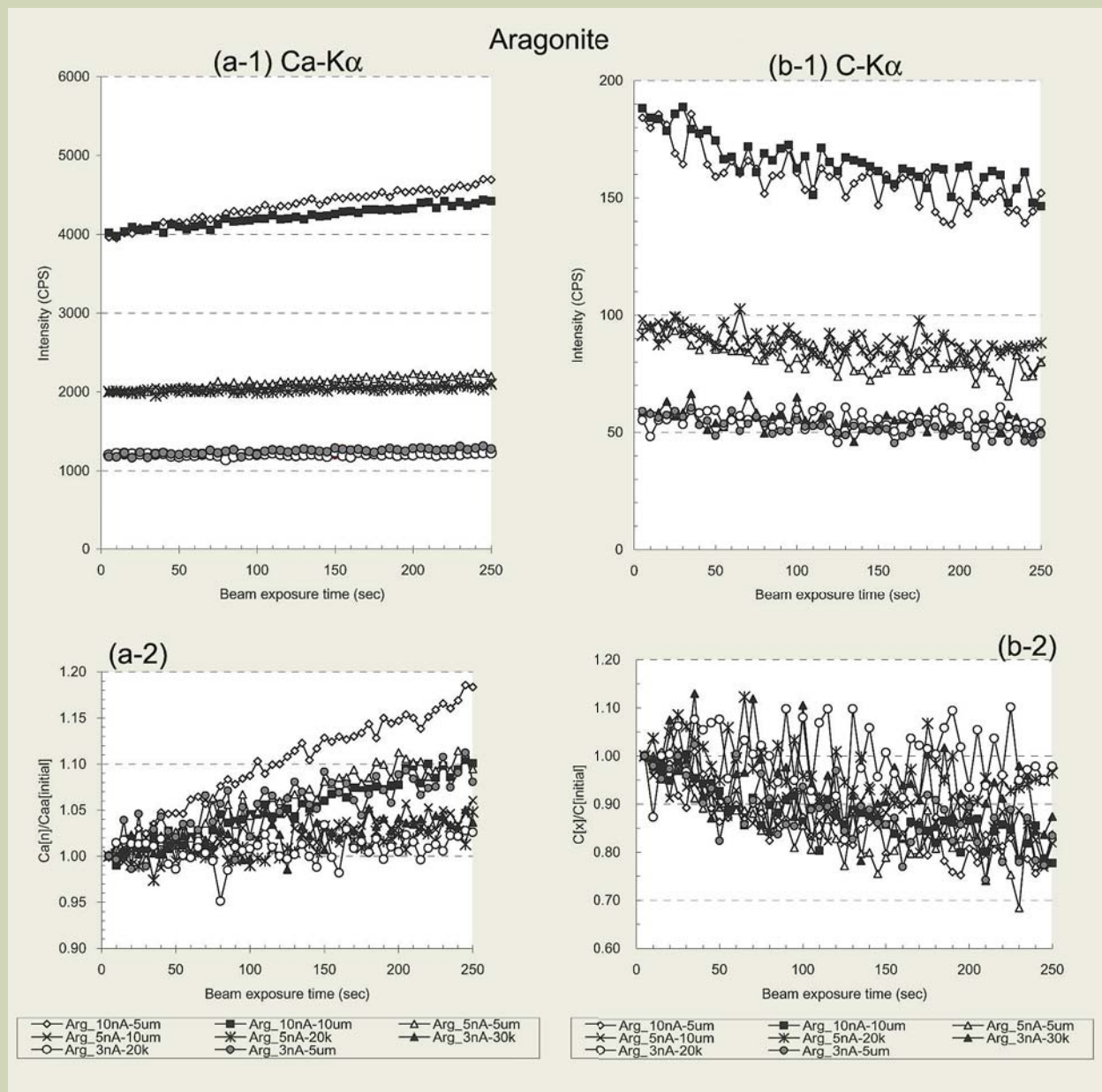


Fig. 9 Intensities of (a) Ca $K\alpha$, and (b) C $K\alpha$ being a function of beam exposure time (sec) at different beam conditions on aragonite standard. Upper and bottom show alterations of counts and rates of intensities, respectively.

surface of otolith should be considered. This indicates that beam damage caused by a high BPD may have led to inaccurate quantifications of otolith chemical composition.

This phenomenon was also suggested by Gunn et al. [15]. And they recommended $1.2 \mu\text{W}/\mu\text{m}^2$ in the BPD, which was conducted by 15 kV, 25 nA and 20 μm of acceleration voltage, beam current and diameter, respectively. However, the width of increments, growth rings, of otolith is smaller than a few μm , so that the size of electron beam should be required to reduce as smaller as possible to obtain the special resolution. In some of previous studies, a small beam diameter

(smaller than 1 μm) and an extremely high BPD (greater than $100 \mu\text{W}/\mu\text{m}^2$) was used to measure Sr/Ca ratios in otoliths. As mentioned previously, a small beam diameter and high BPD may lead to severe otolith surface damage and the alteration of otolith chemical composition. Subsequently, this could lead low precision and inaccurate quantification of otolith Sr/Ca ratios estimations. Accordingly, a small beam diameter and a high BPD should not be used for measurement of Sr/Ca ratios in otoliths.

To avoid decomposing the sample, various preventive measurements can be applied. The beam current can be reduced or, alternatively, the beam may

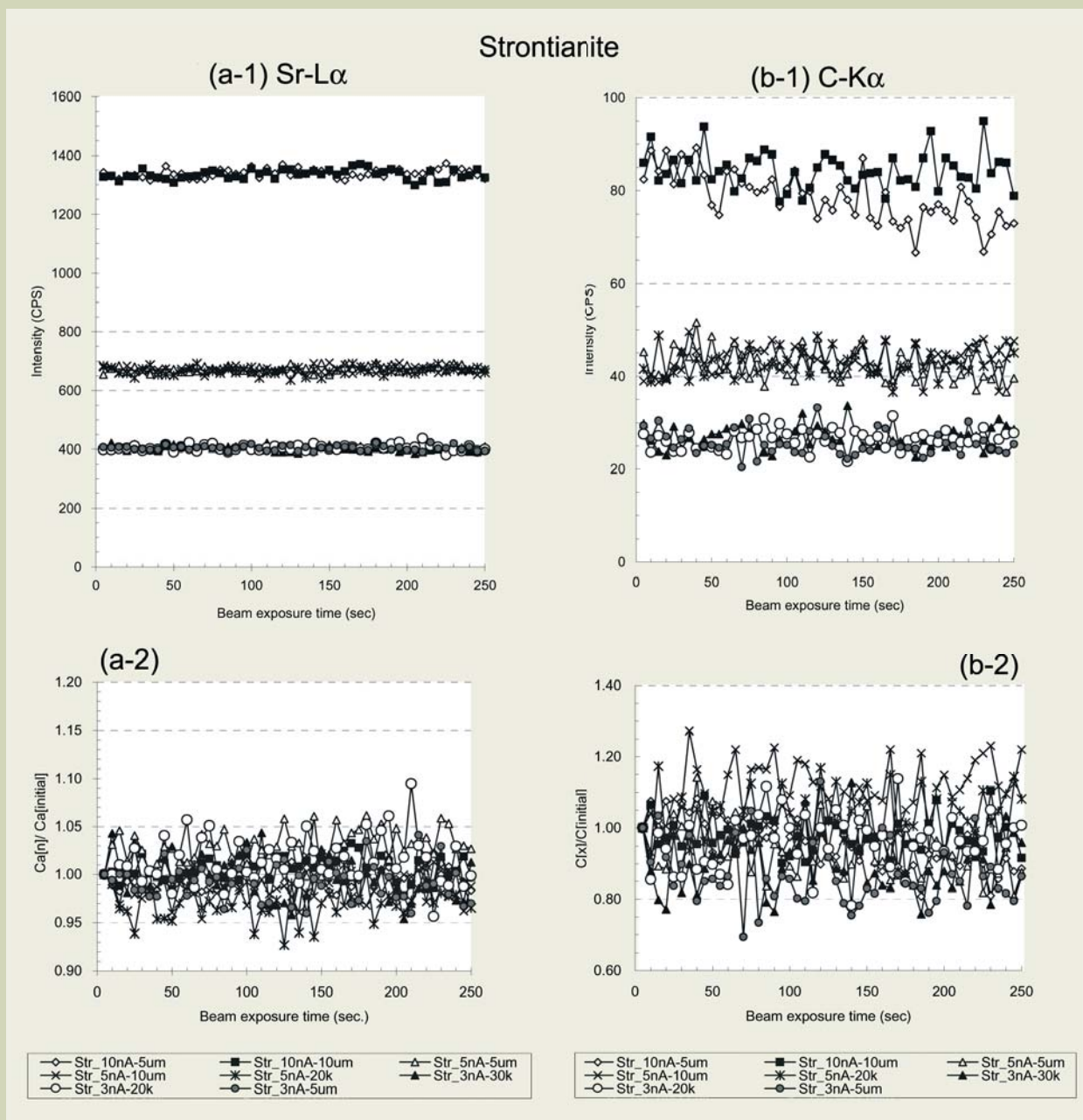


Fig. 10 Intensities of (a) Sr $L\alpha$ and (b) C $K\alpha$ being a function of beam exposure time (sec) at different beam conditions on strontianite standard. Upper and bottom show alterations of counts and rates of intensities, respectively.

be defocused to allow energy dissipation to spread over a larger area. As suggested by the alteration of Carbon under a focused beam, the use of a focused beam less than 1 or 2 μm should be avoided. This does, however, sacrifice spatial resolution. Again that wider electron beam is, on the other hand, inappropriate for analysis of the fine growth increments in otoliths. Consequently, it must be accepted that beam exposure time should be shortened and that beam current and diameter should be as low as possible. Because of these considerations, it is suggested that beam conditions are optimal when the BPD is less than $0.5 \mu\text{W}/\mu\text{m}^2$ and beam diameter $>2 \mu\text{m}$. Note that the lower probe current (less than 1 nA at 15 kV)

is not acceptable for the analysis of otolith because of low Sr $L\alpha$ intensity. From the experiment of the effects of BPD on the X-ray intensities of Ca, C and Sr, four beam conditions were found to have a BPD less than 1 or $0.5 \mu\text{W}/\mu\text{m}^2$, which appears to minimize damage and therefore are acceptable for the analysis of otolith Sr/Ca ratios. According to the changing of X-ray intensities on both standard and otolith, the optimal beam conditions for the analysis of Sr/Ca ratio in the otoliths is suggested to be 3 nA and $5 \times 4 \mu\text{m}^2$ beam (BPD = $0.2 \mu\text{W}/\mu\text{m}^2$).

(4) Variability of intensity in relation to exposure time

To confirm the precision of background counting in the function of counting time, the smallest detectable peak was defined. Additionally, to achieve an appropriate counting time for Sr in the quantitative otolith analysis, precision of peak analysis was examined using the standards at conditions of the lowest BPD ($0.2 \mu\text{W}/\mu\text{m}^2$: 3 nA and 5×4 rectangle beam) on the Sr-standard strontianite. The beam exposure time on each counting was set from 10 to 240 sec. The X-ray intensity was measured from 10 different points.

The relative standard deviation (RSD) of X-ray intensities of Sr in relation to beam exposure time is shown in **Figure 11**. The RSD of both lower- and upper-side backgrounds decreased gradually from 5 % to less than 2 % with an increase in the exposure time. The RSD of the Sr peak decreased gradually from 7 % to 3 % with increasing exposure time up to 80 sec. However, at an exposure time longer than 180 or 240 sec, the RSD of baselines slightly increased, indicating that the X-ray intensities are altered if exposure times exceed 180 or 240 sec even at lower BPD. Whereas the precision of Ca analysis were <0.5 % RSD, regardless of the beam conditions, at an exposure time between 20 and 40 sec. Because Ca can be measured simultaneously with Sr by multiple WDS channels, total analysis time including peak and background counting should be considered only for Sr analysis. Therefore, it is desirable that the total analysis time was restricted less than 180 sec for each spot, and peak-counting time should be between 80 and 120 sec, and as result the each background-counting time should be between 20 and 30 sec.

(5) Precision of Sr measurement in otolith

The sagittal otolith generally contain less than 1 wt% of Sr. However, it must be used higher Sr content standard (strontianite: Sr = 59.4 wt%) because it is unable to find a low-concentration and homogeneous material of the carbonate matrix. To confirm the precision of Sr analysis, Sr contents were measured with the beam current of 3 nA and $5 \times 4 \mu\text{m}^2$ beam, and the peak and bases counting times were 80 sec and 20 sec, respectively (so called *an optimum beam condition*), using chemical-known materials, calcite, apatite and barite. The results and analytical reproducibility ($1\sigma_{\text{mean}}$) of SrO are shown in **Figure 12**. The measured and recommended SrO (wt%) was highly linearly correlated ($r = 0.991$).

The Sr contents in the otolith and their measurement precision were quantified using the *optimum beam condition*. Sr contents were measured from 5-points at 4-different increments of the otolith under the electron

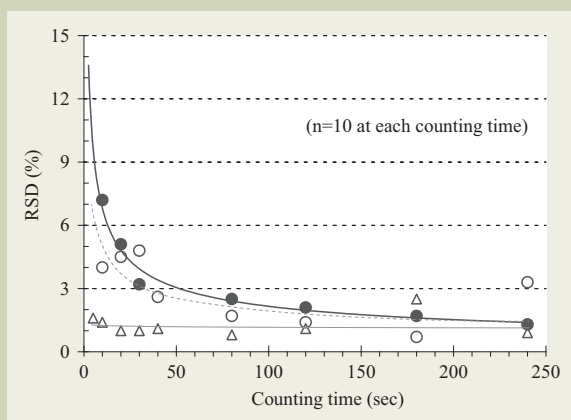


Fig. 11 Accuracy of X-ray counting at different counting time (sec) for Sr $L\alpha$ peak (solid circles), lower side background (open circles), and upper side background (open triangles) on strontianite.

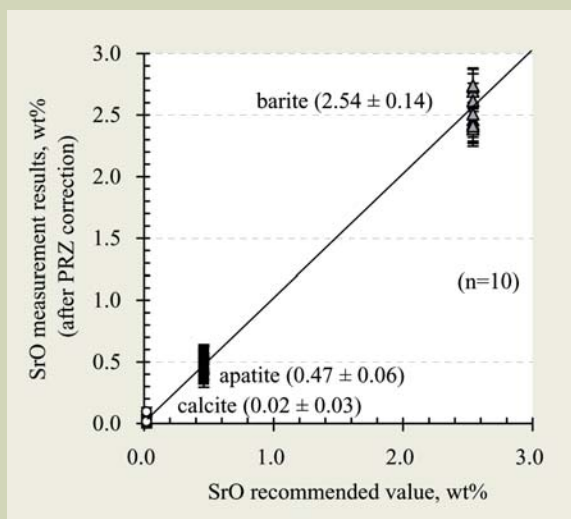


Fig. 12 Correlation between the measurement results and the recommended values of SrO (wt%) of the chemical-known standard materials at the optimum beam condition. Symbol and the recommended value; open circle: calcite (0.02 wt%); solid square: apatite (0.46 wt%); triangle: barite (2.537 wt%). Measurements have been carried out for 10 times on each material and shown mean value and 1σ error in wt%, respectively.

image. The relation between the net peak intensity of Sr, and Sr analysis result, which after corrected by the PRZ, are shown in **Figs. 13** and **14**, and **Table 2**. The standard deviation (SD) of Sr in otoliths in CPS (count per second) were obtained to be 0.29 cps at the highest net intensity of 3.8 cps (RSD = 7.6%; no.4 in Table 2), and 0.22 cps at the lowest net intensity of 0.9 cps (RSD = 24.4%; no.1). These error ranges were computed for the precision of Sr contents in otolith; Sr = 0.14 ± 0.03 wt% (no.1), 0.33 ± 0.04 wt% (no.2), 0.46 ± 0.05 wt% (no.3) and 0.61 ± 0.05 wt% (no.4). Assuming that Ca contents in otoliths were 39.0 wt%, Sr/Ca ratios in eel otoliths were estimated to be $3.59 \pm 0.77 \times 10^{-3}$ (no.1), $8.46 \pm 1.03 \times 10^{-3}$ (no.2), $11.79 \pm 1.28 \times 10^{-3}$ (no.3), and $15.64 \pm 1.28 \times 10^{-3}$ (no.4), respectively. If it is assuming maximum error of Ca (RSD < 1.0%), the ranges of error in Sr/Ca ratios are smaller than these estimation.

Study of migratory behavior and habitat of three major temperate species of eels by otolith microchemistry

Most of fishes migrate with various spatiotemporal orders. Classification of fish migration is divided into two types. Diadromous fishes migrate between fresh- and sea- or brackish-water, whereas non-diadromous fishes migrate within freshwater (e.g., carp) or seawater environment (e.g., tuna). Diadromous fishes are, further, divided into 3-types; anadromous, catadromous and amphidromous. Anadromous fishes are spawning in the freshwater river and grown in seawater (e.g. salmon). Catadromous fishes are spawning in seawater and grown in freshwater (e.g., eel), and amphidromous fishes migrate between sea- and fresh-water bodies frequently (e.g., sweetfish “*ayu*” and smelt “*shi-sya-mo*”).

Catadromous eels are widely distributed in the world. In particular, three major temperate species, Japanese eels *Anguilla japonica* in the East Asia, American eels *Anguilla rostrata* in the Northeast America, and European Eel *Anguilla anguilla* in the West to Northwest Europe and North Africa are valuable for economy, aquaculture and fishery (**Fig. 15**). Habitat of Japanese eel is in the NW Pacific Ocean, and is found in brackish water lakes and estuaries and freshwater rivers from southern Taiwan to Japan in Northeastern Asia. Their leaf-like larvae, *leptocephali*, drift with the North Equatorial Current and Kuroshio from their oceanic spawning grounds, near the Mariana Islands, to the continental shelf of northeastern Asian countries [13, 26, 27]. In the Atlantic, on the other hand, American and European eels spawn in the Sargasso Sea and migrate along the Gulf Stream for the East Coast of North America and the West to Northwest Europe and North Africa. They then metamorphose into transparent glass eels in coastal waters and become pigmented elvers in the estuary. After upstream migration, the elvers become yellow eels and live around estuary and in freshwater rivers for approximately 5 to 20 years [8, 12, 28], and then, once they have reached sexual maturity, migrate downstream to the open ocean to spawn.

Otolith microchemistry is a good tool to indicate migration pattern from individual fish. Patterns of otolith Sr/Ca ratios from core to edge illustrate eel’s movement. Since the last decade, more than 1000 otoliths have been studied from the difference water bodies (Fig. 15). In this

section, results of application studies on three major temperate species of eels are presented.

(1) Analytical procedure

Sagittae, the biggest of the 3 pairs of otoliths, were removed from the inner ear for examination of microchemistry. The procedure of otolith preparation for the analysis of Sr and Ca is similar to Tzeng et al.

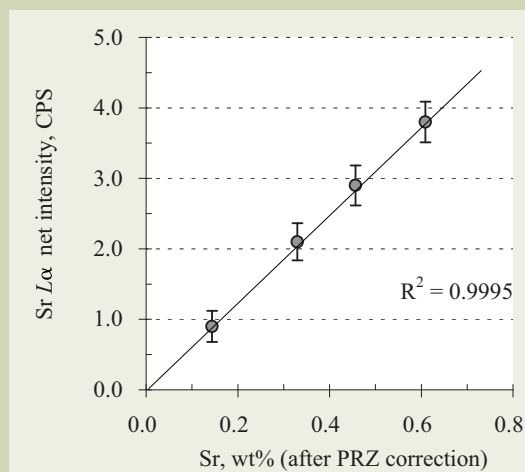


Fig. 13 Correlation of Sr $L\alpha$ intensities (CPS: counts per second) and Sr concentrations (wt% after PRZ correction) on otolith samples.

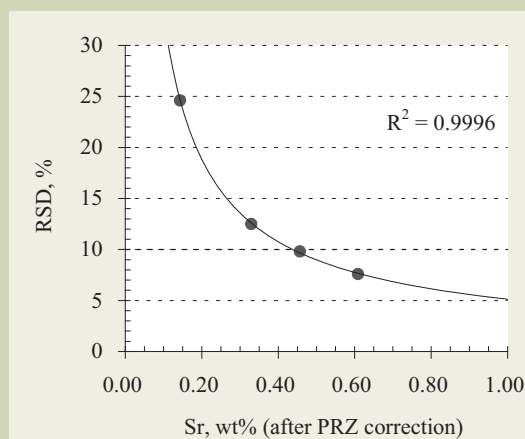


Fig. 14 Estimated RSD (Relative Standard Deviation) of Sr measurements, which obtained by the optimum beam condition.

Table 2 Sr measurement accuracy of otolith.

	Sr, wt%	measured CPS	S.D. (CPS)	S.D. (%)	Sr error in wt%
1	0.14	0.90	0.22	24.6	± 0.03
2	0.33	2.10	0.26	12.5	± 0.04
3	0.46	2.90	0.28	9.8	± 0.05
4	0.61	3.80	0.29	7.6	± 0.05

CPS: count per second, S.D.: standard deviation (1σ).

[13]. The sagittal otolith was cleaned with distilled water, air dried, embedded in epoxy resin, ground and then polished along the sagittal plane with alumina compound until the primordium (core) was exposed. All specimens were cleaned with distilled water again in an ultra-sonic bath and air dried before the carbon coating.

Concentrations of both Sr and Ca in otoliths were measured using *the optimum beam conditions* (Table 1) along a sagittal section from the primordium (core) to

the otolith edge at an interval of 10 μm (Fig. 16). After the EPMA study, growth increments of most of otolith were counted for age determination.

(2) Migration patterns of Japanese eels in Taiwan

To understand the environmental history of the Japanese eel after migration from off shore spawning

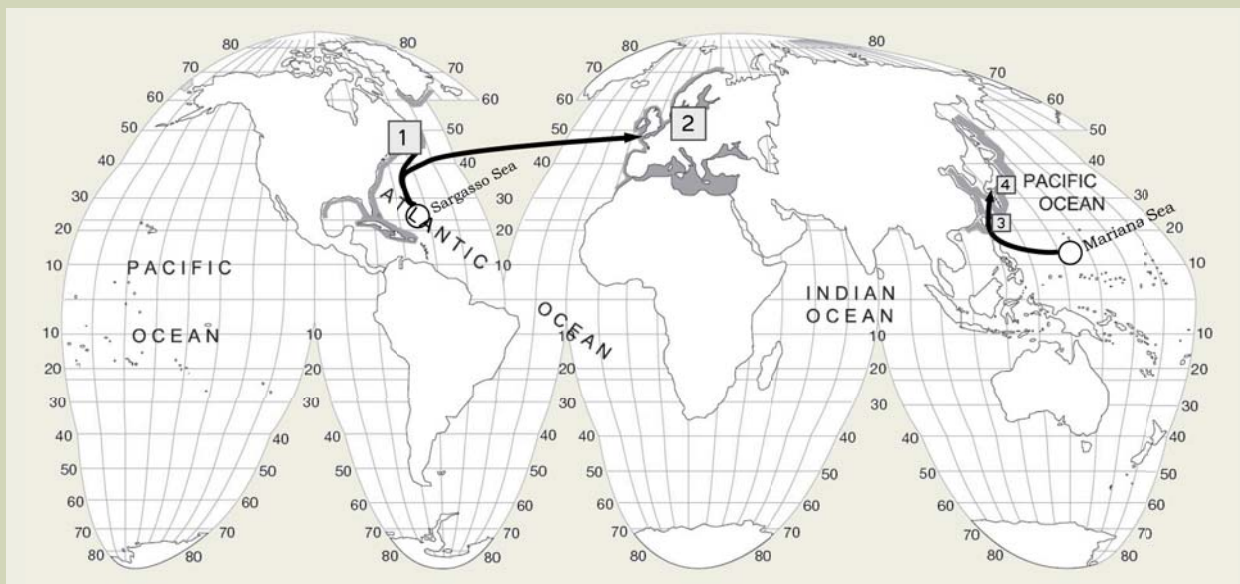


Fig. 15 Main study fields showing the geographical range of each species [35]: American eel *Anguilla rostrata*, (1) New Brunswick, Quebec, and Nova Scotia, Canada [13, 30, 36-41]; European eel *A. anguilla* (2) Baltic Sea region, Sweden, Lithuania and Latvia [32, 33, 42-44]; Japanese eel *A. japonica*, (3) Taiwan; and (4) Japan [14, 28, 29]. Solid lines and open circles represent expected paths of upstream migration (with the Gulf Stream in the Atlantic and the Kuroshio Current in the Pacific), and spawning sites (Sargasso Sea in the Atlantic and Mariana Sea in the Pacific), respectively.

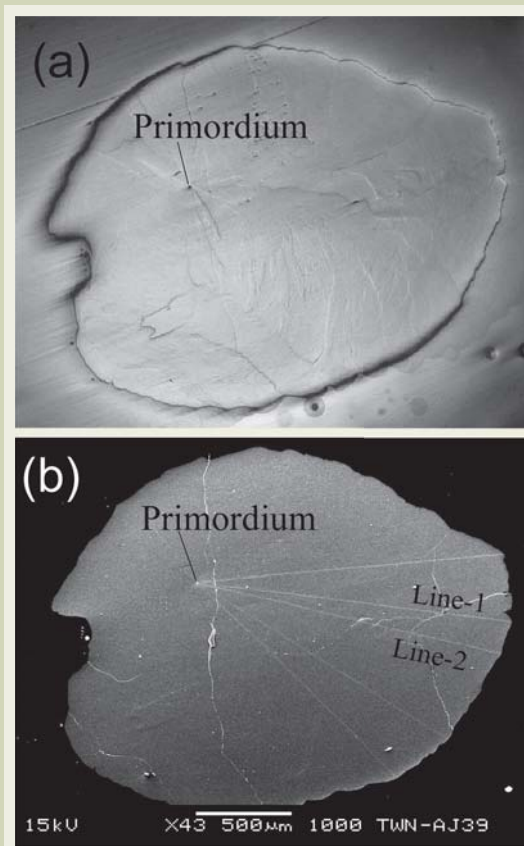


Fig. 16 (a) Optical micrograph of a polished otolith. (b) Secondary electron micrograph of polished surface of otolith after the transect analyses with 10 μm intervals. Analytical tracks are observed as thin-white lines on the surface. Obtained results from Line -1 and -2 are shown in Fig. 17-c (sample D-39).

grounds to estuaries, the temporal change of Sr/Ca ratios in otoliths of eels collected several estuary areas in southwestern Taiwan were examined. A total of over 200 otoliths were measured and the results have been reported [14, 28, 29]. Among them, four typical migratory patterns were described (Fig. 17). Selected four otoliths of Japanese eels from Taiwan were examined with two lines to confirm reproducibility of analysis as well. The ratios on lines #1 and #2 of the same otolith were identical at the same distance from the core, indicating that the analytical precision was acceptable to discussion. During the *leptocephalus* marine stage of early life, Sr/Ca ratios were similar among individuals and increased from $6\text{--}10 \times 10^{-3}$ (Sr contents: approx. 0.2–0.4 wt%) in the core to approximately $16\text{--}18 \times 10^{-3}$ (Sr: approx. 0.6–0.8 wt%), an initial peak at a distance 60–100 μm from the core. Subsequently, decreases once to approximately 7×10^{-3} (Sr: <0.3 wt%) were detected in all of the otoliths (Fig. 17). This indicates that the environmental history of the *leptocephalus* stage was similar among individuals. However, beyond the *leptocephalus* stage the

Sr/Ca ratios dropped to below 1×10^{-3} (Sr: <0.05 wt%) in first half of otoliths T-54, T-21 and D-39 (Figs. 17a, 17b and 17c), whereas the ratios in otolith T-27 dropped to an intermediate level of 3.5×10^{-3} (Sr: 0.14–0.16 wt%: Fig. 17d). These measurements were detected at a distance of 180–210 μm from the core. Following the initial drop, Sr/Ca ratios in the otolith of T-54 remained at less than 4×10^{-3} (Sr: <0.15 wt%) until the otolith edge. The otoliths of T-21 and D-39 showed a different pattern where ratios increased from a lower level of 4×10^{-3} and reached a secondary peak of $8\text{--}12 \times 10^{-3}$ (Sr: approx. 0.3–0.5 wt%). Ratios at the second peak were lower than that of the initial peak in the core area, and continued to gradually decrease. The Sr/Ca ratios in the otolith of T-27, on the other hand, did not decrease as low as others, and the ratios remained at a relatively higher level of $6\text{--}10 \times 10^{-3}$ (Sr: 0.3–0.4 wt%).

These observations indicate that the Sr/Ca patterns beyond the initial peak can be roughly divided into 4 types (Fig. 18); namely, Type A: the Sr/Ca ratios decreased to a lower level ($< 4 \times 10^{-3}$) and remained at that level there-

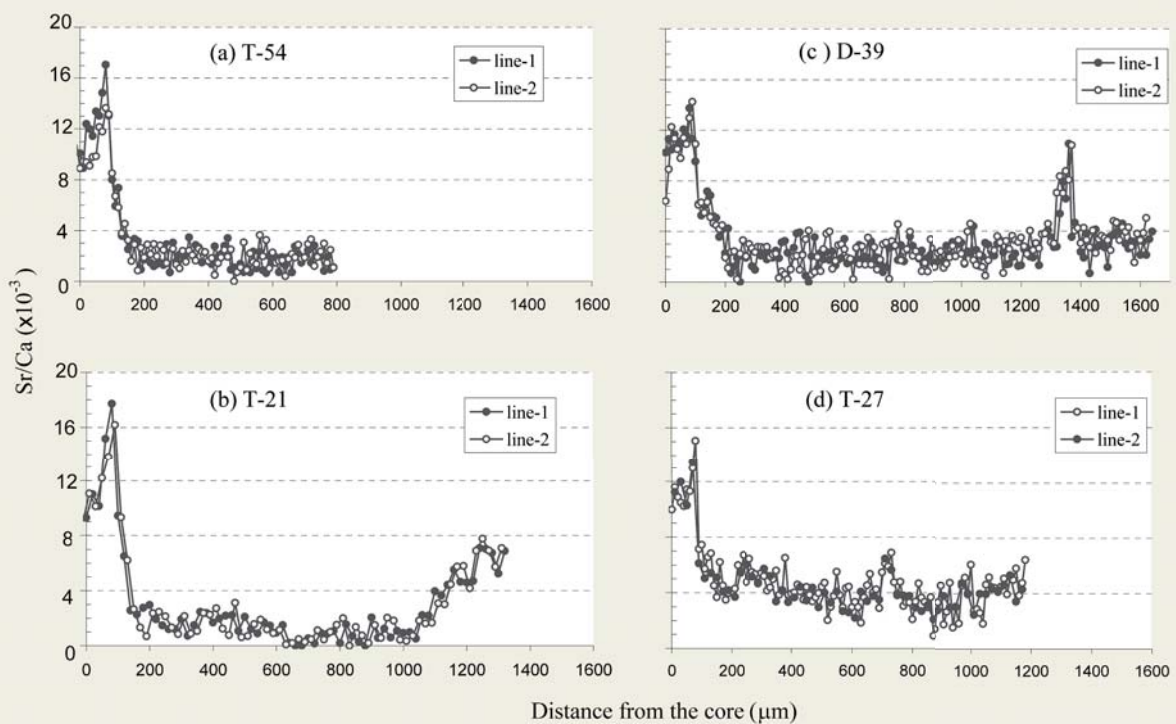
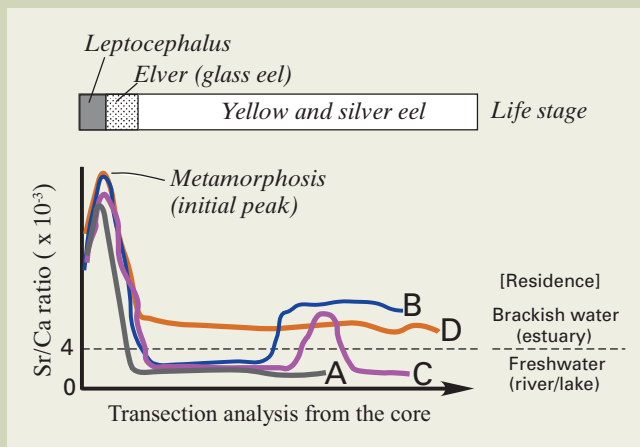


Fig. 17 Sr/Ca ratios determined on 2 parallel transect lines from the primordium to the edge in otolith. The vertical and horizontal axes are Sr/Ca ratio ($\times 10^{-3}$) and distance from the primordium. Interval of analysis spot is 10 μm . [14, 28, 29].

Fig. 18 Schematic diagram of migration patterns of Japanese eels in Taiwan as indicated by the time series change of Sr/Ca ratios in otoliths. Transition of freshwater and brackish water residence is suggested by approximately 4×10^{-3} in Sr/Ca ratio.



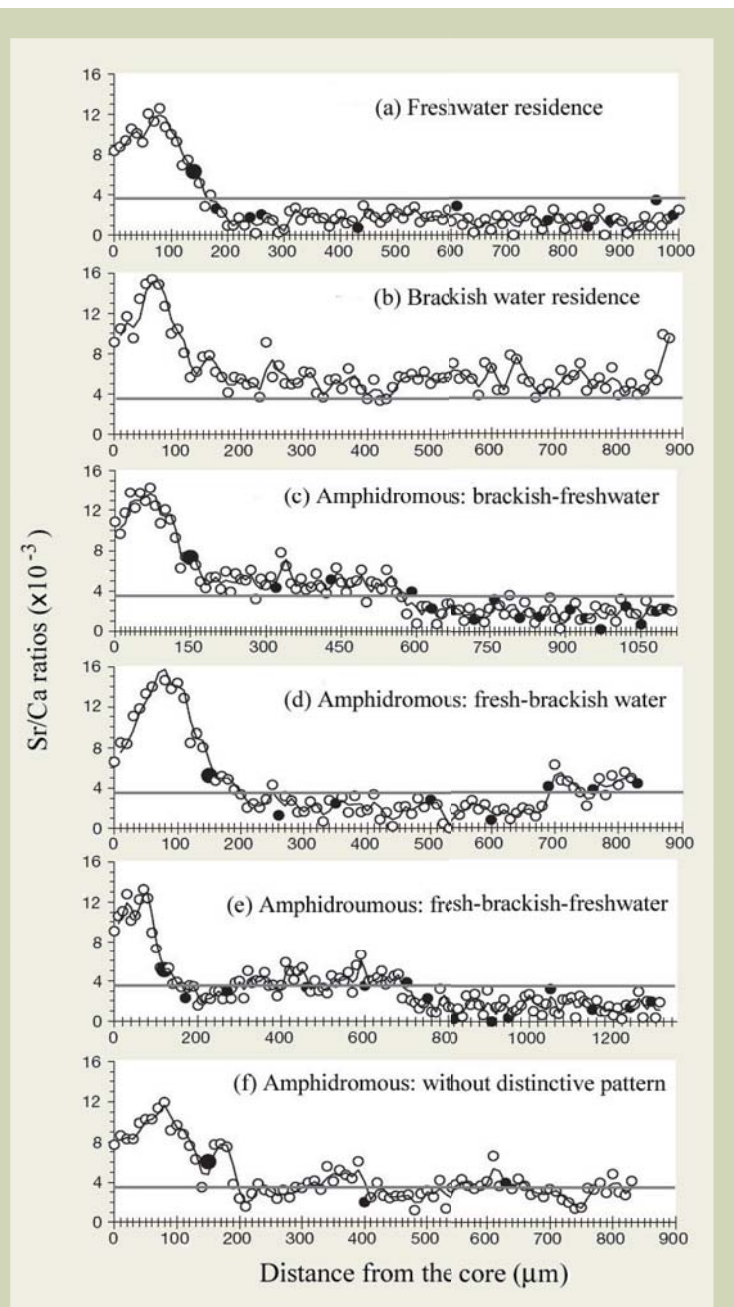
after; Type B: the ratios decreased in a manner similar to those of Type A, but increased to the secondary peak of approximately $6-10 \times 10^{-3}$; Type C: the ratios decreased and increased in a manner similar to those of Type B, and decreased to the lower ratio again; Type D: the ratios did not decrease to a level as low as others type, and remained between 1 and 6×10^{-3} . According to the Sr/Ca patterns and their captured records of eels, each pattern indicates different migration histories as follows; Type A: a freshwater residence; Type B: An amphidromous behavior as residence in freshwater, and shifted brackish water residence; Type C: An amphidromous behavior as residence in freshwater, and shifted brackish water residence, then freshwater residence again; TypeD: a brackish water residence.

(3) Migration patterns of American eels in Northeast Canada

The Sr/Ca ratio transects along the otolith radius,

from core to edge, illustrating 6 life-history patterns determined by otolith Sr/Ca ratio analyses on 162 American Eels *Anguilla rostrata* captured the St. Jean River watershed (lat. 48°N) in Quebec (Canada). Among the 162 eels sampled, we predominantly observed an amphidromous migratory pattern (42%) during the yellow-stage growth phase, followed by brackish (38%) and freshwater (20%) residence behavior. Six type are described as follows: Type-FR (Fig. 19-a): Residence in freshwater. Entrance in freshwater between Year 1 (elver mark) and Year 2. Type- BR (Fig. 19-b): Residence in brackish habitat (for eel [b] otolith was not clear enough to allow a correct age determination). Amphidromous behaviors are divided into 3 groups, namely, Type-A_{BF} (Fig. 19-c): Residence in brackish environment for more than 2 yr, then movement into freshwater. Type-A_{FB} (Fig. 19-d): Residence in freshwater then movement to brackish habitat. Type-A_{FBF} (Fig. 19-e): Freshwater residence, movement to brackish estuary then movement to freshwater. And Type-A_{ND} (Fig. 19-f):

Fig. 19 Representative migratory patterns of American eels *Anguilla rostrata* from St Jean River watershed in Quebec (Canada). The Sr/Ca ratio transects along the otolith radius, from core to edge, illustrating 6 migratory patterns: (a) Type-FR: freshwater residence [sample # IT-206], (b) Type-BR: brackish water residence [# IT-061], (c) Type-A_{BF}: amphidromous [brackish-freshwater: # IT-285], (d) Type-A_{FB}: amphidromous [freshwater-brackish: # IT-014], (e) Type-A_{FBF}: amphidromous [freshwater-brackish-freshwater: # IT-211], (f) Type-A_{ND}: amphidromous [non distinctive pattern: IT-116]. The Sr/Ca ratio patterns were interpreted point-by-point from the elver check to the otolith edge with 2-point smoothed averages, according to a threshold of 3 to 4×10^{-3} between fresh and brackish water bodies, shown as thin straight line. Small solid circles represent annuli. The first peak of Sr/Ca ratio before 100 μm corresponds to metamorphosis from leptocephalus to glass eel of Japanese eels (see Figs. 17 and 18). Amphidromous migratory patterns are predominantly observed (42%) during yellows eels stage among the studied 162 eels, followed by brackish (38%) and freshwater (20%) residence behavior [30].



Frequent movements between habitats, with no defined. A threshold between fresh and brackish water masses is of $3-4 \times 10^{-3}$. The Sr/Ca ratio peak observed before 100 μm corresponds to metamorphosis from *leptocephalus* to glass eel [30]. Sr distribution mapping for the six typical otoliths are shown in **Figure 20**. The core areas are surrounded by highest Sr content (red in color). Scale in each map: 200 μm .

(4) Different Sr/Ca patterns of European eels in the Baltic Sea area

Intensive stocking programs have been undertaken

in the Baltic Sea region over the past 50 years. The most intense stocking programs have been implemented in the Baltic Sea drainage using eels originating from Western Europe. The first eel stockings in Lithuania occurred between 1928 and 1939 when 3.2 million elvers were released into inland freshwater lakes of the Vilnius region (approx. 300 km from the Baltic coast). Since the mid 1960s, Lithuanian lakes have been stocked with approx. 50 million elvers or young yellow eels at an average stocking rate of 1.1 million eels yearly [31]. Studies on stocking effectiveness as well as studies on natural recruitment, however, have not been carried out and the post-stocking movements of stocked eels

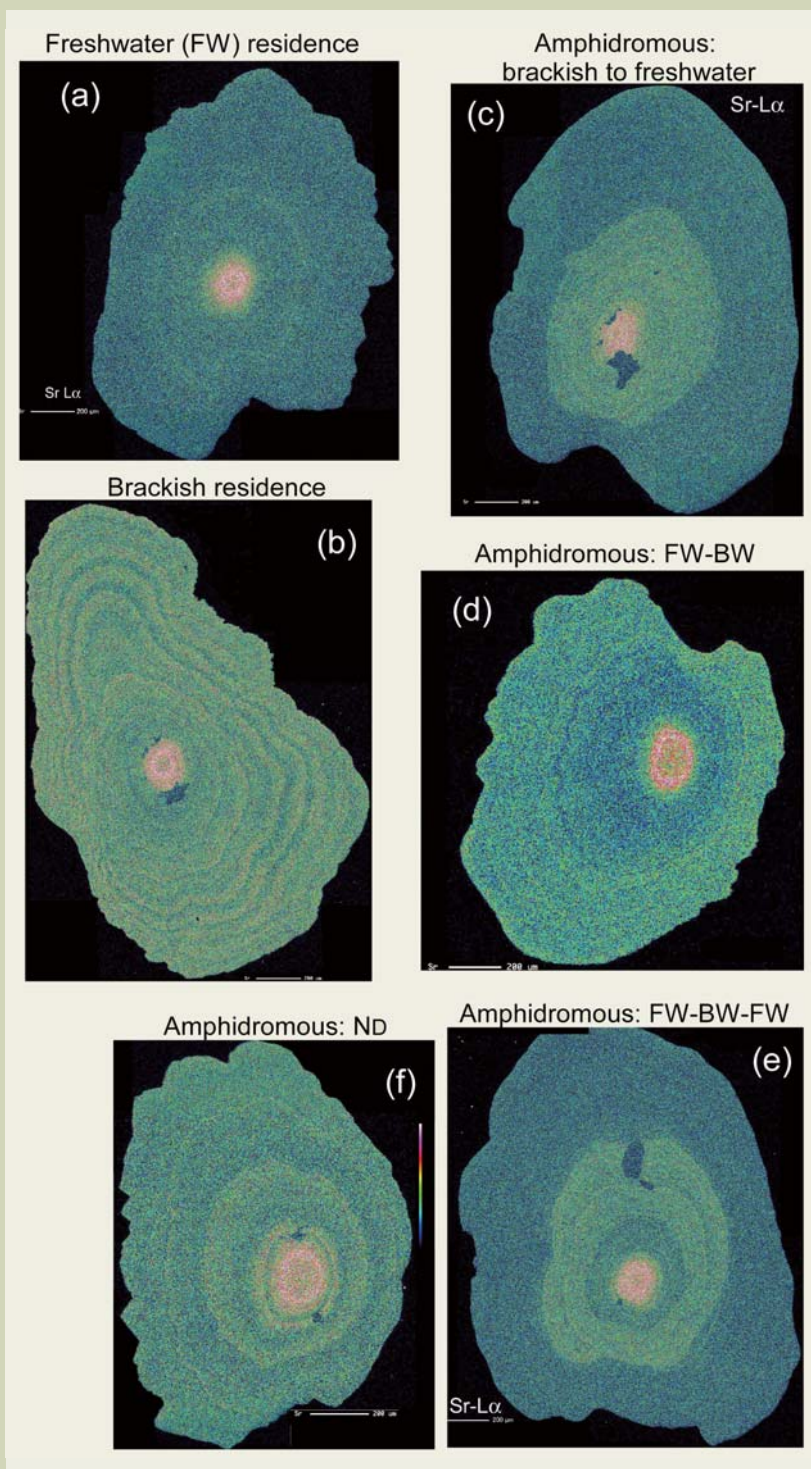


Fig. 20 Sr distribution of sagittal otoliths. Sr $L\alpha$ mapping were performed with TAP diffracting crystal at the condition of 15 kV and 80 nA for the acceleration voltage and beam current, respectively, with 1 μm defocused beam. X-ray intensities were counted for 0.040 sec at the interval of 1 μm . (a) Type-FR (IT-206: Fig. 19-a), (b) BR (IT-061: Fig. 19-b), (c) Type- A_{BF} (IT-285: Fig. 19-c), (d) Type- A_{FB} (IT-014: Fig. 19-d), (e) Type- A_{FBF} (IT-211: Fig. 19-e) and (f) Type- A_{ND} (IT-116: Fig. 19-f). Scale bar is 200 μm . Warm color (red) and cold color (blue) are indicate higher and lower concentration of Sr, respectively.

remain largely unknown because of the dissolution of the Soviet Union.

From a series of otolith study of European Eel *Anguilla anguilla* from Lithuanian water body, the Sr/Ca ratio transects along the otolith radius, from core to edge, illustrating 2 significant life-history patterns, multiple migration patterns were observed as well as Japanese and American eels though [32]. As shown in **Figure 21-a**, a solid line represents the mean \pm SD (standard deviation) otolith Sr/Ca ratio profile of 20 eels that showed a gradual decline pattern, indicating the movement from the full strength of salinity in the North Sea into brackish water of the Baltic Sea (Phase I: mean Sr/Ca ratio $5.51 \pm 1.57 \times 10^{-3}$) and ultimately arrived at the coastal waters of Lithuania (Phase II: mean Sr/Ca ratio $3.64 \pm 1.10 \times 10^{-3}$). And transition of freshwater and sea/brackish water residence is indicated as 2 to 3×10^3 in Sr/Ca ratio. An example which has been studied by Sr/Ca pattern and Sr mapping is shown in **Figure 22**. It is supposed one of typical pattern of the Baltic Sea migration. In **Figure 21-b**, on the other hand, the mean patterns indicate consistently low otolith Sr/Ca ratios ($0.72 \pm 0.76 \times 10^{-3}$) after the glass eel stage from 16 eels which were collected from freshwater lagoon and lake, the Curonian Lagoon (n=6) and Lake Baluošai (n=10). Since their patterns lack the Baltic Sea migration, it is concluded that these patterns are typical from restocked eels. The Sr/Ca patterns indicate the transition from sea/brackish water to freshwater, freshwater residences [32, 33, 43].

Conclusive remarks

Many interpretations of geographical and population genetic studies of fish suffer from uncertainty arising from artificial stocking or due to lack of information about the migrating behavior of species of interest. Successful

fish stock management, as well as conservation program are not effective without a complete understanding of the population genetic structure, stock boundaries and spatial and temporal migratory patterns. In recent years, advances in analytical techniques have led to the use of otolith microchemistry as an aid to stock discrimination in fishes. A contribution of EPMA technique based on geo- and mineral chemistry is remarkable. EPMA study of Sr/Ca ratios of otolith can interpret their migration and habit and are now one of most important data.

Genetic markers are widely used as implements for acknowledging potential stock differences. The recent developments of such investigation methods as the assay of microsatellites have provided us with the opportunity to evaluate relationships between populations and subpopulations. By combining two modern techniques; otolith microchemistry and microsatellite DNA analysis, we intend to demonstrate the effectiveness of such an approach to the diadromous fish stocks management [34]. The techniques will present an innovative approach to address the management-related problems and conservation of endangered species.

Acknowledgments

This series of otolith study was conducted with financial support from the Institute of Earth Sciences, Academia Sinica and the National Science Council of Taiwan. The author deeply appreciates Drs. Wann-Nian Tzeng, Jen-Chieh Shiao of National Taiwan University and Dr. Chih-Wei Chang of National Museum of Marine Biology & Aquarium (Taiwan) for their initiation of otolith analysis and discussion. I also thank Drs. Brian M. Jessop and David K. Cairns of Bedford Institute of Oceanography (Canada), Dr. Linas Ložys of Vilnius University (Lithuania), and Dr. Julian J. Dodson of Université Laval (Canada) for their long term collaborations.

Fig. 21 Comparison of mean value of Sr/Ca ratios of otolith of (a) naturally-recruited and (b) restocked eels from Lithuania water bodies [32]. The transition of freshwater and sea and brackish residence (■) is indicated. (a) The mean \pm S.D. (standard deviation: 1σ) otolith Sr/Ca ratio profile of 20 European eels that showed a gradual decline pattern, indicating the movement from the full strength of salinity in the North Sea into brackish water of the Baltic Sea (phase I: numbers of probe spots = 1240) and ultimately arrived at the coastal waters of Lithuania (phase II: n = 1119). (b) Transects of mean \pm S.D. otolith Sr/Ca ratios from 16 freshwater-resident eels, illustrating consistent low values after the glass eel stage.

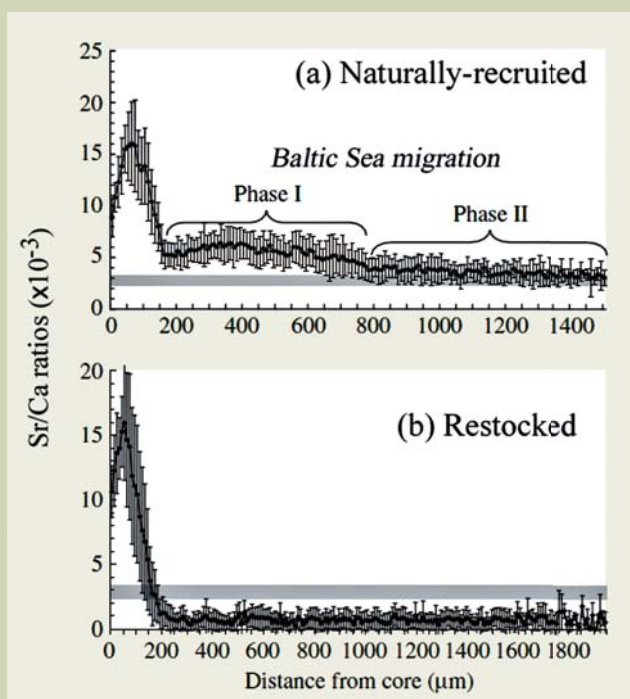
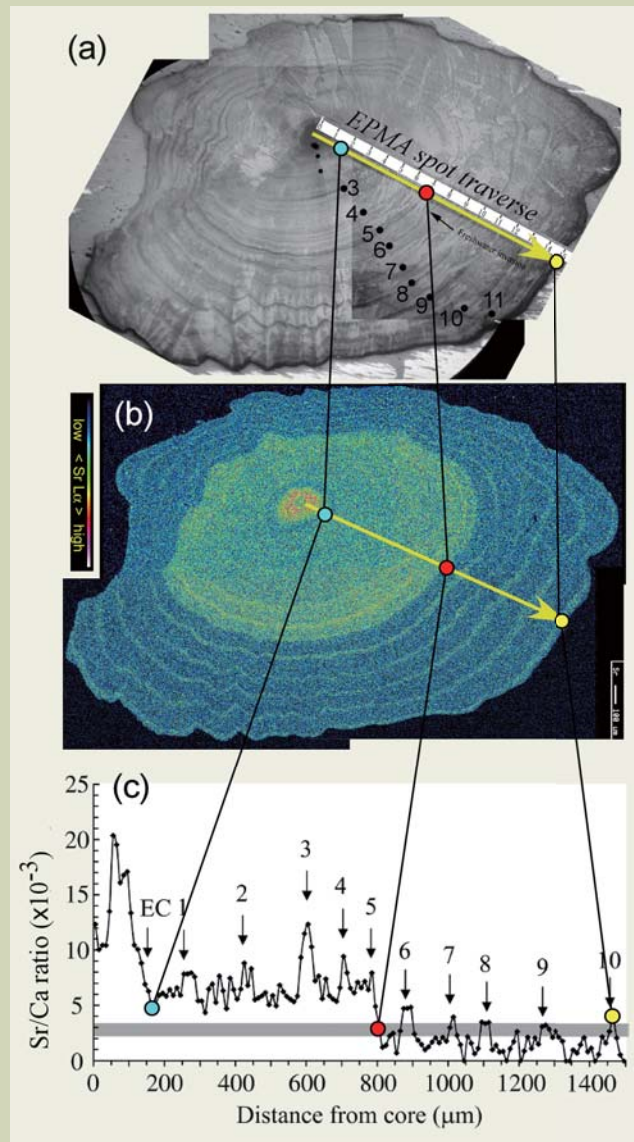


Fig. 22 Otolith Sr/Ca ratio from core to edge illustrates eel movement into fresh water after a period of seawater and brackish-water residence. (a) An optical micrograph of otolith of European Eel *Anguilla anguilla* (Lithuanian eel sampling code LT-1, age 11 years old), collected from the Curonian Lagoon in Lithuania (Lat. 56° N). Dots and numbers represent annual increments and estimated ages, respectively. A track of EPMA quantitative transecting analysis from the primordium (core) to edge is shown as a yellow arrow. (b) Sr distribution mapping displays higher Sr content (green in color) from age 1 to 5 years and high Sr rings at annuli 6–10 between age 6 and 11 years (light blue in color) which is assumed as winter marks. The Primordium (core) area is surrounded by highest Sr content (orange in color) and a yellow arrow shows direction of quantitative transecting analysis (c) An example of the Baltic migration pattern Sr/Ca ratios transect along the otolith radius, from core to edge with 10 μm interval. A freshwater entry (a red circle) is observed the age between 5 and 6 years old. Seasonal migration between high salinity (a yellow circle) and low salinity or fresh waters is also observed after the freshwater entry. #1–10: the annuli corresponding to peaks in the otolith Sr/Ca ratios; EC: elver check (a blue circle). The transition of freshwater and sea/brackish residence (■) is indicated [32].



References

- [1] Campana SE (1999) Chemistry and composition of fish otoliths: pathways, mechanisms and applications. *Mar Ecol Prog Ser* **188**: 263-297.
- [2] Carlstrom D (1963) A crystallographic study of vertebrate otoliths. *Biol Bull* **125**: 441-463.
- [3] Degens ET, WG Deuser, RL Haedrich (1969) Molecular structure and composition of fish otolith. *Mar Biol* **2**: 105-113.
- [4] Amiel AJ, GM Friedman, DS Miller (1973) Distribution and nature of incorporation of trace elements in modern aragonite corals. *Sedimentology* **20**: 47-64.
- [5] Tzeng WN (1996) Effects of salinity and ontogenetic movements on strontium:calcium ratios in the otoliths of the Japanese eel, *Anguilla japonica*. *J Exp Mar Bio Ecol* **199**: 111-122.
- [6] Radtke RL (1989) Strontium-calcium concentration ratios in fish otoliths as environmental indicators. *Comp Biochem Physiol* **92A**: 189-193.
- [7] Otake T, T Ishii, M Nakahara, R Nakamura (1994) Drastic changes in otolith strontium/calcium ratios in leptocephali and glass eels of Japanese eel *Anguilla japonica*. *Mar Ecol Prog Ser* **112**: 189-193.
- [8] Tzeng WN, YC Tsai (1994) Changes in otolith microchemistry of the Japanese eel, *Anguilla japonica*, during its migration from the ocean to the rivers of Taiwan. *J Fish Biol* **45**: 671-683
- [9] Arai T, T Otake, K Tsukamoto (1997) Drastic changes in otolith microstructure and microchemistry accompanying the onset of metamorphosis in the Japanese eel *Anguilla japonica*. *Mar Eco Prog Ser* **161**: 17-22.
- [10] Thorrold Sr, CM Jones, SE Campana (1997) Response of otolith microchemistry to environmental variations experienced by larval and juvenile Atlantic croaker (*Micropogonias undulatus*). *Limnol Oceanogr* **42**:102-111
- [11] Kawakami Y, N Mochioka, K Morishita, T Tajima, H Nakagawa, H Toh, A Nakazono (1998) Factors influencing otolith strontium/calcium ratios in *Anguilla japonica* elvers. *Environ Biol Fish* **52**: 299-303.
- [12] Tsukamoto K, I Nakai, WV Tesch (1998) Do all freshwater eels migrate? *Nature* **396**: 635-636.

- [13] Tzeng WN, KP Severin, H Wickström (1997) Use of otolith microchemistry to investigate the environmental history of European eel *Anguilla anguilla*. *Mar Ecol Prog Ser* **149**: 73-81.
- [14] Shiao JC, Y Iizuka, CW Chang, WN Tzeng (2003) Disparities in habitat use and migratory behavior between tropical eel *Anguilla marmorata* and temperate eel *A. japonica* in four Taiwanese rivers. *Mar Ecol Prog Ser* **261**: 233-242.
- [15] Gunn JS, IR Harrowfield, CH Proctor, RE Thresher (1992) Electron probe microanalysis of fish otoliths - evaluation of technique for studying age and stock discrimination. *J Exp Mar Biol Ecol* **158**: 1-36.
- [16] Sadovy Y, KP Severin (1992) Trace elements in biogenic aragonite: Correlation of body growth and strontium levels in the otoliths of the white grunt, *Haemulon plumieri* (Pisces. Haemulidae). *Bull Mar Sci* **50**: 237-257.
- [17] Toole CL, RL Nielsen (1992) Effects of microprobe precision on hypotheses related to otolith Sr:Ca ratios. *Fish Bull US* **90**: 421-427.
- [18] Philibert J, R Tixier (1968) Electron penetration and the atomic number correction in electron probe microanalysis. *Brit J Appl Phys* **2(1)**: 685-694.
- [19] Reed SJB (1993) Electron Microprobe Analysis (2nd Ed.). Cambridge University Press, Cambridge.
- [20] Potts PJ (1987) A handbook of silicate rock analysis. Blackie, New York.
- [21] Jarosewich E (2002) Smithsonian Microbeam Standards, *J. Res. Natl. Inst. Stand. Technol.* **107**, 681-685.
- [22] Jarosewich E, IG MacIntyre (1983) Carbonate reference samples for electron microprobe and scanning electron microscope analyses. *J. Sedimentary Petrol* **52**:677-678.
- [23] Jarosewich E, JS White (1987) Strontianite reference samples for electron microprobe and SEM analyses. *J. Sedimentary Petrol* **57**:762-763.
- [24] Casting R (1951) Application des sondes électroniques a une method d'analyse ponctuelle chimique et cristallographique. PhD thesis, University of Paris.
- [25] Weast RC (editor-in-chief) (1973) Handbook of chemistry and physics (54th edn.). Chemical Rubber Company Press, Cleveland.
- [26] Tsukamoto K (1992) Discovery of the spawning area for Japanese eel. *Nature* **356**: 789-791.
- [27] Tsukamoto K with 18 coauthors (2011) Oceanic spawning ecology of freshwater eels in the western North Pacific, *Nature Communications* **2**, Article number: 179, doi:10.1038/ncomms1174, www.nature.com/ncomms/journal/v2/n2/full/ncomms1174.html
- [28] Tzeng WN, JC Shiao, Y Iizuka (2002) Use of otolith Sr : Ca ratios to study the riverine migratory behaviors of Japanese eel *Anguilla japonica*. *Mar Ecol Prog Ser* **245**:213-221.
- [29] Tzeng WN, Y Iizuka, JC Shiao, Y Yamada, H Oka (2003). Identification and growth rates comparison of divergent migratory contingents of Japanese eel (*Anguilla japonica*). *Aquaculture*. **216**:77-86.
- [30] Thibault I, JJ Dodson, F Caron, WN Tzeng, Y Iizuka, JC Shiao (2007) Eels facultative catadromy: a conditional strategy? Facultative catadromy in American eels: testing the conditional strategy hypothesis. *Mar Ecol Prog Ser* **344**:219-229.
- [31] Ložys L (2002) Monitoring of glass eel recruitment in Lithuania. In Monitoring of Glass Eel Recruitment (Dekker, W., ed.), pp.87-96. Ijmuiden: Netherlands Institute of Fisheries Research.
- [32] Shiao JC, L Ložys, Y Iizuka, WN Tzeng (2006) Migratory patterns and contribution of stocking to the population of European eel in Lithuanian waters as indicated by otolith Sr:Ca ratios. *J Fish Biol.* **69**:749-769.
- [33] Lin YJ, L Ložys, JC Shiao, Y Iizuka, WN Tzeng (2007) Growth differences between naturally recruited and stocked European eel *Anguilla anguilla* in Lithuania. *J Fish Biol*, **71**:1773-1787.
- [34] Han YS (2012) Wide geographic distribution with little population genetic differentiation: a case study of the Japanese eel *Anguilla japonica*. In Eels: Physiology, Habitat and Conservation (Chapter 7), Eds. S Nakashima and M Fujimoto, pp.149-164. Nova Science Publishers, Hauppauge, USA.
- [35] Daverat F, KE Limburg, I Thibault, JC Shiao, JJ Dodson, F Caron, WN Tzeng, Y Iizuka, H Wickström (2006) Phenotypic plasticity of habitat use by three temperate eel species *Anguilla anguilla*, *A. japonica* and *A. rostrata*. *Mar Eco Prog Ser* **308**: 231-241.
- [36] Jessop BM, JC Shiao, Y Iizuka, WN Tzeng (2002) Migratory behaviour and habitat use by American eels *Anguilla rostrata* as revealed by otolith microchemistry. *Mar Eco Prog Ser*, **233**:217-229.
- [37] Jessop BM, JC Shiao, Y Iizuka, WN Tzeng (2006) Migration of juvenile American eels *Anguilla rostrata* between freshwater and estuary, as revealed by otolith microchemistry. *Mar Eco Prog Ser*, **310**:219-233.
- [38] Lamson HM, JC Shiao, Y Iizuka, WN Tzeng, DK Cairns (2006) Movement patterns of American eels (*Anguilla rostrata*) between salt and fresh water in a coastal watershed, based on otolith microchemistry. *Marine Biology*, **149**:1567-1576.
- [39] Jessop BM, JC Shiao, Y Iizuka, WN Tzeng (2007) Effects of inter-habitat migration on the evaluation of growth rate and habitat residence of American eels *Anguilla rostrata*. *Mar Eco Prog Ser*, **342**:255-263.
- [40] Jessop BM, JC Shiao, Y Iizuka (2009) Life history of American eels from Western Newfoundland. *Trans Am Fish Soc*, **138**:861-871.
- [41] Lamson HM, DK Cairns, JC Shiao, Y Iizuka, WN Tzeng (2009) American eel, *Anguilla rostrata*, growth in fresh and salt water: implications for conservation and aquaculture. *Fishes Manag Ecol*, **16**:306-314.
- [42] Tzeng WN, CH Wang, H Wickström, M Reizenstein (2000) Occurrence of the semi-catadromous European eel *Anguilla anguilla* in the Baltic Sea. *Mar Biol*. 137:93-98.
- [43] Lin YJ, JC Shiao, L Ložys, M Plikshs, A Minde, Y Iizuka, I Rashal, WN Tzeng (2009) Do otolith annular structures correspond to the first freshwater entry for yellow European eels *Anguilla anguilla* in the Baltic countries? *J Fish Biol*, **75**:2709-2722.
- [44] Lin YJ, JC Shiao, M Plikshs, A Minde, Y Iizuka, I Rashal, WN Tzeng (2011) Otolith Sr:Ca Ratios as Natural Mark to Discriminate the Restocked and Naturally Recruited European Eels in Latvia Proceedings of American Fisheries Society Symposium **76**:1-14.

Realization of an Innovative Metrological Traceability Using the Quantitative NMR Method

Toshihide Ihara and Takeshi Saito

National Metrology Institute of Japan, National Institute of Advanced Industrial Science and Technology

Reference materials are indispensable for accurate analysis of hazardous substances in food and environment. For organic substances, however, the dissemination of reference materials is hopelessly unable to catch up with today's rapidly proliferating analytical needs. To solve this problem, analytical techniques were improved to develop a method in which a single primary reference material could provide accurate quantitative measurements for a wide variety of organic compounds. In this approach, we turned our attention to the ^1H NMR method. We improved the method to perform precise comparisons of signal quantities from protons at different chemical shifts, enabling quantitative analysis at an acceptable level of uncertainty for a variety of organic reference materials by using a primary reference material for protons. Based on this achievement, an innovative metrological traceability capable of minimizing the number of national reference materials was realized, thus enabling us to have a prospect for rapid expansion of reference materials used in food and environmental analyses.

Introduction

Our modern lives are surrounded by chemical compounds, and a wide range of laws and regulations controls these chemical compounds, to ensure safety and to prevent adverse impact on the environment and human health. In recent years, public concern for safety has increased in Japan, prompting an increase in the number of chemical compounds subject to regulation, limitations, and other regulatory controls. For example, in May 2006, the Food Sanitation Law was revised to introduce the "positive list system^{Term 1}" for agricultural chemical residue in foods. With the enforcement of stringent regulations in Japan, the number of control subjects expanded from approximately 250 to about 800 kinds of agricultural and other chemical compounds traded domestically and internationally. At the same time, several new official methods^{Term 2} of analysis were established to measure the regulated chemical compounds, and as a result, the use of advanced analytical equipment capable of conducting multiple simultaneous measurements, such as gas chromatograph/mass spectrometer (GC/MS) and liquid chromatograph/mass spectrometer (LC/MS), increased in food and environmental analyses. In this situation, many laboratories that inspect and test chemical compounds are increasingly employing GC/MS and LC/MS to conduct analyses.

While these analytical equipment are capable of simultaneously measuring multiple components, it is

necessary to calibrate the sensitivity of the analytical instrument for each analyte in the samples to ensure the reliability of analytical results. To perform this calibration, reference materials (RMs) that serve as "yardstick" are required for individual analytes. In this type of analysis, the accuracy of inspection and testing results are crucial, and the reliability of the "yardstick" is of paramount importance. The use of certified reference materials (CRMs)^{Term 3} [1], or equivalent RMs are highly recommended in such cases, and therefore various testing and inspection laboratories are working swiftly to acquire the RMs necessary to handle the ever-increasing list of regulated materials.

Current problems with RMs

The characterization of RMs by metrologically appropriate procedures is achieved by using measurement methods that offer metrological traceability^{Term 4} to SI definitions (in this case, amount-of-substance). Normally, this is a task performed by the national metrology institute^{Term 5} of a country, and the RMs produced are known as the national reference materials (primary RMs). Generally, national RMs offer the highest standards of accuracy, and are scrupulously prepared with labor, time, and expense. Normally, they are not transferred directly to the inspection and testing laboratories that perform the actual analysis, because this is not practical due to the quantities and costs involved. Instead, secondary RMs are characterized based on the national RMs, and working RMs are in turn characterized using the secondary RMs. In this way, a

Central 3, 1-1-1 Umezono, Tsukuba Ibaraki 305-8563, Japan

E-mail: t.ihara@aist.go.jp

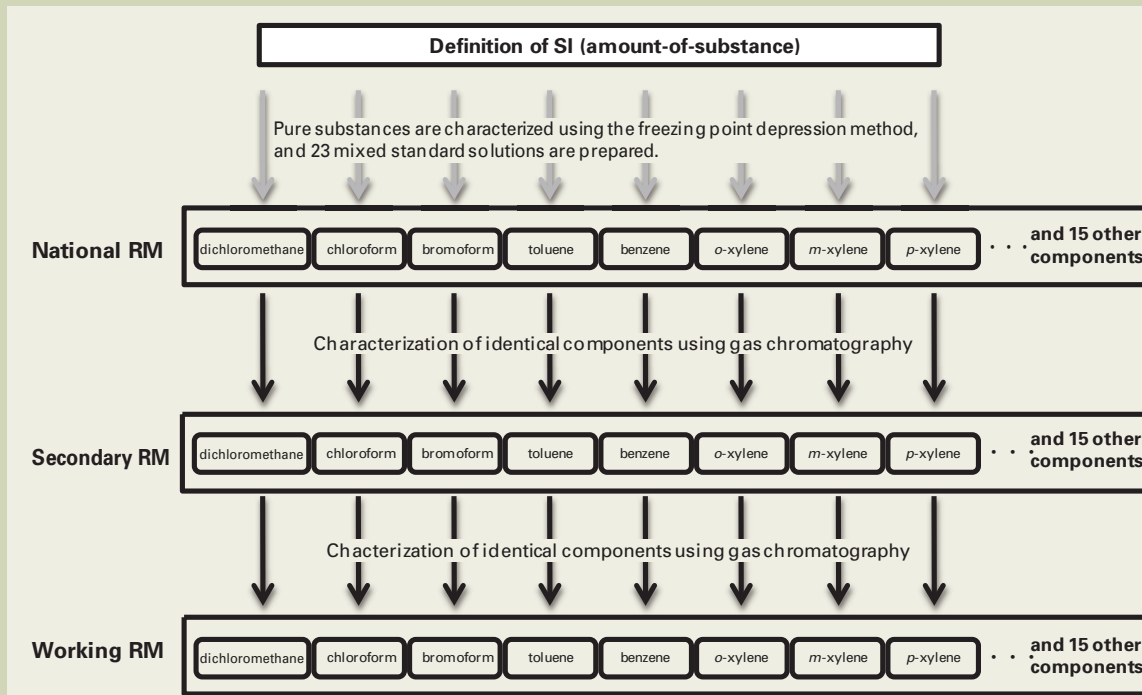


Fig. 1 Metrological traceability system for RMs used in analysis of volatile organic compounds.

pyramid structure is constructed, with a few higher-order RMs at the top and a larger population of lower-order RMs reproduced below. The order in this proliferation of RMs is enforced through metrological traceability to the original set of accurate “yardstick” or the national RMs.

Figure 1 is a schematic diagram of the metrological traceability system for the RMs used in the analysis of volatile organic compounds that are used to test the quality of river and tap water. The national RM is in the form of a single solution incorporating 23 volatile compounds. Metrological traceability to SI is obtained using pure substances for each component that is valued using the freezing point depression method. The secondary and working RMs also consist of a single solution incorporating 23 volatile organic compounds, but in this case, characterization from upper-order to lower-order standards is conducted separately for each component. Because the lower-order metrological traceability system requires a one-to-one correspondence, the pyramid structure breaks down for these RMs. In other words, the national RM for a given component must be used to characterize the secondary RM for the same component, and characterization of working RMs for the same component is performed using this secondary RM. Because this is one-to-one comparison of the same chemical compounds, commercially available analytical technologies such as gas chromatography can be used for characterization down to the working RM level while maintaining excellent reliability. This practical system of metrological traceability is used throughout the world.

The drawback of this metrological traceability system is that it requires a wide array of national RMs to match each chemical compound subject to be analyzed. Development of these national RMs is a major bottleneck in the metrological traceability system because it requires enormous time, labor, and expense. The construction of a more efficient metrological traceability system based on

an entirely new concept is needed to address the rapidly proliferating demand for RMs prompted by increasingly tight regulation of chemical compounds through the positive list system discussed above.

Research target

To recapitulate the previous section, the problem with present metrological traceability system for RMs lies in the dependence on national RMs. Because the system consists of the series of “characterization chains” for the same chemical compound, the system cannot respond promptly to the need for RMs to analyze the growing number of chemical compounds. Although this problem can be solved if minimum types of higher-order RMs could be used to calibrate a wide range of working RMs, this is not possible with current analytical technologies, which are designed to calibrate a like chemical compound with a like chemical compound. An entirely new analytical technology must be developed and introduced: a universal analytical technology capable of analyzing chemical compounds independently of their molecular structure.

The aim of this study is to develop a new analytical technology to realize a system that efficiently secures metrological traceability to the wide range of working RMs without creating national RMs for each chemical compound. Given that the vast majority of chemical compounds subject to strengthened regulation in recent years are organic compounds, we developed a universal analytical technology targeting organic compounds.

The required analytical technology

Absolute values for amount-of-substance can be obtained using SI-traceable measurements. This type of measurement is known as the primary method of

measurement^{Term 6}. **Table 1** shows a list of analytical methods certified as primary methods of measurement, divided into primary direct methods and primary ratio methods. The primary direct methods, also called the absolute measurement methods, are defined as “the methods for measuring the value of an unknown without reference to a standard of the same quantity.” Examples of primary direct methods are coulometry, gravimetry, and the freezing point depression method. Because these analytical methods yield absolute values for amount-of-substance, they are appropriate for valuating the national RMs. However, in general, they tend to be slow and their applications are limited to short list of substances, and they are not suitable candidates as universal analytical technology that is the objective of this study. Primary ratio methods, on the other hand, are already in practical use. They are defined as “methods for measuring the value of a ratio of an unknown to a standard of the same quantity; its operation must be completely described by a measurement equation.” They include titrimetry and isotope dilution mass spectrometry. Another analytical approach that qualifies as a primary ratio method, though not well established as an analytical technology, is the quantitative nuclear magnetic resonance (quantitative NMR).

A measurement method that can be applied to the characterization of a wide range of working RMs must satisfy the following conditions:

- 1) It must satisfy market demands regarding uncertainty, while also provide speed and simplicity of use.
- 2) It must be highly versatile and applicable to a wide variety of chemical compounds (general organic compounds for the purposes of this study).

Quantitative NMR is the most feasible candidate that can satisfy both conditions 1) and 2), although the answer is not yet fully established. Accordingly, in this study, we endeavored to establish quantitative NMR as a universal analytical technology for working RMs in organic compounds.

Principles of quantitative NMR

NMR is one of the main methods for determining the molecular structure of a chemical compound. It has an extensive track record in unraveling molecular structures, including the analysis of complex molecules such as proteins. Information obtained using NMR, such as chemical shift (the resonance peak position dependent on atomic bonding and the ambient environment) and spin-spin coupling (a split of the peak due to bonded nearby nuclei), provides hints about the chemical species and ambient environment of a molecule. In addition, the area ratio of various peaks, which resonate according to different chemical shifts, generally indicates the ratio of the number of atomic nuclei contributing to the peaks. As **Figure 2** shows, the area ratio of ¹H NMR signals can easily be used to confirm the relative number of protons for the resonances, which is vital for the qualitative analysis of organic compounds.

Conventionally, this aspect of NMR was used exclusively to determine the chemical structure, solely by expressing the number of protons as a ratio in a molecule. However, the concept can be applied differently. If the molecular structure of an organic compound is already known and assignments of its ¹H NMR spectrum has been set, the number of protons contributing to each resonance peak is known, and this information can be applied to the quantitative analysis of chemical compounds. Thus,

when the ¹H NMR measurement is performed by adding a reference chemical compound to a sample solution separately in an analyte solution, the spectra of the two chemical compounds overlay each other, as shown in **Figure 3**. At this point, if the mass (weight), molecular weight, and purity of the added reference chemical compound (hereinafter, will be called the Primary Standard: PS) are known, the amount-of-substance (number of molecules) corresponding to peak I in **Figure 3** will also be known, and can be used as the criterion for finding the number of molecules in the analyte. To illustrate with a specific example, if the number of protons in PS (I) is the same as the number of protons in analyte (D) (the number is 6 for both), the ratio of the areas for peak I and peak D indicates the relative number of molecules. As such, the relationship can be expressed as follows:

$$\begin{aligned} & \text{(Peak area I)} / \text{(Number of molecules of PS)} \\ & = \text{(Peak area of D)} / \text{(Number of molecules in analyte)} \end{aligned}$$

Since the number of molecules in PS is already known, the number of molecules in the analyte can be obtained. The mass (weight) and molecular weight of the target substance can then be used to determine the purity of the analyte [2]. Therefore, quantitative NMR is, in principle, a primary ratio method which can be used to obtain traceable measurement values for the number of protons — that is, amounts of substance in a sample.

In the example in **Figure 3**, both the analyte and the PS are pure substances. After weighing the two substances individually, they are dissolved in a deuterated solvent, and quantitative NMR is used to measure the purity of the analyte using the mass ratio of the two substances. Working RMs, in contrast, are often supplied in the form of solution. If supplied at a certain concentration (about 0.1 %), quantitative NMR can be applied by dissolving the working RM in an appropriate deuterated solvent. The concentration of working RM can be found from the number of molecules obtained for the analyte, the mass of sample solution added, and the number of molecules in the analyte.

Feasibility of quantitative NMR

National metrology institutes in several countries (including AIST), which are members of the Consultative Committee for Amount of Substance (CCQM)^{Term 7}, have shown interest in the possibility of applying quantitative NMR as a primary ratio method, which was first suggested by Germany's Federal Institute for Material Research and Testing (BAM). In 2001, the Laboratory of the Government Chemist (LGC) in the United Kingdom and BAM served as pilot laboratories to conduct an international comparison^{Term 8} for the quantitative analysis of ethanol in aqueous solution, with the participation by 10 institutes in key countries. On this occasion, measurements were conducted on the same sample using conventional analytical approaches such as gas chromatography (GC) as well as quantitative NMR [3]. The sample was precisely produced by LGC, one of the pilot laboratories. The ethanol concentration was 1.072 mg/g ± 0.006 mg/g, but this value was not disclosed to the participants. Also, BAM separately supplied a deuterated water solution of PS (3-trimethylsilyl sodium propionate-*d*₄) of known concentration to the participating institutions that declared to conduct the quantitative NMR measurement.

Table 1 Types of primary methods of measurement and their characteristics.

Analytical method	Primary direct method			Primary ratio method		
	Coulometry	Gravimetry	Freezing point depression method	Titrimetry	Isotope dilution mass spectrometry	Quantitative NMR
Outline of analytical method	Amount of electricity used in electrolysis of specified substances is measured.	Settling quantity of specified substances in solution is measured.	Relationship between fraction melted and temperature around the melting point is measured.	Specified substance is measured using chemical reactions.	Mass spectrometry is performed using a stable isotope.	Ratio of areas of ^1H peaks with different chemical shifts is measured.
Main target substance	Metallic elements	Inorganic salts	High purity organic compounds	Acid, base, elements	Trace metals trace organic compounds	Organic compounds
Reference standard	Not required	Not required	Not required	Reference standards based on the principles of titration are required.	Required for each analyte	A reference standard for ^1H is required.
Uncertainty (less than 1%)	○	○	○	○	○	△ (Unknown value)
Swiftness	×	×	×	×	○	○
General applicability	×	×	×	×	×	○

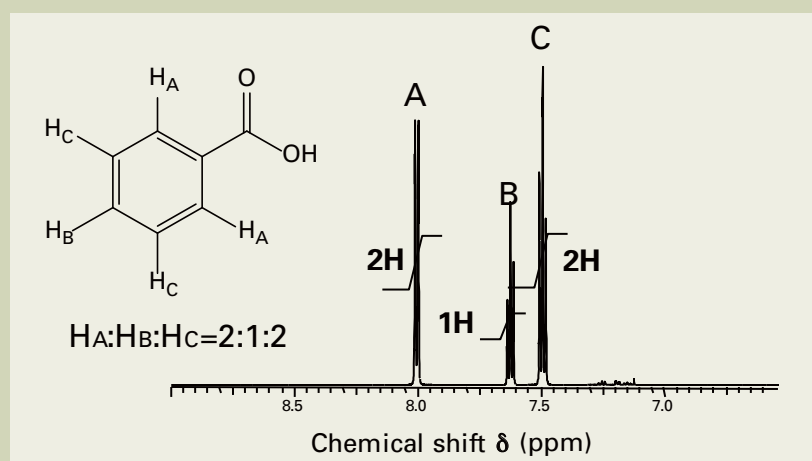


Fig. 2 Qualitative analysis of chemical compounds using ^1H NMR.

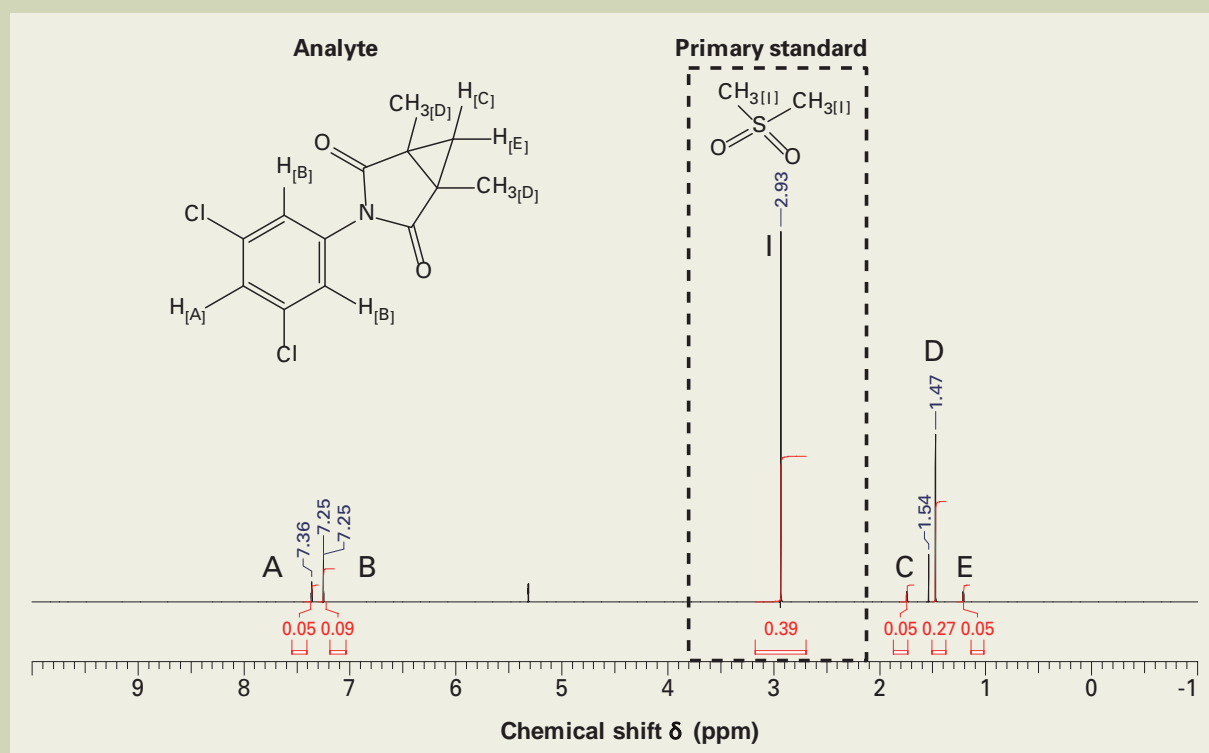


Fig. 3 Quantitative analysis of chemical compounds using ^1H NMR.

The measurement results were reported individually to the pilot laboratory. **Figure 4** is a summary of the results. Each data point represents a reported result. The adjacent error bar is the measurement uncertainty estimated by each participating institution (95 % confidence interval). The uncertainty of the quantitative NMR results from most institutions was in the range that could be described as percentage, and some of the results deviated significantly from the preparation values. In short, it was found that the quantitative NMR lacked accuracy compared to the conventional analytical methods such as GC. From the result of this international comparison, it was determined that the quantitative NMR did not offer sufficient technical accuracy. This view remains essentially unchallenged in the international scientific community today.

At the same time, **Figure 4** shows that the value reported by AIST closely matched the preparation value and its uncertainty was considerably smaller than the quantitative NMR findings of other participating institutions. This is why AIST takes a different stance on quantitative NMR. The uncertainty AIST reported to the pilot laboratory for quantitative NMR in the international comparison is illustrated in **Figure 5**. Upon evaluating the relative standard uncertainties of each component, we found that the greatest factor was the uncertainty of the concentration of ^1H PS supplied by the pilot laboratory. Because the uncertainty of AIST's quantitative NMR measurement was much smaller, it became clear that a much smaller measurement uncertainty would have resulted if AIST had supplied its own more accurate PS.

It should be emphasized that the quantitative NMR offers a major advance in versatility. Whereas GC and other conventional analytical technologies applied in the international comparison can only be used to compare the concentrations of like chemical compounds (PS must be the same chemical compound as the measured substance), quantitative NMR can compare quantities of chemical compounds of different types (that is, PS does not have to be the same type of chemical compound as the measured substance). As such, although quantitative NMR requires at least one substance including ^1H , it can be used to measure any organic compound that includes proton, and a wide range of applications can be expected accordingly. The Authors believe that quantitative NMR can be applied in the characterization of working RMs by developing and integrating certain elemental technologies. These are discussed below.

Elemental technologies to realize the quantitative NMR

Figure 6 illustrates the elemental technologies developed by the authors, and the combination necessary to realize the potential of quantitative NMR as a universal analytical technology for working RMs. The features required of NMR differ greatly depending on whether the technology is optimized for qualitative analysis or for quantitative analysis, as in our case. With quantitative NMR, the highest priority is to observe the signal in accurate proportion to the number of atomic nuclei in the analysis, rather than improving measurement speed or improving the signal-to-noise ratio (S/N). We therefore revised the conditions for selecting the core elemental technologies.

The first elemental technology corrects a signal

amplification issue. Generally speaking, NMR signals relax throughout its lifetime called the spin lattice relaxation time (T_1), which is the time taken for the atomic nuclei to settle from their excited state to their ground state. This period varies according to the environment of protons (such as bonding with other atoms). When NMR is performed for qualitative analysis, the sample is irradiated with radio frequency pulses with short cycle to increase the signal and to improve S/N. In such case, the delay time may be shorter than T_1 , where excitation pulse is applied before all protons settled to their ground state. As a result, differences in T_1 among the protons of analyte and PS make it impossible to obtain the peak area in correct proportion for the number of protons in each proton. We resolved this problem by measuring the relationship between repetition time and peak area. By taking delay time six times or greater than T_1 for the analyzed protons, it was demonstrated by experiment that 99.9 % or more of original signal intensity could be obtained, providing a stable peak-area ratio [4]. By ensuring that the delay time was sufficiently longer than the longest T_1 for all protons in the analyte, it was possible to obtain accurate peak-area ratio that was unaffected by the T_1 of the protons (though the measurement time increased several times longer than the conventional method).

Normally in NMR measurement, an audio filter is used to narrow a measured bandwidth to improve S/N. However, since the audio filter does not show a flat sensitivity characteristic over the whole range of the bandwidth, the sensitivity significantly decreases especially at the edges of the filter bandwidth. Depending on the chemical shift, a few percent or more decrease in sensitivity occurs. Thus, to obtain a flat sensitivity unaffected by the chemical shift, it is necessary to pay attention to the filter characteristics. In an NMR instrument equipped with a digital filter, signals passed through a wide-bandwidth audio filter are subject to further digital filtering, thus it is better to understand this point. On the other hand, in the case of an NMR instrument not equipped with a digital filter, a decrease in signal intensity occurs at an observation bandwidth of 10 ppm to 20 ppm set for qualitative NMR spectroscopy. As a result, as the chemical shift of the protons of analyte and PS is deviated further from the spectral center, it is difficult to obtain an accurate peak area. The authors therefore expanded the observation bandwidth to about 100 ppm to set a wide-bandwidth filter, enabling us to use a sufficiently flat filter characteristics for the range where ^1H NMR signals exist (normally, 0 ppm to 10 ppm), leading to the acquisition of a flat sensitivity that we expected even from an NMR instrument not equipped with a digital filter. Such filter setting requires loading of a large amount of data, and therefore this setting is not used in normal NMR measurement. However with quantitative NMR, the highest priority is to obtain accurate measurement values. Thus, an approach that breaks through conventional methods was adopted and this problem was successfully solved [4].

In addition to the two elemental technologies described above, the Authors found that to improve the reproducibility of measurement results, phase correction, baseline correction, and peak area integration setting (range) were more important compared to other minor factors.

Use of transfer materials

Although quantitative NMR requires ^1H as the PS, the analyte (substance to be analyzed) does not have to be the

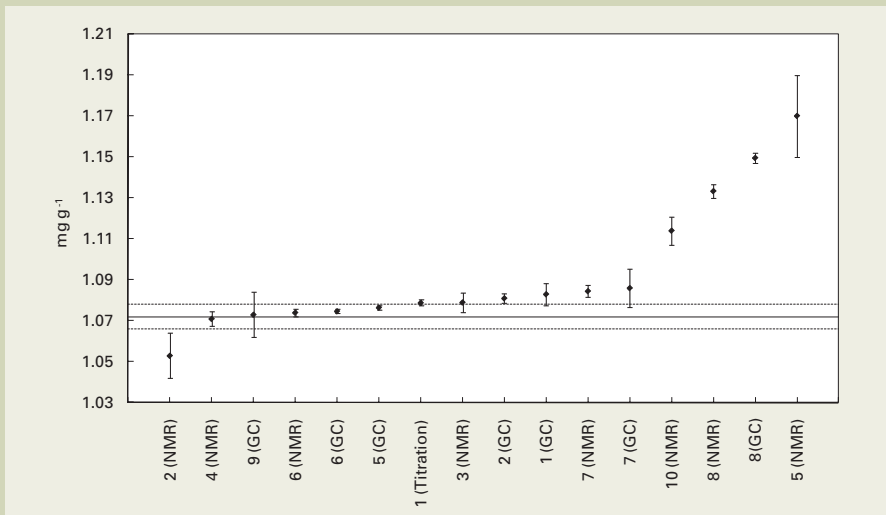


Fig. 4 Results of international comparison on quantitative analysis of ethanol in aqueous solution. The solid line indicates the preparation value; the dotted line indicates uncertainty for the preparation value. No. 6 is the result for NMIJ/AIST. Participants: BAM (Germany), KRISS (China), LGC (UK), LNE (France), NIST (USA), NMI (Netherlands), NMIJ (Japan), NRC (Canada), NRCCRM (China) and VNIM (Russia).

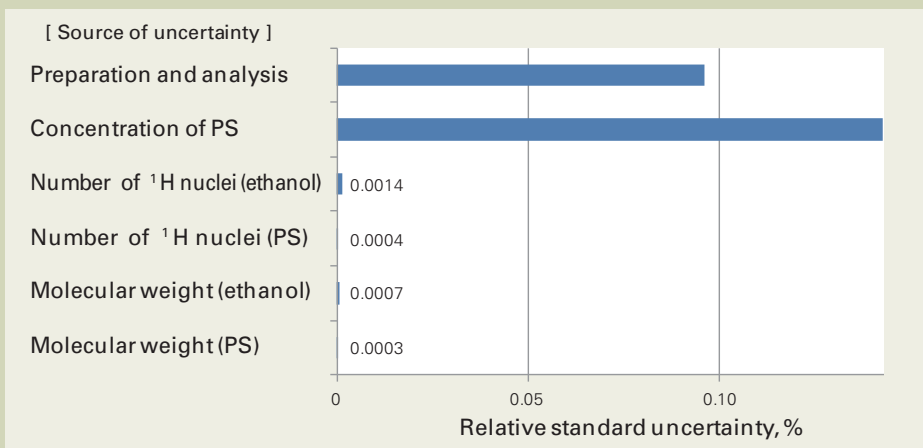


Fig. 5 Uncertainty for ¹H NMR in the international comparison on quantitative analysis of ethanol in aqueous solution.

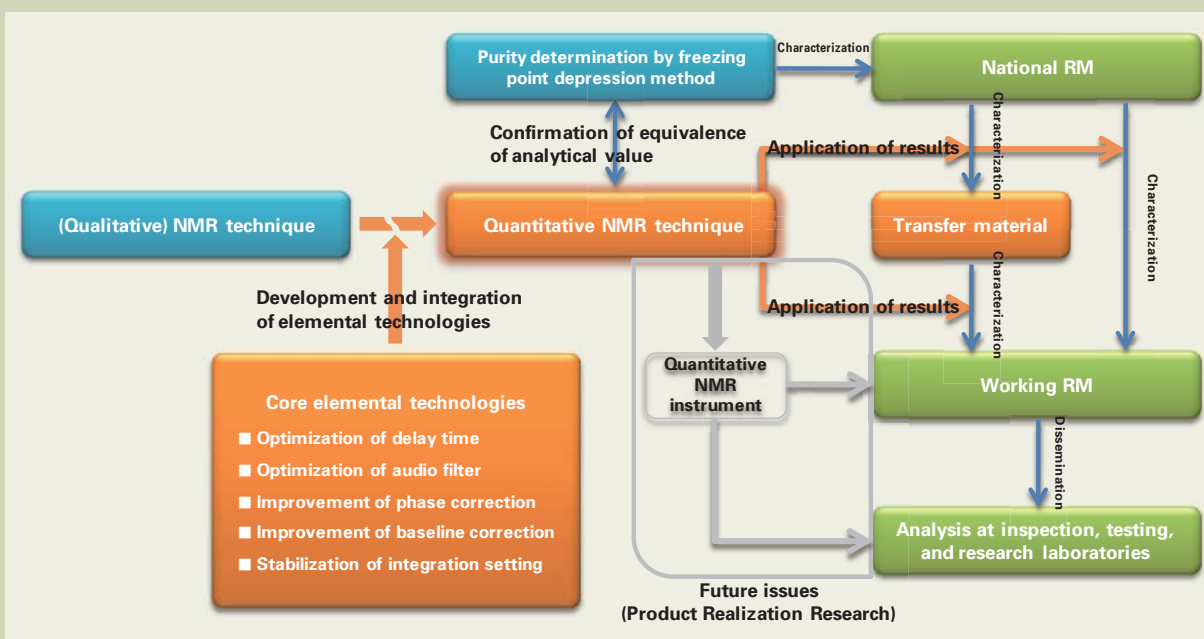


Fig. 6 Development of elemental technologies for the construction of universal analytical technology and the process of integration.

same substance. The PS (limited to pure substances in this discussion) must satisfy the following conditions:

- 1) It must have as little impurities as possible, to keep the uncertainty for its purity value small.
- 2) It must dissolve easily in wide range of solvents, and must be stable in solution.
- 3) It must have low volatility (sublimability) and absorbency, so its mass (weight) can be measured easily.
- 4) Its chemical shift must not overlap with that of the target substance.

Although some national RMs satisfy these conditions for PS, many national RMs do not satisfy requirement 2), because a suitable solvent for dissolving both the PS and the analyte has not been found. Also, some national RMs do not satisfy 4), as the PS used depends on the analyte, and different PSs must be used with certain analytes.

The number of national RMs cannot be reduced if different PSs must be prepared according to various analytes. The Authors solved this problem using the analytical methods illustrated in **Figure 7**, utilizing the advantages of quantitative NMR. We achieved this by selecting the transfer materials or chemical compounds whose chemical shifts do not overlap with either the PSs or the analytes [5]. In Step 1, the PS (national RM; in this example, benzoic acid [NIST SRM 350a] is used) is used to characterize the specified peak of the transfer material using quantitative NMR. In Step 2, the specified peak of the characterized transfer material is adopted as the standard for characterization of the analyte. By adopting this two-step analytical method, the number of national RMs, which anchor the metrological traceability system, can be minimized. In addition, by ensuring homogeneity and long-term stability of the transfer materials, it is possible to supply the transfer materials as RMs for quantitative NMR, by which substances suitable for measurements of analytes can be widely selected. Thus, the introduction of the transfer materials in quantitative NMR was a crucial development in the process of integrating the elemental technologies.

Evaluating the integrated technologies

We described how several elemental technologies were integrated to construct an analytical technology using quantitative NMR. Next, we demonstrated the

reliability of the technologies by comparing them with long-established techniques. To do this, we first selected several target substances from commercially available, pesticide standards. Their purity values were determined using the freezing point depression method, a well-established primary direct method that AIST has been using for the valuation of national RMs (see Table 1). Then we measured the same samples with the newly developed quantitative NMR to find the purity value, and checked whether the two values matched in the range of their respective uncertainties.

As the PS for measurements using quantitative NMR, we used 1,4-dichlorobenzene (NMIJ CRM 4039-a, 99.99 % \pm 0.03 %), a national RM supplied by the National Metrology Institute of Japan (NMIJ). However, since 1,4-dichlorobenzene is rather difficult to use in terms of high sublimability, a two-step characterization was adopted by which 1,4-BTMSB-*d*₄ (1,4-bis(trimethylsilyl) benzene-*d*₄), DSS-*d*₆ (3-(trimethylsilyl)-1-propane-1,1,2,2,3,3-*d*₆-sodium sulfonate) or DMSO₂ (dimethyl sulfone) was used as the transfer material. To dissolve the transfer material and the analyte, solvents were selected from a number of deuterated solvents, to minimize skewing of results from the protons of any impurities in the solvent. The solubility and other characteristics of the transfer material and analyte were also taken into consideration, and a solution with a concentration of about 1000 mg/L was prepared.

The analytical results with 400 MHz NMR spectrometer (JNM-ECS 400) are summarized in **Table 2**. Although in many cases the uncertainty was larger for the purity values by quantitative NMR compared to freezing point depression method, the values for the two methods matched within the uncertainty ranges, demonstrating that our analytical technology using quantitative NMR was sufficiently reliable [6]. The uncertainty for quantitative NMR was between 0.5 % and 1.0 % ($k=2$, 95 % confidence interval). Although this accuracy as a purity measurement technology is somewhat inferior to the freezing point depression method, quantitative NMR can be used to calibrate substances to which the freezing point depression method cannot be applied, including a wide range of organic compounds, and it satisfies the market demand for the uncertainty levels in working RMs.

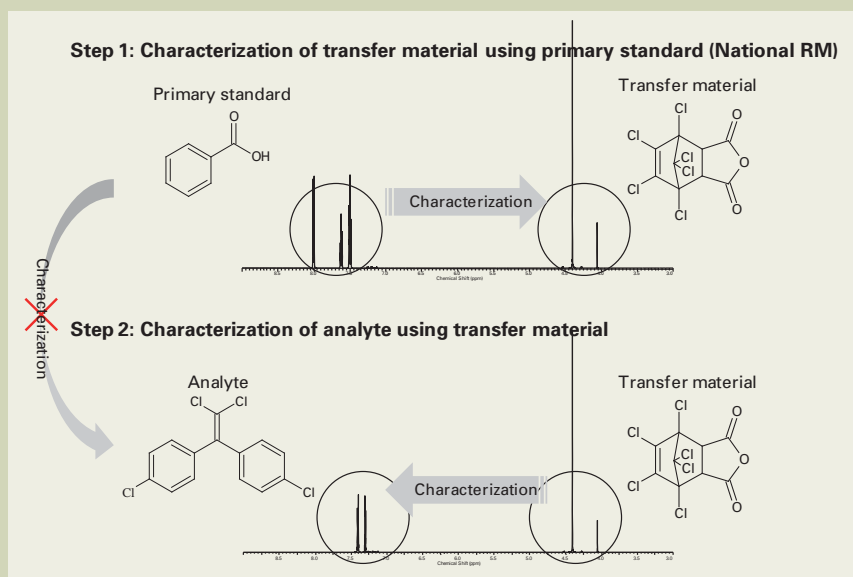


Fig. 7 Use of transfer material in quantitative NMR.

Practical application of the quantitative NMR

We envision a transfer from the current one-to-one metrological traceability system based on separate national RMs for each substance, to one-to-many metrological traceability system in which several substances can be traced to just a few national RMs. So far, we made advancement for the development of universal analytical technology, a core technology applicable to numerous organic compounds. After establishing an ideal scenario for this project, we began by developing

elemental technologies, using irradiation pulse delay time and optimization of audio filters. We then demonstrated that these analytical technologies could satisfy market requirements for uncertainty. We learned that the transfer materials could be used to minimize the number of national RMs required as standards for amount-of-substance. Finally, we plotted a roadmap toward a metrological traceability system, as illustrated in **Figure 8**.

The system we outlined represents a quantum leap in the innovative metrological traceability systems, since it removes the need to maintain one-to-one characterization chain from national RMs to working RMs for individual substances.

As for quantitative NMR that is a core of the

Table 2 Purity analysis results for organic compounds using quantitative NMR.

Target substance	Freezing point depression method		Quantitative NMR				
	Reference value (%)	Uncertainty (% $, k=2$)	Analytical value (%)	Uncertainty (% $, k=2$)	Primary standard	Transfer material	Solvent
Echlomezol	99.4	0.7	99.3	0.5	1,4-Dichlorobenzene	1,4-BTMSB- d_4	Acetone- d_6
Dimepiperate	99.5	0.6	99.7	0.9	1,4-Dichlorobenzene	1,4-BTMSB- d_4	Dichloromethane- d_2
Isoprothiolane	99.9	0.1	99.9	0.5	1,4-Dichlorobenzene	1,4-BTMSB- d_4	Acetone- d_6
Alachlor	99.8	0.2	99.7	0.5	1,4-Dichlorobenzene	1,4-BTMSB- d_4	Acetonitrile- d_3
Carboxin	99.6	0.4	99.5	0.5	1,4-Dichlorobenzene	1,4-BTMSB- d_4	Dichloromethane- d_2
Linuron	99.7	0.4	99.6	1.0	1,4-Dichlorobenzene	1,4-BTMSB- d_4	Acetone- d_6
Pyrimethanil	99.9	0.1	100.0	0.5	1,4-Dichlorobenzene	1,4-BTMSB- d_4	Methanol- d_4
Tiadinil	99.6	0.5	99.4	0.9	1,4-Dichlorobenzene	1,4-BTMSB- d_4	Methanol- d_4
Flusulfamide	99.6	0.3	99.3	0.8	1,4-Dichlorobenzene	1,4-BTMSB- d_4	Methanol- d_4
Carbofuran	99.8	0.4	99.8	0.6	1,4-Dichlorobenzene	1,4-BTMSB- d_4	Acetonitrile- d_3
Fthalide	99.8	0.3	99.6	0.7	1,4-Dichlorobenzene	DMSO $_2$	Chloroform- d
Methomyl	99.5	0.5	99.9	0.5	1,4-Dichlorobenzene	1,4-BTMSB- d_4	Dichloromethane- d_2
Tricyclazole	99.5	0.2	99.6	0.9	1,4-Dichlorobenzene	DSS- d_6	DMSO- d_6
Fludioxonil	99.8	0.2	99.5	0.8	1,4-Dichlorobenzene	DSS- d_6	DMSO- d_6
Prometryn	99.7	0.3	99.5	0.9	1,4-Dichlorobenzene	DSS- d_6	DMSO- d_6
Clothianidin	Inapplicable (thermal decomposition)		99.6	0.8	1,4-Dichlorobenzene	DSS- d_6	Methanol- d_4
Cymoxanil	Inapplicable (thermal decomposition)		99.9	0.8	1,4-Dichlorobenzene	1,4-BTMSB- d_4	Acetonitrile- d_3
Theflubenzuron	Inapplicable (uncrystallized)		99.9	0.9	1,4-Dichlorobenzene	1,4-BTMSB- d_4	DMSO- d_6
<i>trans</i> -Permethrin	Inapplicable (uncrystallized)		99.8	0.6	1,4-Dichlorobenzene	DMSO $_2$	Acetonitrile- d_3
Myclobutanil	Inapplicable (uncrystallized)		99.8	0.6	1,4-Dichlorobenzene	DMSO $_2$	Acetonitrile- d_3
Tebufenpyrad	Inapplicable (uncrystallized)		98.1	0.9	1,4-Dichlorobenzene	DMSO $_2$	Dichloromethane- d_2

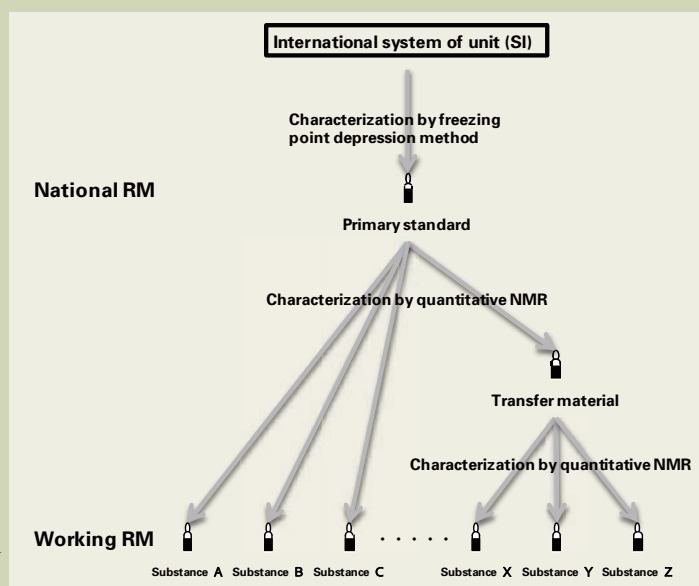


Fig. 8 Innovative metrological traceability system with quantitative NMR.

system, it is important to build infrastructures to realize a rapid transfer to a system in which a variety of chemical substances necessary for the society can be characterized by many institutes. From this viewpoint, we are implementing collaborative research projects with National Institute of Health Sciences and also with JEOL RESONANCE Inc., Wako Pure Chemical Industries, Ltd. and Kao Corporation. In these research projects, we are advancing the standardization of analytical methods by actively making our achievements public through verification tests and by conducting comparison tests among institutes. In addition, we are working on the development of easy-to-use transfer materials as RMs used for quantitative NMR (being supplied by Wako Pure Chemical Industries, Ltd.) and the preparation of an automation tool whose function ranges from measurement parameter setting to data analysis in quantitative NMR (being supplied by JEOL RESONANCE Inc.).

Many de facto commercial reagents are in use today, even though evaluation of their purity or concentration remains inadequate. For example, for active substances in natural sources, such as herbal medicines, quantitative analysis often depends on the samples of isolated constituents or the commercially available reagents. Quantitative NMR can offer highly reliable and effective quantitative analysis in such cases (see **Figure 9**) [7, 8], where the discovery of appropriate standard would normally be difficult, and therefore, the adoption of quantitative NMR by the Japanese Pharmacopoeia (JP) is being discussed as an analytical method to determine absolute purities of reference standards for quantitative analyses [9, 10, 11].

Future directions

Quantitative NMR has great potential marketability, as the necessary analytical equipment are commercialized (Figure 6: Future issues). As reasonably priced, easy-to-use equipment, which are optimized for quantitative NMR, become available, and applications for nuclei other than ^1H are developed, they will find use not only in analytical technologies for working RMs, but also in quantitative analysis of several organic compounds occurring in numerous fields conducted at a wide variety of proving,

testing, and research laboratories.

Perhaps most exciting of all, an innovative metrological traceability system based on this analytical technology for organic compounds may provide an effective scheme for responding flexibly to today's proliferating demand for RMs. Although core technologies other than quantitative NMR have not yet been demonstrated, universal analytical technologies that can be used similarly in the construction of a rational metrological traceability system may be developed. The Authors hope that this paper will serve as a starting point for the development of such universal analytical technology.

Acknowledgments

The Authors would like to acknowledge the valuable sources we consulted to bring the research results to fruition. The analytical results for agricultural compounds were derived from "Research on the supply of RMs related to foodstuffs and agricultural compounds," a paper commissioned by Wako Pure Chemicals Industries, Ltd. Our heartfelt thanks go out to Ms. Yuko Yamada and Mr. Shinji Nakao (Wako Pure Chemicals Industries, Ltd.), who provided samples and cooperated on evaluation. We wish to thank Dr. Tetsuji Nishimura, Dr. Naoki Sugimoto, Dr. Hiroshi Akiyama, Dr. Takeshi Yamazaki, Dr. Atsuko Tada, Dr. Takashi Ohtsuki and Dr. Yukihiro Goda (National Institute of Health Sciences, Japan); Dr. Takako Suematsu and Mr. Hiroto Suematsu (JEOL RESONANCE Inc.); Dr. Ryo Koike and Mr. Takaaki Horinouchi (Kao Corporation); Mr. Keiji Ohno, Ms. Yuko Yamada and Mr. Toru Miura (Wako Pure Chemicals Industries, Ltd.), for two collaborative papers, "Establishing measurement methods for the standardization of qNMR" and "Building the infrastructures for dissemination of qNMR and promoting expansion of demand for qNMR" which provided the content for the proposals in Sections of "Practical application of the quantitative NMR" and "Future directions" of this paper. Finally, Dr. Koichi Chiba and Dr. Shinichi Kinugasa (AIST) provided valuable assistance in writing this paper, for which we thank him sincerely.

This paper is based on a paper titled "Expansion of organic reference materials for the analysis of hazardous substance in foods and environment, *Synthesiology* Vol.2,

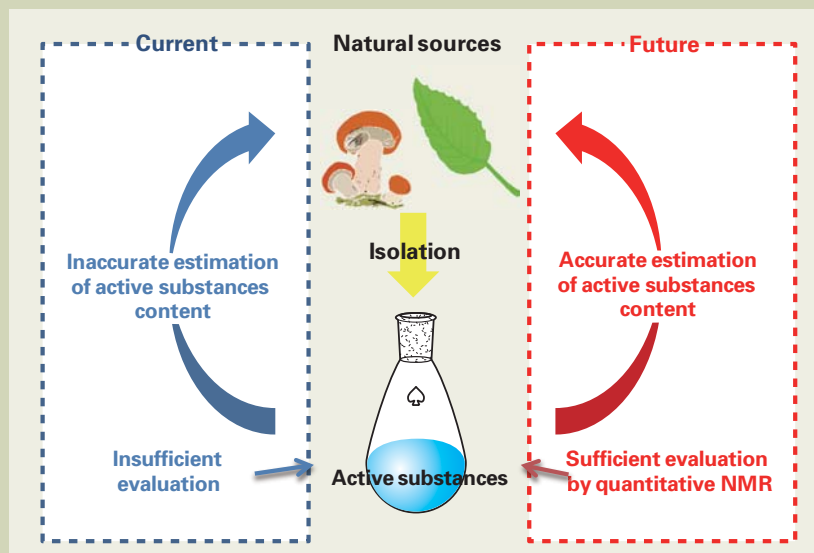


Fig. 9 Quantitative evaluation of active substances in natural sources using quantitative NMR.

No.1, 12-22 (2009)” and partially modifies its content.

Terminology

- Term 1. Positive list system: Established in 2006 based on a revision of Japan's Food Sanitation Law, this system prohibits the sales of foods that contain agricultural chemical residues above a certain quantity. In cases where the safe (not harmful to human) quantity has been specified (called the residue level), the agricultural chemical must be below that quantity. In case where the safe quantity has not been specified, a uniform limit of 0.01 ppm is applied.
- Term 2. Official method of analysis: A set of analytical procedures officially published and recognized in accordance with laws governing chemical compounds, to enable comparison of analytical results among different testing laboratories and samples. An official method of analysis must be robust and universally applicable. Examples used in Japan are Japanese Industrial Standard (JIS), Japanese Agricultural Standard (JAS), and Japanese Pharmacopoeia (JP).
- Term 3. Certified reference material (CRM): In ISO Guide 35, which provides the international guidelines for RMs, this is defined as “reference material, characterized by a metrologically valid procedure for one or more specified properties, accompanied by a certificate that provides the value of the specified property, its associated uncertainty, and a statement of metrological traceability.”
- Term 4. Metrological traceability: The characteristic of a measurement result, where the result can be linked to a known reference standard (usually a national standard) through an unbroken chain. In the 3rd version of the International Vocabulary of Metrology (VIM), this term was amended from “traceability” to “metrological traceability” to distinguish from the term used to manage the shipping histories of foods and other goods.
- Term 5. National metrology institute: A research institute that sets a country's official measurement standards. In Japan, it is the National Metrology Institute of Japan within the National Institute of Advanced Industrial Science and Technology.
- Term 6. Primary method of measurement: The method used to define national RMs. It is defined as follows: “primary method of measurement is a method having the highest metrological qualities, whose operation can be completely described and understood, for which a complete uncertainty statement can be expressed in terms of SI units.”
- Term 7. Consultative Committee for Amount of Substance (Comité Consultatif pour la Quantité de Matière: CCQM): One of the consultative committees formed under the aegis of the International Committee of Weights and Measures (Bureau International des Poids et Mesures: BIPM) that consists of the Meter Convention member institutions. Established in 1993, this consultative committee discusses issues on metrology in chemistry.
- Term 8. International comparison (CCQM inter-comparison): Comparison among calibration laboratories to confirm the degree of equivalence in the calibration and measurement capabilities and

values assigned to RMs between various national metrology institutes. Normally, this process begins with an international comparison for research purposes, called a pilot study. After the technical groundwork has been established to a certain degree, an official international comparison, called a key comparison, is performed.

References

- [1] ISO Guide 35: Reference materials - *General and statistical principles for certification*, p.2, International Organization for Standardization, Geneva, Switzerland (2006).
- [2] G. Maniara, K. Rajamoorthi, S. Rajan and G. W. Stockton: Method performance and validation for quantitative analysis by ^1H and ^{31}P NMR spectroscopy. Applications to analytical standards and agricultural chemicals, *Anal. Chem.*, **70**, 4921-4928 (1998).
- [3] T. Saito, T. Ihara, H. Sato, J. Harald, and S. Kinugasa: International comparison on the determination of an ethanol aqueous solution by ^1H nuclear magnetic resonance, *Bunseki Kagaku*, **52**, 1029-1036 (2003).
- [4] T. Saito, S. Nakaie, M. Kinoshita, T. Ihara, S. Kinugasa, A. Nomura and T. Maeda: Practical guide for accurate quantitative NMR analysis, *Metrologia*, **41**, 213-218 (2004).
- [5] T. Saito, T. Ihara, M. Koike, S. Kinugasa, Y. Fujimine, K. Nose and T. Hirai: A new traceability scheme for the development of international system-traceable persistent organic pollutant reference materials by quantitative nuclear magnetic resonance, *Accred. Qual. Assur.*, **14**(2), 79-86 (2009).
- [6] T. Saito, T. Ihara, T. Miura, Y. Yamada and K. Chiba: Efficient production of reference materials of hazardous organics using smart calibration by nuclear magnetic resonance, *Accred. Qual. Assur.*, **16**(8-9), 421-428 (2011).
- [7] N. Sugimoto, A. Tada, T. Suematsu, K. Arifuku, T. Saito, T. Ihara, Y. Yoshida, R. Kubota, M. Tahara, K. Shimizu, S. Ito, T. Yamazaki, Y. Kawamura and T. Nishimura: Absolute quantification of carminic acid in cochineal extract by quantitative NMR, *Shokuhin Eiseigaku Zasshi*, **51**(1), 19-27 (2010).
- [8] M. Tahara, T. Suematsu, M. Hayakawa, Y. Goda, Y. Konishi and N. Sugimoto: Application of quantitative NMR to determine absolute purities of trichothecenes, *Micotoxins* (in press).
- [9] M. Tahara, N. Sugimoto, T. Ohtsuki, A. Tada, H. Akiyama, Y. Goda and T. Nishimura: Determination of the purities of commercial reagent products using qNMR for ensuring the reliability of quantitative analysis, *Journal of Environmental Chemistry* (in press).
- [10] J. Hosoe, N. Sugimoto and Y. Goda: Trial study to determine absolute purities of chemical reagents used as reference standards in the Japanese Pharmacopoeia by using quantitative NMR (qNMR), *Pharmaceutical and Medical Device Regulatory Science*, **41**(12), 960-970 (2010).
- [11] J. Hosoe, N. Sugimoto, T. Suematsu, Y. Yamada, M. Hayakawa, T. Katsuhara, H. Nishimura and Y. Goda: Validation studies of qNMR for chemical reagents used as reference standards for quantitative analyses of crude drugs in the Japanese Pharmacopoeia, *Pharmaceutical and Medical Device Regulatory Science*, **43**(2), 182-193 (2012).

Introduction of New Products

Field Emission Scanning Electron Microscope

JSM-7100F

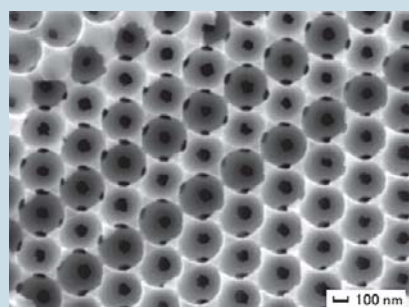
The JSM-7100F is a versatile high performance analytical FE-SEM. The electron optics produces the maximum 200 nA probe current with the patented in-lens Schottky FEG and a small probe diameter even at large probe currents with the patented aperture angle optimizing lens. The objective lens is the field free type. This lens is suitable for high precision EBSD analysis and characterization of a magnetic specimen.

Resolution : 1.2nm (30 kV), 3.0nm (1 kV)
 Accelerating voltage : 0.2 to 30 kV
 Magnification : × 10 to 1,000,000

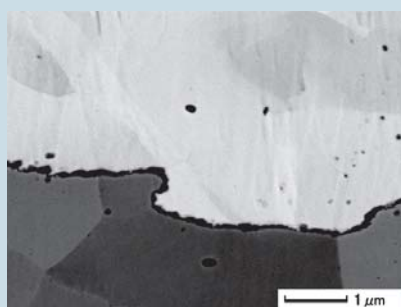


Observation

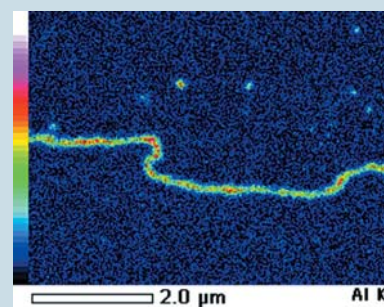
A variety of images, such as secondary electron images, backscattered electron images, and STEM images, are obtained. The stable Schottky field emission electron source ensures research with high quality images.



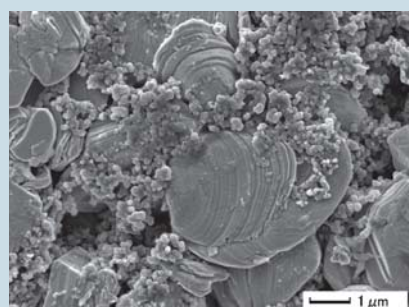
Three dimensionally ordered macroporous carbon*
 (Secondary electron image) ×50,000, 3kV



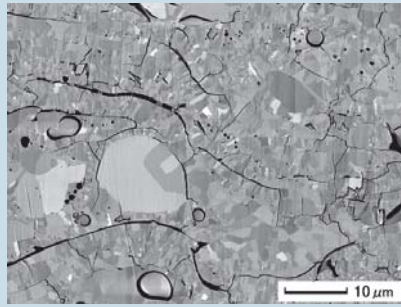
Cross section of zinc plating
 (Backscattered electron image) ×20,000, 5kV



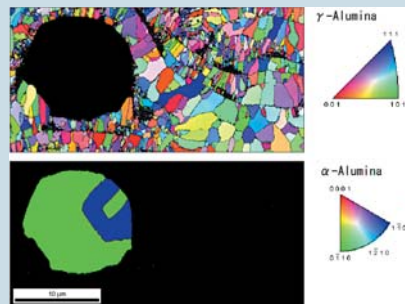
Cross section of zinc plating
 (EDS elemental map)



Anode of lithium battery
 (Secondary electron image) ×13,000, 3kV



Thermal sprayed alumina film
 (Backscattered electron image) ×2,000, 2.5kV



EBSD IPF MAP (ND)

*Specimen courtesy of Professor Andreas Stein Department of Chemistry, University of Minnesota

Benchtop SEM

JCM-6000

JCM-6000 NeoScope™ let's you observe a specimen at much higher magnification than a light microscope with the same simple operation of a light microscope. The observation image appears automatically when a specimen is inserted, and you can go up to the maximum magnification of $\times 60,000$ quickly with the automated operations.

JCM-6000 NeoScope™ is equipped with a TMP for quick start. The installation is easy. The wall outlet (100V AC) is the only utility needed. Cooling water is not necessary.

Magnification : $\times 10$ to 40,000
Accelerating voltage : 15 kV/10 kV/5 kV



High Performance GC-TOF MS

JMS-T100GCV

AccuTOF GCv 4G

The AccuTOF GCv 4G is a fully automated Gas Chromatograph Time-of-Flight Mass Spectrometer (GC-TOFMS).

A data recording speed of 50 spectra/second enables high throughput analysis.

A new high speed preamp and data acquisition system is capable of sampling TOFMS signal at 4 giga samples/second, twice faster than the previous system. It also enables more efficient high-resolution, high-accuracy analysis.

An improved detection system has extended the practical mass range for FD ionization.





Certain products in this brochure are controlled under the "Foreign Exchange and Foreign Trade Law" of Japan in compliance with international security export control. JEOL Ltd. must provide the Japanese Government with "End-user's Statement of Assurance" and "End-use Certificate" in order to obtain the export license needed for export from Japan. If the product to be exported is in this category, the end user will be asked to fill in these certificate forms.

JEOL JEOL Ltd.

1-2 Musashino 3-chome Akishima Tokyo 196-8558 Japan Sales Division Telephone:+81-42-528-3381 Facsimile:+81-42-528-3386

<http://www.jeol.com/>

ARGENTINA
COASIN S.A.C.IyF.
Virrey del Pino 4071,
1430 Buenos Aires
Argentina
Telephone: 54-11-4552-3185
Facsimile: 54-11-4555-3321

AUSTRALIA&NEWZEALAND
JEOL(AUSTRALASIA) Pty.Ltd.
Suite 1, L2 18 Aquatic Drive
- Frenchs Forest NSW 2086
Australia
Telephone: 61-2-9451-3855
Facsimile: 61-2-9451-3822

AUSTRIA
JEOL (GERMANY) GmbH
Oskar-Von-Miller-Strasse 1a, 85386
Eching, Germany
Telephone: 49-8165-77346
Facsimile: 49-8165-77512

BANGLADESH
A.Q. CHOWDHURY SCIENCE & SYNERGY PVT. LTD.
House No. 12, Road No. 5A
Sector No. 11, Uttara Dhaka - 1230
Bangladesh
Telephone: 880-2-9890790, 8953450, 8953501
Facsimile: 880-2-8854428

BELGIUM
JEOL (EUROPE) B.V.
Planet II, Gebouw B
Leuvensesteenweg 542,
B-1930 Zaventem
Belgium
Telephone: 32-2-720-0560
Facsimile: 32-2-720-6134

BRAZIL
JEOL Brasil Instrumentos Cientificos Ltda.
Av. Jabaquara, 2958-5° andar-cj. 52
04046-500 Sao Paulo, SP
Brazil
Telephone: 55-11-5070 4000
Facsimile: 55-11-5070 4010

CANADA
JEOL CANADA, INC.
3275 Premier Rue #8
St-Hubert, Quebec J3Y 8Y6, Canada
Telephone: 1-450-676-8776
Facsimile: 1-450-676-6694

CHILE
ARQUIMED INNOVATION
Arturo Prat 828,
Santiago, Chile
Telephone: 56-2-634-6266
Facsimile: 56-2-634-4633

CHINA
JEOL(BEIJING) CO., LTD.
Room B1010/1110, Wantong New World Plaza No. 2
Fuchengmenwai Street, Xicheng District,
Beijing 100037, P.R.China
Telephone: 86-10-6804-8321
Facsimile: 86-10-6804-6324

JEOL (BEIJING) CO., LTD., SHANGHAI BRANCH
Room 1505/1506, No1 300Xi Kang Road,
Jing an Dist., Shanghai, 200040, China
Telephone: 86-21-6248-4888/4487/4537/4404
Facsimile: 86-21-6248-4075

JEOL (BEIJING) CO., LTD., GUANG ZHOU BRANCH
N1801/1808, World Trade Center Building,
371-375, Huan Shi Road East, Guang Zhou,
Guangdong Prov., 510095, P.R.China
Telephone: 86-20-8778-7848
Facsimile: 86-20-8778-4268

JEOL (BEIJING) CO., LTD., WUHAN BRANCH
Room 3216, World Trading Bldg.
688 Jiefang Street, Hankou, Wuhan, Hubei 430032
P.R.China
Telephone: 86-27-8544-8953
Facsimile: 86-27-8544-8695

JEOL LTD. (BEIJING) CO., LTD., CHENGDU BRANCH
1807A Zongfu Building,
NO. 45 Zhongfu Road, Chengdu, Sichuan, 610016
P.R. China
Telephone: 86-28-86622554
Facsimile: 86-28-86622564

EGYPT
JEOL SERVICE BUREAU
3rd Fl. Nile Center Bldg., Nawal Street,
Dokki, (Cairo), Egypt
Telephone: 20-2-3335-7220
Facsimile: 20-2-3338-1186

FRANCE
JEOL (EUROPE) SAS
Espace Claude Monet, 1 Allée de Giverny
78290, Croissy-sur-Seine, France
Telephone: 33-13015-3737
Facsimile: 33-13015-3747

GERMANY
JEOL (GERMANY) GmbH
Oskar-Von-Miller-Strasse 1a, 85386
Eching, Germany
Telephone: 49-8165-77346
Facsimile: 49-8165-77512

GREATBRITAIN&IRELAND
JEOL (U.K.) LTD.
JEOL House, Silver Court, Watchmead,
Welwyn Garden City, Herts AL7 1LT, U.K.
Telephone: 44-1707-377117
Facsimile: 44-1707-373254

GREECE
N. ASTERIASIS S.A.
56-58, S. Trikoupis Str. P.O. Box 26140
GR-10022, Athens, Greece
Telephone: 30-1-823-5383
Facsimile: 30-1-823-9567

HONGKONG
FARMING LTD.
Unit 1009, 10/F., MLC Millennium Plaza
683 King's Road, North Point, Hong Kong
Telephone: 852-2815-7290
Facsimile: 852-2581-4635

INDIA
JEOL INDIA Pvt. Ltd.
Elegance Tower, Level 2, 212B
Old Mathura Road, Jasola Business District Centre,
Near Apollo Hospital, Jasola,
New Delhi 110 025, India
Telephone: 91-11-4372-2578
Facsimile: 91-11-4050-1235

BLUE STAR LTD. (HQ: Mumbai)
Analytical Instruments Department,
Sahas 414/2 Veer Savarkar Marg
Prabhadey Mumbai 400 025, India
Telephone: 91-22-6666-4000
Facsimile: 91-22-6666-4001

BLUE STAR LTD. (Delhi)
Analytical Instruments Department,
E-24/12 Okhla Industrial Area,
Phase-II, New Delhi 110 020, India
Telephone: 91-11-4149-4000
Facsimile: 91-11-4149-4005

BLUE STAR LTD. (Calcutta)
Analytical Instruments Department,
7, Hare Street Calcutta 700 001, India
Telephone: 91-33-2213-4133
Facsimile: 91-33-2213-4102

BLUE STAR LTD. (Chennai)
Analytical Instruments Department,
No. 46, Garuda Building,
Cathedral Road, Chennai 600 086, India
Telephone: 91-44-4244-4000
Facsimile: 91-44-4244-4190

INDONESIA
PT. TEKNO LABINDO Penta Perkasa
Komplek Gading Bukit Indah Blok I/11
Jl. Bukit Gading Raya Kelapa Gading Permai,
Jakarta 14240, Indonesia
Telephone: 62-21-45847057/58/59
Facsimile: 62-21-45842729

ITALY
JEOL (ITALIA) S.p.A.
Centro Direzionale Green Office
Via dei Tulpani, 1
20090 Pieve Emanuele (MI) Italy
Telephone: 39-02-9041431
Facsimile: 39-02-90414343

KOREA
JEOL KOREA LTD.
Dongwoong Bldg. 7F, 1443, Yangjae Daero,
Gangdong-Gu, Seoul, 134-010, Korea
Telephone: 82-2-511-5501
Facsimile: 82-2-511-2655

KUWAIT
Ashraf & CO. Ltd. W.L.L.
P.O.Box 3555 Safat 13036, Kuwait
Telephone: 965-1805151
Facsimile: 965-24335373

MALAYSIA
JEOL(MALAYSIA) SDN.BHD.(359011-M)
205, Block A, Mezzanine Floor,
Kelana Business Center,
97, Jalan SS 7/2, Kelana Jaya,
47301 Petaling Jaya, Selangor, Malaysia
Telephone: 60-3-7492-7722
Facsimile: 60-3-7492-7723

MEXICO
JEOL DE MEXICO S.A. DE C.V.
Arkansas 11 Piso 2
Colonia Napoléon
Delegación Benito Juárez, C.P. 03810
Mexico D.F., Mexico
Telephone: 52-55-55-211-4511
Facsimile: 52-55-55-211-0720

PAKISTAN(Karachi)
ANALYTICAL MEASURING SYSTEM (PVT) LTD.(AMS LTD.)
14-C Main Sehar Commercial Avenue Lane 4,
Khayaban-e-Sehar,
D.H.A-VII, Karachi-75500, Pakistan
Telephone: 92-21-35345581/35340747/35346057-8
Facsimile: 92-21-35345582

PANAMA
PROMED S.A.
Parque Industrial Costa del Este
Urbanización Costa del Este
Apartado 0818-01755, Panama, Panama
Telephone: 507-3093100
Facsimile: 507-3093115

PHILIPPINES
PHILAB INDUSTRIES INC.
7487 Baotikan Street, SAV Makati,
1203 Metro, Manila Philippines
Telephone: 63-2-896-7218
Facsimile: 63-2-897-7732

PORTUGAL
Izasa Portugal Lda.
R. do Prdletariado, 1
2790-138 CARNAXIDE, Portugal
Telephone: 351-21-424-73-00
Facsimile: 351-21-418-60-20

RUSSIA
JEOL (RUS) LLC.
Krasnoprolatarskaya Street, 16,
Bld. 2, 127473, Moscow,
Russian Federation
Telephone: 7-495-748-7791/7792
Facsimile: 7-495-748-7793

SAUDI ARABIA
ABDULREHMAN ALGOSAIBI G.T.O. (Riyadh)
King Abdulaziz Avenue,
P.O. Box 215, Riyadh 11411, Saudi Arabia
Telephone: 966-1-479-3000
Facsimile: 966-1-477-1374

SCANDINAVIA
SWEDEN
JEOL (Skandinaviska) AB
Hammarbacken 6A, Box 716, 191 27 Sollentuna
Sweden
Telephone: 46-8-28-2800
Facsimile: 46-8-29-1647

SERVICE & INFORMATION OFFICE
NORWAY
JEOL (Skandinaviska) AB
Lorenvangen 23, 0580 Oslo, NORWAY
Telephone: 47-2-2-64-7930
Facsimile: 47-2-2-65-0619

FINLAND
JEOL (Skandinaviska) AB
Ylkaupinkuja 2, FIN-02360 Espoo, Finland
Telephone: 358-9-8129-0350
Facsimile: 358-9-8129-0351

SINGAPORE
JEOL ASIA PTE, LTD.
2 Corporation Road #01-12 Corporation Place
Singapore 618494
Telephone: 65-6565-9889
Facsimile: 65-6565-7552

SOUTH AFRICA
ADI Scientific (Pty) Ltd.
370 Angus Crescent,
Northlands Business Park, 29 Newmarket Road
Northridge, Randburg, Republic of South Africa
Telephone: 27-11-462-1393
Facsimile: 27-11-462-1466

SPAIN
IZASA S.A.
Argoneses, 13, 28100 Alcobendas,
(Poligono Industrial), Madrid, Spain
Telephone: 34-91-663-0500
Facsimile: 34-91-663-0545

SWITZERLAND
JEOL (GERMANY) GmbH
Oskar-Von-Miller Strasse 1,
85386 Eching, Germany
Telephone: 49-8165-77346
Facsimile: 49-8165-77512

TAIWAN
JIE DONG CO., LTD.
7F, 112, Chung Hsiao East Road,
Section 1, Taipei, Taiwan 10023
Republic of China
Telephone: 886-2-2395-2978
Facsimile: 886-2-2322-4655

For Mass Spectrometer Products:
Mass Solutions Technology Co., Ltd.
5F, No.79, Sec. 1, Xintai 5th Rd,
Xizhi Dist., New Taipei City 221, Taiwan
Republic of China
Telephone: 886-2-2698-9511
Facsimile: 886-2-2698-9512

For Semiconductor Products:
JEOL TAIWAN SEMICONDUCTORS LTD.
11F-1, No. 346, Pei-Da Road, Hsin-Chu City 300,
Taiwan, Republic of China
Telephone: 886-3-523-4480
Facsimile: 886-3-523-8503

THAILAND
BECTHAI BANGKOK EQUIPMENT & CHEMICAL CO., Ltd.
300 Phaholyothin Rd. Phayathai, Bangkok 10400,
Thailand
Telephone: 66-2-615-2929
Facsimile: 66-2-615-2350/2351

THE NETHERLANDS
JEOL (EUROPE) B.V.
Lirweg 4, NL-2153 PH Nieuw-Vennep,
The Netherlands
Telephone: 31-252-623500
Facsimile: 31-252-623501

TURKEY
TEKSER A.S.
Kayisdagi, Inonu Mah,Kartal Cad. No:55/3
34755 Atasehir / Istanbul, Turkey
Telephone: 90-216-5736470
Facsimile: 90-216-5736475

UAE
MRS Group Dubai
P.O.Box: 171612,
Rashid Abdulla Al Noami Building
Suite No: 306, Damascus Street,
Al Qusais-3, Dubai, U.A.E.
Telephone: 971-4-2581141
Facsimile: 971-4-2581151

JEOL Gulf
P.O.Box: 171612,
Rashid Abdulla Al Noami Building
Suite No: 306, Damascus Street,
Al Qusais-3, Dubai, U.A.E.
Telephone: 971-553964219(mobile)

USA
JEOL USA, INC.
11 Dearborn Road, Peabody, MA 01960, U.S.A.
Telephone: 1-978-535-5900
Facsimile: 1-978-536-2205/2206

JEOL USA, INC. WEST OFFICE
5653 Stoneridge Drive Suite #110
Pleasanton, CA 94588, U.S.A.
Telephone: 1-925-737-1740
Facsimile: 1-925-737-1749

VENEZUELA
GOMSA Service and Supply C.A.
Urbanization Montalban III
- Residencias Don Andres - Piso 7 - Apartamento 74
Avenida 3, entre calles 7 y 6
Montalban, Caracas, Venezuela
Telephone: 58-212-443-4342
Facsimile: 58-212-443-4342

VIETNAM
TECHNICAL MATERIALS AND RESOURCES IMPORT-EXPORT JOINT STOCK
COMPANY(REXCO)
Hanoi Branch,
No. 13-Lot 12 Trung Yen, Trung Hoa Street, Cau Giay Dist, Hanoi, Vietnam
Telephone: 84-4-562-0516, 17/562-0535
Facsimile: 84-4-853-2511